UNIVERSITÄT ZU LÜBECK
INSTITUT FÜR ROBOTIK
UND KOGNITIVE SYSTEME

Augmented Reality Applications to Facilitate Vascular Diagnostics and Interventions

Towards X-Ray Free Image-Guidance

Felix von Haxthausen

Dissertation

University of Lübeck
Institute for Robotics and Cognitive Systems

UNIVERSITÄT ZU LÜBECK

From the Institute for Robotics and Cognitive Systems
of the University of Lübeck
Director: Prof. Dr.–Ing. Achim Schweikard

Augmented Reality Applications to Facilitate Vascular Diagnostics and Interventions

Towards X-Ray Free Image-Guidance

Dissertation
for Fulfillment of Requirements
for the Doctoral Degree
of the University of Lübeck

from the Department of Computer Sciences and Technical Engineering

Submitted by
Felix von Haxthausen
from Ludwigshafen am Rhein

Lübeck, 2023

First referee: Prof. Dr. rer. nat. Floris Ernst

Second referee: Prof. Dr.-Ing. Nicole Jochems

Date of oral examination: 24th November 2023

Approved for printing. Lübeck, 1st December 2023

Find joy in everything you choose to do. Every job, relationship, home... it’s your responsibility to love it, or change it...

Chuck Palahniuk

Abstract

Cardiovascular diseases are the leading cause of death in Europe, accounting for 46 % of deaths in women and 39 % in men. Consequently, safe and accurate methods of diagnosis and intervention are crucial. Current procedures rely on X-rays, which are based on carcinogenic ionizing radiation, or ultrasound (US), requiring an experienced clinician, has an ergonomically poor workflow, and is susceptible to artifacts. However, since US is a safe, cost-effective and widely available imaging modality, it is worthwhile to use this modality for diagnostics and interventions while surmounting the existing drawbacks through the application and development of innovative technologies. Therefore, Augmented Reality (AR) applications and specific tracking methods will be developed and evaluated in this thesis, which will support and simplify US-based vascular diagnostics and endovascular interventions.

For vascular diagnostics, a system was designed to assist the physician during the examination through intuitive augmented reality-based in-situ visualization, followed by automatic vessel segmentation. To this end, a new inside-out tracking method was devised, allowing the AR head-mounted-display (HMD) to spatially track the probe without the need for an external tracking system. Extensive testing revealed that tracking could be performed with a mean accuracy of 1.98 mm/1.81° for the static configuration. The mean error in a dynamic scenario was 2.81 mm/1.70°. The segmentation task was solved by implementing a state-of-the-art deep learning approach, and the result provides the physician with a robust indication of the artery's location and size, thereby facilitating the diagnostic process. The network has been trained and tested on US images of the femoral artery of healthy volunteers, demonstrating its viability on realistic images with a dice score of 0.82.

In order to facilitate endovascular interventions, this thesis presents a novel technical configuration that can visualize real-time 3D US through an AR HMD in order to guide vascular access prior to intervention. For the procedure itself, the device provides a 3D visualization of the vessel structure, including the current position and orientation of the endovascular instrument with respect to it, thereby making fluoroscopy potentially unnecessary. As for the first application, a remote rendering approach provides the computational capacity necessary for a suitably high frame rate and minimal latency. Furthermore, the experiments show that 3D US may offer additional benefits in US-guided tasks (i.e., reduced task completion time) over 2D US images viewed in AR. The developed assistance system for the actual endovascular intervention enables tracking of instruments by means of electromagnetic

tracking and an intuitive visualization of the 3D vascular tree, including the pose of the catheter tip with the AR HMD. An in-depth evaluation of the tracking accuracy, including a landmark-based registration, showed promising results with a mean error of 1.38 mm.

In summary, this dissertation presents novel AR applications that have the potential to facilitate both vascular diagnostics and interventions using ultrasound and easy-to-setup tracking techniques - without relying on the use of X-rays. The further development of AR HMDs coupled with safe and novel imaging modalities such as magnetic particle imaging, including non-rigid registration approaches, represent important future research areas.

Kurzfassung

Herz-Kreislauf-Erkrankungen sind die häufigste Todesursache in Europa und machen 46 % der Todesfälle bei Frauen und 39 % bei Männern aus. Daher sind sichere und genaue Diagnose- und Interventionsmethoden von entscheidender Bedeutung. Die derzeitigen Verfahren beruhen auf Röntgenstrahlen, welche auf krebserregender ionisierender Strahlung basieren, oder auf Ultraschall (US), der einen erfahrenen Kliniker erfordert, ergonomisch ungünstige Arbeitsabläufe aufweist und anfällig für Artefakte ist. Da es sich bei US jedoch um eine sichere, kosteneffiziente und weithin verfügbare Bildgebungsmethode handelt, ist es lohnenswert, diese Methode für Diagnosen und Eingriffe zu nutzen und die bestehenden Nachteile durch die Anwendung und Entwicklung innovativer Technologien zu überwinden. Dazu werden in dieser Arbeit Augmented Reality (AR)-Anwendungen und spezielle Trackingmethoden entwickelt und evaluiert, die die US-basierte vaskuläre Diagnostik und endovaskuläre Interventionen unterstützen und vereinfachen sollen.

Für die vaskuläre Diagnostik wurde ein System entwickelt, das den Arzt während der Untersuchung durch eine intuitive Augmented-Reality-basierte in-situ Visualisierung und eine anschließende automatische Gefäßsegmentierung unterstützt. Zu diesem Zweck wurde eine neue Inside-Out-Trackingmethode entwickelt, die es dem AR-Head-Mounted-Display (HMD) ermöglicht, die Sonde räumlich zu verfolgen, ohne dass ein externes Trackingsystem erforderlich ist. Ausführliche Tests ergaben, dass das Tracking mit einer mittleren Genauigkeit von 1,98 mm/1,81° für die statische Konfiguration durchgeführt werden konnte. Der mittlere Fehler in einem dynamischen Szenario betrug 2,81 mm/1,70°. Die Segmentierung wurde durch die Implementierung eines Deep-Learning-Ansatzes gelöst. Das Ergebnis liefert dem Arzt eine robuste Angabe zur Lage und Größe der Arterie und erleichtert so den Diagnoseprozess. Das Netzwerk wurde anhand von US-Bildern der Femoralarterie gesunder Probanden trainiert und getestet, wobei es seine Tauglichkeit auf realistischen Bildern mit einem Dice-Wert von 0,82 bewiesen hat.

Zur Unterstützung bei endovaskulären Eingriffen wird in dieser Arbeit eine neuartige technische Konfiguration vorgestellt, die volumetrischen Echtzeit-3D-US durch ein AR HMD visualisieren kann, um somit den Gefäßzugang vor dem Eingriff zu führen. Für die Intervention selbst bietet die Applikation eine 3D-Visualisierung der Gefäßstruktur, einschließlich der aktuellen Position und Ausrichtung des endovaskulären Instruments relativ zur Struktur, wodurch eine Fluoroskopie potentiell überflüssig wird. Für die 3D-US-geführte Gefäßpunktion bietet ein Remote-

Rendering-Ansatz die erforderliche Rechenkapazität für eine ausreichend hohe Bildrate und minimale Latenzzeiten. Darüber hinaus zeigen die Experimente, dass 3D-US bei US-geführten Aufgaben zusätzliche Vorteile (u. a. eine kürzere Interventionszeit) gegenüber 2D-US-Bildern bieten kann, die in AR betrachtet werden. Das entwickelte Assistenzsystem für die endovaskuläre Intervention ermöglicht die Verfolgung von Instrumenten mittels elektromagnetischem Tracking und eine intuitive Visualisierung des 3D-Gefäßbaums, einschließlich der Position der Katheterspitze mit dem AR HMD. Eine eingehende Bewertung der Tracking-Genauigkeit, einschließlich der landmarkbasierten Registrierung, zeigte vielversprechende Ergebnisse mit einem mittleren Fehler von 1,38 mm.

Zusammenfassend werden in dieser Dissertation neuartige AR-Anwendungen vorgestellt, die das Potenzial haben, sowohl die vaskuläre Diagnostik als auch Interventionen mit Hilfe von Ultraschall und einfach einzurichtenden Tracking-Techniken zu erleichtern - ohne dabei auf den Einsatz von Röntgenstrahlen angewiesen zu sein. Die weitere Entwicklung von AR HMDs in Verbindung mit sicheren und neuartigen Bildgebungsmodalitäten wie der Magnetpartikel-Bildgebung, einschließlich nicht-rigider Registrierungsansätze, stellen wichtige zukünftige Forschungsbereiche dar.

Acknowledgments

During the last few years, I have received a lot of unforgettable support and help at work and in my private life. First of all, I would like to thank my supervisor Prof. Dr. Floris Ernst. I would like to start with the possibility of dedicating myself freely and on my own responsibility to the topic of this dissertation and receiving support when necessary. But above all, I would like to emphasize his mental support, the trust in me and his reliability towards me during difficult life situations. I know that this cannot be taken for granted, and I would therefore like to express my special thanks.

Furthermore, I would like to thank Dr. Verónica García-Vázquez. You helped me a lot while getting started in scientific work, and much of the way I work today I learned from you. I am very grateful for that, and I hope we will work together again at some point!

A big thank you to my colleagues at the Institute of Robotics and Cognitive Systems. I really appreciate our working atmosphere, which is characterized by respect, friendliness, helpfulness, and cordiality. Keep it up!

Finally, I would like to thank my close friends, my siblings, my parents and my partner. You are the main reason that I am where I am today. I know that I can always rely on you and that you make me a better person.

Mathematical Notation

In this thesis, standard mathematical notation is used such that scalars are represented as single letters, i.e., $a \in R^1$, vectors as bold letters, i.e., $\boldsymbol{w} \in R^{10}$, and matrices as bold capital letters, i.e., $\boldsymbol{M} \in R^{\{10 \times 10\}}$. Subscripts are used to denote elements in vectors, i.e., w_i is part of $\boldsymbol{w} = [w_1, w_2, \dots, w_i]$. The used letters for indices in this work are i, j and k. To denote coordinate systems, this work uses capital calligraphic letters such as, for example, $\mathcal{A}$. Functions are written as single letters, i.e., $x = f(y)$ which implements the transformation $f(y) : R^1 \rightarrow R^1$. Sets are written as capital letters, i.e., $X = \{\boldsymbol{x}_1, \boldsymbol{x}_2, \dots, \boldsymbol{x}_n\}$. For better understanding, subscripts for variables or functions might be used, i.e., s_{c}, which is the sphere center position.

Contents

1 Introduction

In this chapter, a brief introduction to vascular diseases is given. Hereafter, current diagnostic and interventional approaches are presented, including their drawbacks. On the basis of those, a system is elaborated that can overcome these disadvantages. Hereafter, these initial ideas are discussed on a more technical level, which finally leads to the research questions.

Contents

1.1 Vascular Diseases

Vascular diseases include a variety of diseases that affect the vascular system of the human body and manifest in arteries, veins and capillaries. Some examples of Cardiovascular Diseases (CVD) are briefly described below.

Atherosclerosis is a condition in which the interior walls of the arteries become dense and rigid as a result of the accumulation of plaque, which is composed of fatty deposits, cholesterol, and other substances. If this accumulation occurs within the extremity arteries, it can lead to ischemia and eventually to Peripheral Arterial Disease (PAD). An abnormal enlargement of the abdominal aorta, which supplies blood to the abdomen, legs and pelvis is called Abdominal Aortic Aneurysm (AAA). As a final example, strokes are defined as a condition in which the blood supply to the brain is interrupted. This may be due to an obstructed artery or a ruptured vessel resulting in ischemia of the brain [1, 2].

A recent review [3] showed that in Europe, CVD contributed to more than 3.8 million deaths annually, of which more than 2 million were women and less than 1.76 million were men. This amounted to 46 % of fatalities for women and 39 % of deaths for men. On the contrary, cancer, the second most frequent cause of death in Europe, was responsible for 24 % of all male fatalities and 20 % of all female fatalities. CVD therefore remain the most common cause of death in the European region. Within this work, the developed applications focus on facilitating diagnostics and interventions for two main vascular diseases, as these show the greatest potential for possible applicability. This is mainly due to the advantageous anatomical location, which is relatively superficial. The next two subsections explain in more detail the epidemiology of the chosen CVD and its causes.

1.1.1 Peripheral Arterial Disease

PAD is a vascular disorder that manifests itself in the arteries of the extremities. It is defined as the partial or complete occlusion of one or more peripheral arteries caused by atherosclerosis. Untreated PAD can lead to significant limb ischemia and finally amputation. PAD is one of the most common vascular disease with a prevalence of 14.5 % (age ≥ 70) [4]. Furthermore, the prevalence has increased by 34.4 % between 2005 and 2015 [5]. PAD is uncommon in younger people, but its prevalence increases sharply with age and significantly affects the elderly population (Figure 1.1(a)).

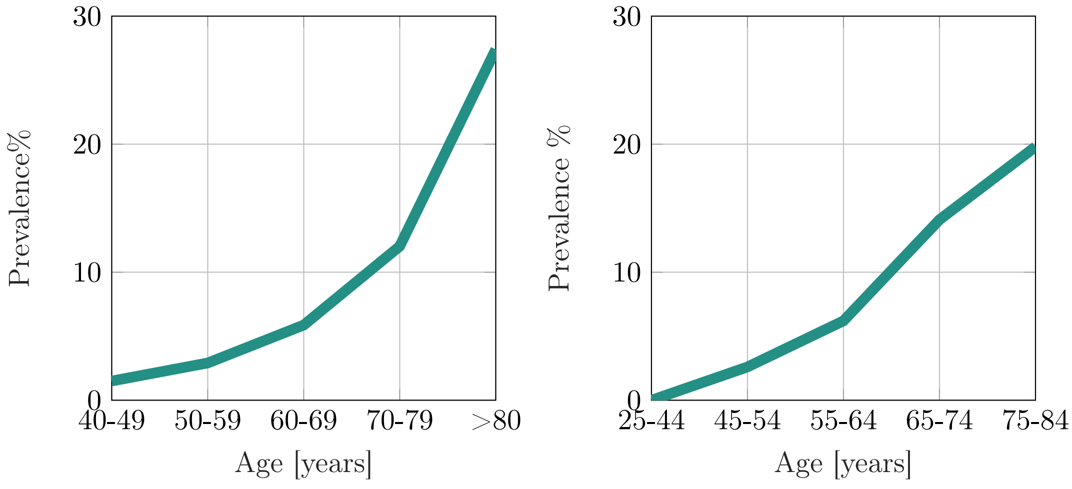

(a)

(b)

Figure 1.1: (a) Prevalence of PAD versus age (Data based on Allison et al. [6]). (b) Prevalence of AAA versus age for men (Data based on Singh et al. [7]).

1.1.2 Abdominal Aortic Aneurysms

The aorta is the largest artery in the human body that supplies blood to the abdomen, legs, and pelvis. Beginning at the aortic hiatus, the abdominal aorta terminates in the common iliac arteries (Figure 1.2). An AAA is a condition in which the wall of the aorta weakens and expands, forming a bulge or swelling. Over time, the aneurysm can enlarge and become more dangerous, as the weakened wall can burst and cause life-threatening bleeding. This is a potentially life-threatening condition with a prevalence of approximately 5 % [8], in which the massive hemorrhage after rupture leads to a fatality rate greater than 80 % [9]. Most AAAs occur in older adults (Figure 1.1(b)), particularly in men over 65 years of age, and are often asymptomatic until they enlarge or rupture. Smoking, hypertension, a family history of AAA and additional undiagnosed illnesses such as atherosclerosis are risk factors.

1.2 Diagnostic Approaches

1.2.1 Peripheral Arterial Disease

A systematic physical examination is required, although this alone has relatively low sensitivity and reproducibility [10]. Clinical indicators have prognostic relevance in addition to their diagnostic value. The ankle-brachial index, a suggested screening test for suspected PAD, confirms the condition in patients whose signs and symptoms point to lower limb ischemia [11]. For both, screening and diagnosis, Duplex

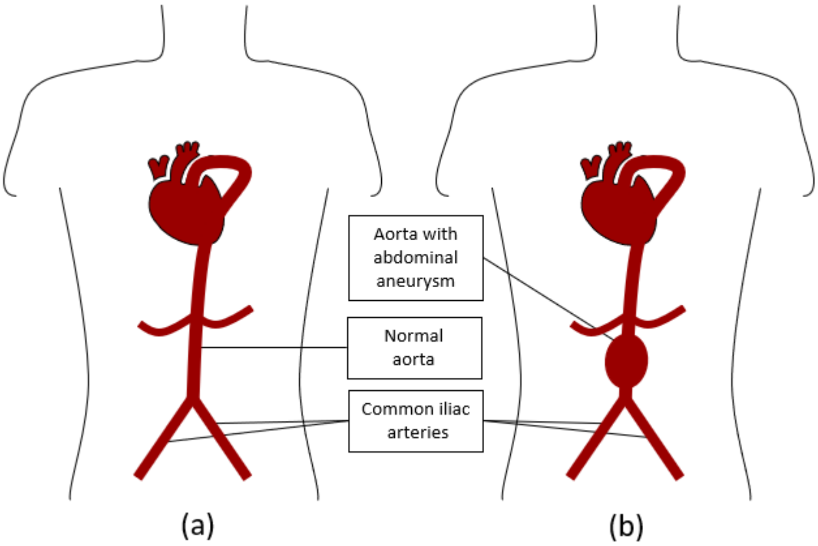

Figure 1.2: Illustration of a healthy aorta (a) and an aorta with an abdominal aneurysm (b).

Ultrasonography (DUS) is frequently the initial step in diagnosis. DUS uses B-mode echography, pulsed-wave, continuous, color, and power Doppler modalities to find, identify, and measure the size and severity of vascular lesions [10].

When imaging vessels, Computed Tomography Angiography (CTA) provides a short examination duration and few motion and respiration artifacts. Rapid, non-invasive capture, widespread accessibility, excellent quality, and 3D nature are all benefits of this imaging method. Furthermore, CTA shows a 'roadmap' of vascularization, which is important for choosing interventional approaches.

1.2.2 Abdominal Aortic Aneurysms

In 98.5 % of people undergoing screening, the infrarenal aorta can be accurately imaged by Ultrasound (US). In the remaining cases, a skilled sonographer should rescan the patient in a hospital setting after an overnight fast [12].

With high sensitivity and specificity, abdominal US and DUS are the first-line imaging methods for diagnosing minor AAAs. An important part of determining the severity of the condition and formulating and planning a treatment strategy plays CTA. Furthermore, CTA is a crucial tool in the post-repair follow-up process and is the imaging modality of choice for the diagnosis of a rupture. With the use of specialized post-processing software, CTA may offer a comprehensive data set of the entire aorta and access arteries, enabling, for example, analysis in three orthogonal planes, creation of a centerline, and precise measurement of diameter and length [12].

1.2.3 Disadvantages of Current Diagnostic Imaging Approaches

US has significant advantages over techniques such as Computed Tomography (CT) and Magnetic Resonance Imaging (MRI) due to its radiation-free, portable, widely available and real-time imaging capabilities. Nevertheless, US is a heavily user-dependent modality that necessitates highly competent and experienced sonographers for accurate exams. In addition to selecting the correct field of view, therefore maintaining focus on the screen of the US station, and holding the probe manually with the necessary amount of pressure, the examiner must also manually alter many imaging parameters on the US station. This unergonomic screening procedure may potentially result in musculoskeletal diseases associated with this workflow [13, 14]. Moreover, manual manipulation of the probe makes image acquisition very challenging to reproduce. While spatially and temporally separated image acquisition and diagnosis are typical for MRI and CT, sonographers are required to perform both simultaneously, making the examination more cognitively challenging. Furthermore, no ’roadmap’ is generated during the imaging process.

For CTA, on the other hand, lack of functional and hemodynamic data, radiation exposure, and the use of potentially nephrotoxic contrast chemicals are the most prominent disadvantages. While MRA does not require nephrotoxic contrast agent and is a radiation-free modality, it has inferior resolution, is relatively expensive, includes contraindications such as metallic implants and is more sensitive to motion artifacts [10].

1.2.4 Overcoming Current Limitations of Diagnostic Systems

Based on the previously mentioned shortcomings of present systems, a system will be defined that employs existing medical imaging technologies, but enhances them with particular visualization methods and post-processing procedures to provide a realistic and achievable approach to the ideal system.

This system provides the following most important key features:

1. Radiation and nephrotoxic contrast agents are not needed for imaging.

This specification excludes CT as a potential imaging modality. When comparing MRI with US, US stands out for its cost-effectiveness and real-time capability, which is why this work is limited to this modality. However, to overcome the drawbacks of US, the ideal system needs to offer additional features:

2. The system provides an intuitive and ergonomic visualization to enable easy, reproducible image acquisition;
3. It provides the physician with a ’roadmap’ for determining the severity of the condition and formulating and planning a treatment strategy;
4. The system enables spatially and temporally separated image acquisition and diagnosis and supports the physician in measuring the stenosis.

Inspired by Superman's X-ray vision (Figure 1.3), one may address the second point by superimposing the US image onto the real patient. By visualizing the image at the location of the actual imaged anatomy, the sonographer has direct feedback on the spatial relationship between the probe position and the imaged anatomy. Furthermore, this way of visualization reduces the need to constantly change gaze between the screen and the patient.

Figure 1.3: Superman's X-ray vision enables him to see regions of interest within the body (published November 1961 in Action Comics).

Augmented Reality (AR), which is the combination of real-world and computer-generated material, can be used to create such an in-situ visualization. The third and fourth point might be solved by creating a 3D image data set from sequentially acquired 2D US images. The sonographer's sweep along the artery with in-situ visualization can be utilized to spatially align the 2D images to a volume and hence create a so-called Tomographic Ultrasound (tUS) volume. The Infinity system (Figure 1.4, piur imaging, Vienna, Austria), which is already used in clinical practice, offers such a system for diagnostic purposes. However, the system relies on additional hardware to create the tUS. After acquiring the sweep, the physician can examine the artery for stenosis by looking at the volume and three orthogonal slices. A post-processing pipeline furthermore automatically segments the artery to facilitate diagnosis and stenosis measurement (Figure 1.5).

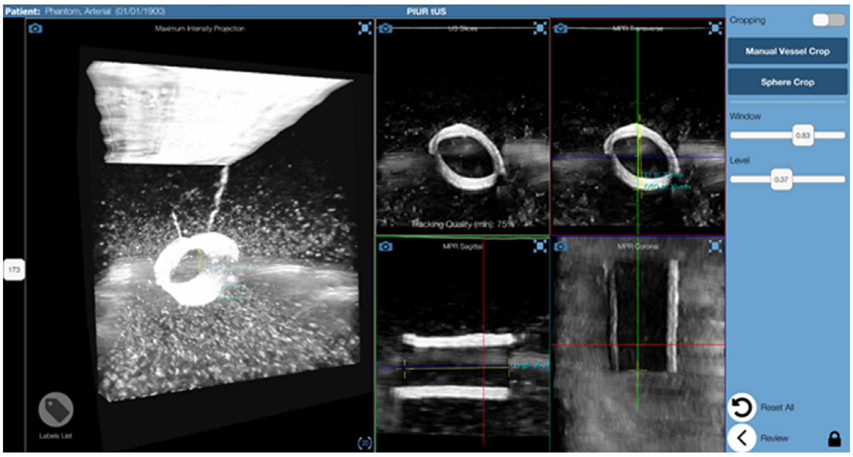

Figure 1.4: Graphical user interface of the piur Infinity system. Subsequently acquired 2D US images are spatially stacked to create a tUS. The interface displays the volume rendered image and three orthogonal slices. This figure was published in [15], Copyright Elsevier (2019).

To summarize, the ideal system offers three main features:

1. It provides an AR-based in-situ visualization of US images;
2. During acquisition the images are stored and hereafter spatially aligned based on the US probe position and orientation;
3. Post-processing software provides the segmented artery for computer-assisted stenosis measurement.

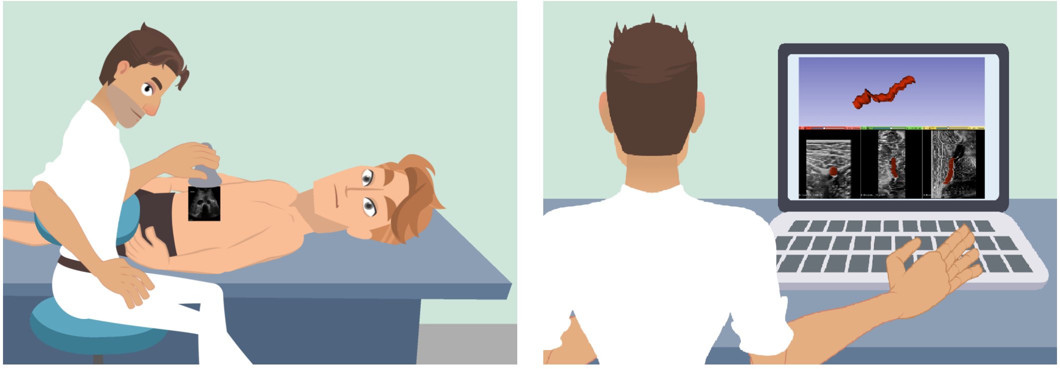
(a) (b)

Figure 1.5: (a) Sketch of the ideal diagnostic system for image acquisition. The physician holding the probe sees the US image in-situ while acquiring a sweep along the artery. (b) Sketch of the ideal diagnostic system for analysis. After the acquisition, the physician can investigate the pathology using the generated tUS image.

1.3 Interventional Approaches

General CVD prevention is of the utmost importance, and multidisciplinary care is required. The best medical therapy encompasses cardiovascular risk factor management, including pharmaceutical therapy, in addition to non-pharmacological measures like quitting smoking, adopting a balanced diet, losing weight, and engaging in regular physical activity. The pharmacological component of medical treatment consists of antihypertensive, lipid-lowering, and antithrombotic medications. As indicated, optimal glucose control should be achieved in individuals with diabetes [10, 12]. However, in some circumstances, conservative treatment is no longer sufficient, necessitating interventional techniques.

Endovascular interventions cover minimally invasive treatments to treat vascular diseases within the vessel. Vascular surgeons employ catheters to access arteries and veins during endovascular surgery. These types of surgeries are less invasive than conventional open surgical procedures and can offer advantages such as reduced hospital stays, reduced chance of complications and discomfort, reduced recuperation time and shorter recovery time [16, 17].

1.3.1 Vascular Access

For endovascular interventions, an accurate puncture of the common femoral artery in the groin to provide an access port is necessary to begin the actual intervention. Reported femoral access site complications range from 0 % to 17 % and include, among others, hemorrhage, pseudoaneurysm, and limb ischemia [18]. To locate the femoral artery within the groin, the physician may either palpate the pulsating artery or use US imaging as an image guidance modality. US-guided access of the femoral artery, however, is associated with lower access-related complications and higher efficacy rates [19].

1.3.2 Peripheral Arterial Disease

Revascularization may be advised if leg pain is so severe that it interferes with daily activities or if the symptoms have not improved with conservative treatments. The original interventional approach for PAD is to establish a bypass via open surgery to circumvent a vascular stenosis or occlusion.

However, the establishment of endovascular techniques has significantly changed the current treatment. Sven-Ivar Seldinger established the so-called Seldinger technique in 1952 [20], which serves as the foundation for endovascular procedures. Here, the target vessel, usually the femoral artery, is first punctured percutaneously with a hollow needle. A guide wire is then placed in the vessel via the needle. The endovascular instrumentation, such as catheters, balloons, stents, etc., can hereafter be advanced via this intravascular wire to the affected location under controlled X-ray fluoroscopy. An inflatable balloon is then placed at the location of the stenosis. There, aqueous fluid is used to gradually raise the balloon's pressure to a range of 6 to 20 bars (Figure 1.6). In order to less severely or permanently impede blood flow, the technique widens constrictions, which are typically the result of atherosclerotic changes. The majority of current angioplasty procedures also include the insertion of a short stent, which is in principle a wire mesh tube, into the artery. In order to promote more blood flow, the stent is kept in place permanently [21].

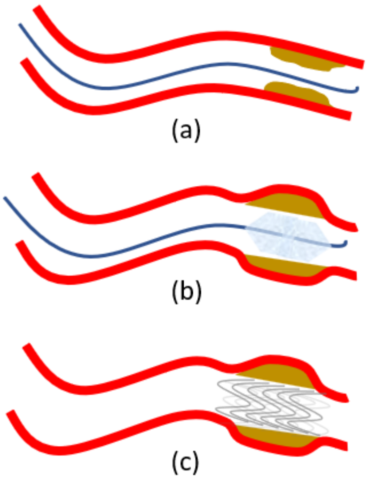

Figure 1.6: Sketch of the endovascular approach for PAD. (a) The guide wire is moved along the artery until the pathology is reached. (b) A balloon catheter is inflated at the pathology's position to widen the narrowed vessel. (c) A stent graft providing radial support in the blood vessel lumen is placed permanently at the same position.

1.3.3 Abdominal Aortic Aneurysms

Currently, aorta diameter rather than volume data are used to support the threshold for minor AAA repairs. The balance between the danger of aneurysm rupture and the risk of operational mortality for aneurysm repair guides the immediate choice regarding the size at which an aneurysm should be treated [12].

According to recommendations [12], males should have an AAA that is at least 5.5 cm in diameter before considering elective surgery to repair it. The limit for pursuing AAA repair in women with tolerable surgical risk may be $>5.0\,\text{cm}$. Around $80\,\%$ of surgical procedures are minimally invasive [22]. During this interventional approach, a stent graft, introduced at the patient's femoral arteries, is placed endovascularly within the aorta such that the blood passes through the aneurysm while depressurizing the aneurysm sac (Figure 1.7).

Fluoroscopy and Digital Subtraction Angiography (DSA) provide tool guidance during this procedure (Figure 1.8). In the last decade, Endovascular Aortic Repair

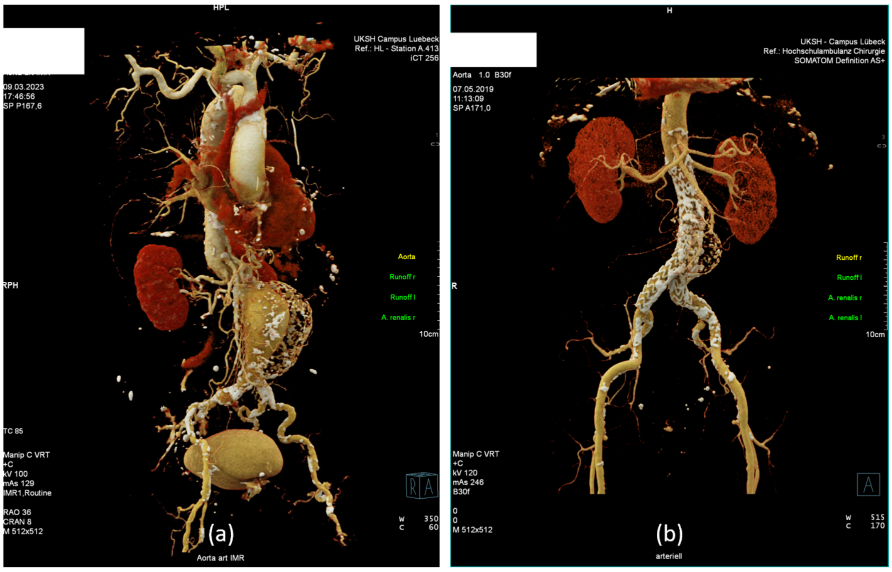

Figure 1.7: Rendering of CTA data of an AAA (a) before and (b) after EVAR. Images used with permission from Malte Sieren (Department of Radiology and Nuclear Medicine, University Hospital Schleswig-Holstein Campus Lübeck).

(EVAR) has become the standard intervention due to medical technology advancements. Advantages of EVAR compared to open treatment include lower perioperative morbidity and mortality [16]. However, they introduce certain drawbacks that will be discussed in the following.

1.3.4 Disadvantages of Image-Guided Interventional Approaches

As femoral artery access is usually guided by US imaging, the same drawbacks as mentioned in Section 1.2.3 exist. However, in the case of US-guided vascular puncture, the display of the US image on the station screen is even less advantageous as the physician must simultaneously puncture within the target anatomy. A pronounced hand-eye coordination is even more important during this procedure. In this context, 2D US has the risk of out-of-plane imaging, which requires the interventionist to constantly position the probe to view both the needle and target anatomy.

The requirement of employing X-rays for navigation of endovascular instruments and nephrotoxic contrast agents for angiography remains an unresolved issue in endovascular interventional procedures. Although technological advancement and compliance with radiation protection measures have already resulted in a decrease in radiation [23, 24], patient and surgeon radiation exposure is still considerable due to more sophisticated operations requiring lengthy fluoroscopy duration. Additionally,

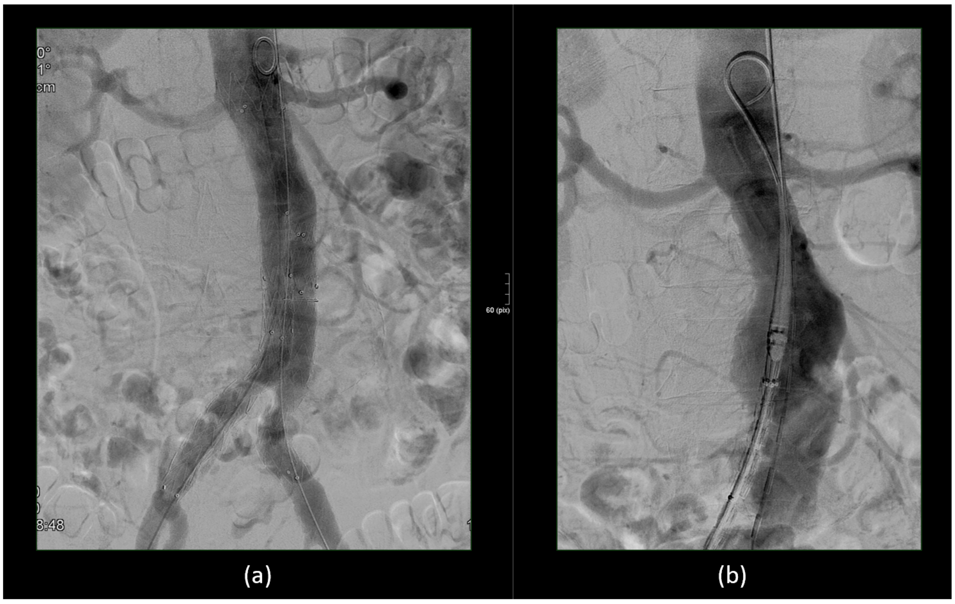

Figure 1.8: DSA images of the abdominal aorta and renal arteries (a) before and (b) after EVAR. Images used with permission from Malte Sieren (Department of Radiology and Nuclear Medicine, University Hospital Schleswig-Holstein Campus Lübeck).

fluoroscopy and DSA are 2D projection imaging modalities and therefore miss any depth information, which may as well lead to longer surgeries.

1.3.5 Overcoming Current Limitations of Endovascular Interventions

As before, the aim is to elaborate a system that overcomes the mentioned drawbacks while keeping in mind that the approach should be realistic and achievable. Because femoral access and endovascular intervention are two separate substeps with different requirements, two different ideal systems are discussed.

Since the femoral access system does not require subsequent analysis of the image data, an ergonomic and intuitive in-situ visualization of the US image is sufficient in this case. Therefore, the physician can see both the target anatomy and the needle in their true position and orientation. To overcome the drawback of out-of-plane imaging, a volumetric image of the target anatomy and the needle would be necessary. Recently, real-time volumetric US has gained popularity since new matrix array probes give sufficiently high frame rates and improved image quality for several medical applications. Hence, for this application, an in-situ visualization of real-time 3D US could overcome the drawback of out-of-plane imaging.

For endovascular interventions, on the other hand, the system should have the following specifications:

1. No radiation and nephrotoxic contrast agent is needed;

2. The system shall provide 3D information of the vascular anatomy and the relative position and orientation of endovascular tools;
3. It shall provide visualization that enables depth perception.

According to the first specification, the system will not rely on fluoroscopy and nephrotoxic contrast agents. To provide 3D information, a 3D model of the aorta or peripheral arteries can be displayed. This 3D model can be based on medical imaging data acquired during the diagnostic process. To visualize the position and orientation of the tools with respect to the artery, the system requires spatial registration and continuous tracking of the instruments. To provide depth perception for the virtual 3D content, a stereoscopic display worn by the physician can be used. To summarize, the ideal system consists of three main steps (Figure 1.9):

1. The system visualizes a 3D model of abdominal aorta or peripheral arteries based on preinterventional medical imaging data;
2. A spatial registration and continuous tracking enable to visualize the instrument's position with respect to the artery 3D model;
3. A stereoscopic display enables depth perception of the content.

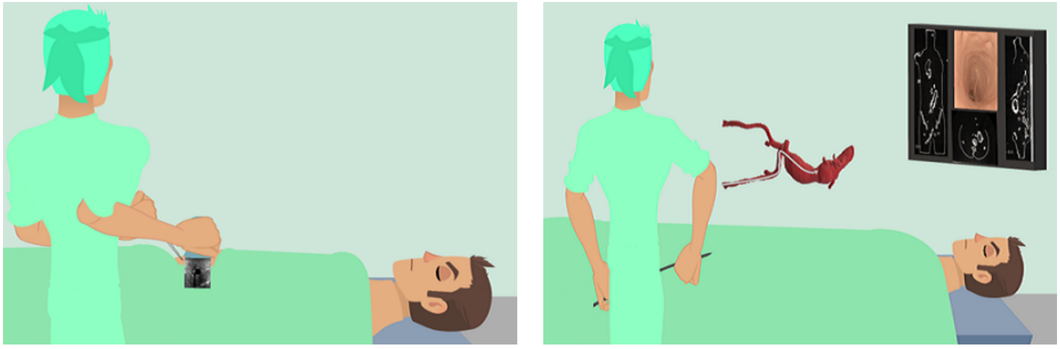

(a) (b)

Figure 1.9: (a) Sketch of the ideal interventional system for image guidance during vascular access. The physician holding the probe sees the 3D US image in-situ while advancing towards the femoral artery. (b) Sketch of the ideal interventional system for image guidance during the endovascular intervention. The physician sees a virtual 3D model of the artery (red) and the endovascular tools (grey) to navigate the guide wires and catheters towards the pathology.

1.4 Aims and objectives of this work

The preceding chapters provide the reader with a general context, including the medical justification for the necessity of innovative systems. Furthermore, possible visions are presented that can overcome previous disadvantages. Previously formed concepts are now addressed on a technical level, and scientific obstacles and, hence, research questions are formulated as a result. This work does not aim to present a complete ideal system but rather tries to answer scientific questions about the most important features within these concepts.

In order to facilitate vascular diagnostics, the system should provide an AR-based in-situ visualization of US images. On a technical side, the system therefore needs to, first, stream US images with minimum latency and, second, spatially track the US probe to visualize the image in the correct position and orientation. Minimal technical complexity is favorable to not make the diagnostic process more laborious. Hence, the first research question can be formulated as:

RQ1 How can the probe be tracked with minimal technical complexity, and how accurate is the tracking?

Hereafter, the system needs to stack the images in space to create a tUS. Due to the knowledge of the probe and image pose, these images can simply be stacked using any medical image computing and visualization platform. However, it is also necessary to automatically segment the arteries in the images. Since US is known for its high noise level and poor signal-to-noise ratio, simple image processing steps might not be sufficient for an accurate segmentation. Therefore, the second research question is:

RQ2 How can arteries be reliably segmented in US images, and what accuracy is achievable?

In addition to tracking the probe, the guidance system facilitating vascular access has to stream 3D image data and enable appropriate volume rendering of the 3D US data. Especially for stand-alone AR devices, which usually have very limited computing capacity, the challenge is to ensure volume rendering at a target refresh rate of 60 Hz for a smooth and realistic visualization. Furthermore, with the continuous transfer of large amounts of data, the challenge is to assure low latency when displaying the volumes in-situ. In summary, these challenges can be framed as the following questions:

RQ3 Is it possible to provide a target frame rate of 60 Hz when rendering US volumes on a stand-alone AR device? Can the system achieve a latency close to real-time perception?

To facilitate endovascular interventions, vascular 3D models need to be generated based on preinterventional imaging data. This can be performed either using the tomographic US set or a CTA data set. To visualize the endovascular instruments within the 3D model, the models and instruments must be spatially registered and the tools continuously tracked. Since there is no line-of-sight between an external optical tracking system and endovascular tools, an appropriate tracking approach must be found.

RQ4 How can we register the vascular 3D model with the tracked endovascular tools for a combined visualization? Which tracking approach can be utilized for this kind of intervention, and what accuracy is achievable?

These questions will be investigated and addressed in the subsequent chapters, which will be as self-contained as feasible for the purpose of thoroughness and readability. This implies that methods and outcomes are only detailed and discussed inside the chapter in which they are utilized.

The workflow of a typical vascular treatment served as inspiration for the remaining three main sections of this work (Figure 1.10). The research questions **RQ1** and **RQ2** belong to the diagnostic phase and will be addressed in Chapter 3. On the other hand, **RQ3** and **RQ4** can be assigned to the interventional part, which is located in Chapter 4. Finally, in Chapter 5, a summarizing discussion takes place.

Figure 1.10: Workflow of vascular treatments. **RQ1** and **RQ2** are part of vascular diagnostics while **RQ3** and **RQ4** can be assigned to vascular interventions.

2 Key Technologies and Methodologies

For ease of reading, the following chapters will be maintained as independent as possible. As a result, only the chapters in which the technologies and methodologies are actually employed are addressed. However, this chapter will be an exception. It will go into great detail about important technologies and methods and outline them. Key technologies and methodologies are those that are applied consistently across the whole dissertation and are thus the most pertinent. Nearly all of the next chapters will require prior understanding of the contents outlined here.

Contents

2.1 Mixed & Augmented Reality

In this section, a first definition for AR is given, followed by an explanation of the reality-virtuality continuum concept, an introduction to different types of AR visual output devices and a more detailed description of the AR glasses HoloLens, which are used throughout this work.

In general, AR can be defined as an (immediate, interactive and real-time capable) extension of the perception of the real environment by virtual contents (for any senses), which are oriented as far as possible to reality in their characteristics and appearance, so that in extreme cases (if this is desired) a distinction between real and virtual (sensory) impressions is no longer possible [25].

2.1.1 The Reality-Virtuality Continuum

The term mixed reality was introduced in 1994 by Milgram et al. [26]. They differentiate three states that actually form a continuum (Figure 2.1(a)): The purely real environment, the virtual environment and a mixed state. Accordingly, any environment that consists of virtual and real elements can be considered as mixed reality. Depending on the amount of virtual content in the environment, they further differentiate between AR and augmented virtuality, while both are considered as mixed reality.

Roughly two decades later, Skarbez et al. [27] try to refine the initial idea. They argue that the reality-virtuality continuum is actually not a continuum because a complete virtual environment is not achievable. A fully virtual setting would only be achieved if the user experienced intero- and exteroceptive senses. They mention the famous movies *Matrix* as an example, in which those senses are stimulated via electrodes attached to the brain. Therefore, they propose a slightly different reality-virtuality continuum (Figure 2.1(b)). Here, a discontinuity on the right side marks the 'Matrix-like' environment. The external virtual environment defines a domain in which all exteroceptive senses are stimulated while the interoceptive ones stay unaltered.

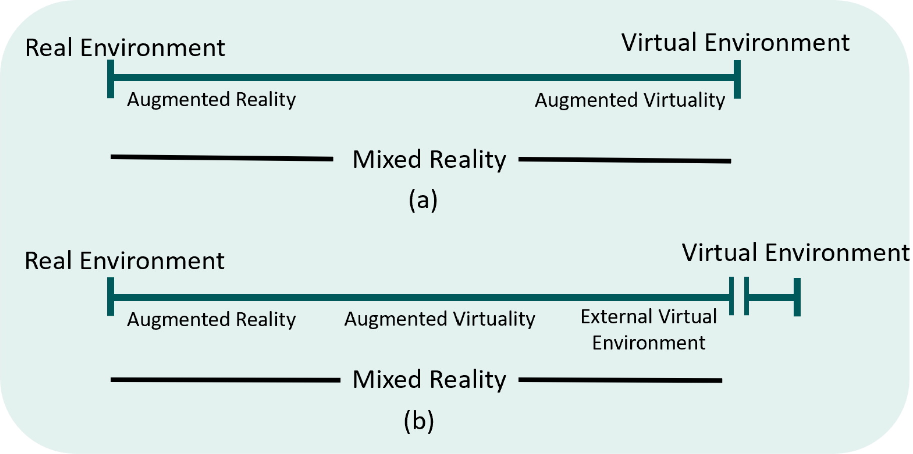

Figure 2.1: The reality-virtuality continuum according to (a) Milgram et al. [26] and (b) Skarbez et al. [27].

As the definition of mixed reality by Skarbez et al. appears to be a more accurate description, this work follows this interpretation. Since in the presented applications the real world is enhanced with virtual content rather than vice versa, the term AR is applied throughout this work.

2.1.2 Augmented Reality Visual Output Devices

There are several methods to perceive an AR world using diverse visual output devices. The most simple form is a standard screen that visualizes the real world, including the virtual content. Hereafter, handheld devices such as smartphones and tablets can be considered more advanced visual output device (Figure 2.2). These have a camera on the back, which is used for recording the real environment and optical tracking, and usually have corresponding sensors for detecting position and orientation. Augmentation is usually based on the perspective of the camera pose, but not on the actual viewing angle of the user [25]. Furthermore, the user is required to hold the device in her or his hands and is therefore not able to use them for other tasks.

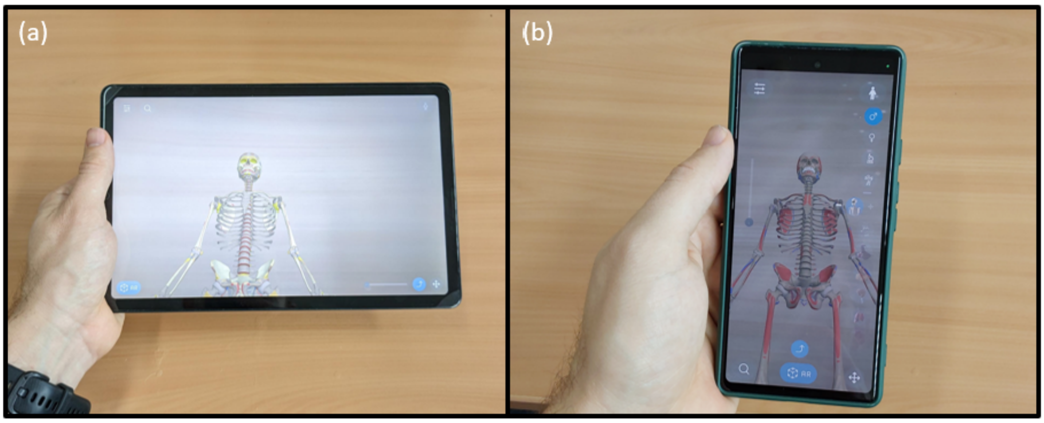

Figure 2.2: Medical AR applications for a tablet (a) and a smartphone (b) visualizing an anatomical model in the real world.

A Head-Mounted Display (HMD) is a technology worn on the head that allows users to visualize information directly in their field of vision. Monocular HMDs comprise a single display that is concurrently captured by each eye. Binocular HMDs, on the other hand, have one screen per eye, enabling stereoscopic vision. HMDs can further be divided into Video Pass-Through (VPT) and Optical See-Through (OST) devices. VPT displays are HMDs like those commonly used for Virtual Reality (VR). In contrast to the use in VR, however, a video of the reality is superimposed in such a way that the user has the impression of being able to view the environment through the glasses. To this end, one or more video cameras are attached to or directly integrated into the HMD. The recorded video is correctly inserted as a background image when the scene is rendered, including virtual elements. In most cases, the video cameras cannot be placed directly in front of the eye's ray path. Thus, in addition to the undistortion of the camera image, a translational and/or rotational offset must often also be considered during the perspective correction of the camera image [25]. State-of-the-art VST-HMDs, which are as well VR-HMDs, are the VIVE Pro 2 (HTC, Taiwan ROC), Valve Index (Valve Corporation, WA, USA), Quest Pro (Meta, CA, USA) and Varjo XR-3 (Varjo Technologies Oy, Helsinki, Finland). Their specifications are summarized in Table 2.1.

Table 2.1: Technical specifications of state-of-the-art VST-HMDs.

	Display Resolution	**Diagonal Field-of-View**	**Max Refresh Rate [Hz]**	**Weight [g]**	**Stand-alone Device**
VIVE Pro 2	2448 × 2448	116°	120	850	No
Valve Index	1440 × 1600	108°	144	809	Yes
Quest Pro	1920 × 1800	106°	90	722	Yes
Varjo XR-3	1920 × 1920	134°	90	594	No

Similar to VPT displays, OST displays allow virtual objects to be superimposed on the viewer's field of vision. However, these types of devices enables a direct view of the real world, facilitated by their transparent displays. While the view of reality is always direct and thus immediate, the virtual content is optically superimposed. Therefore, in contrast to VPT displays, there are no restrictions in terms of quality, latency and resolution when viewing the real environment – providing a clear advantage. On the downside, due to the display technology, they have Field-of-View (FOV) and contrast restrictions and need further calibration to account for the user's specific eye locations. The most used and state-of-the-art OST-HMDs are Magic Leap 1 & 2 (Magic Leap, FL, USA) and HoloLens 1 & 2 (Microsoft, WA, USA). The most important specifications are summarized in Table 2.2. While Magic Leap 2 offers the biggest FOV, HoloLens 2 facilitates intuitive interaction with virtual elements by means of hand gestures and voice commands. Throughout this work, several AR applications have been developed for HoloLens 1 & 2, which is why the next section explains the system and its sensors in more detail.

Table 2.2: Technical specifications of state-of-the-art OST-HMDs. Table adapted from M. Doughty et al. [28] under CC-BY license.

	HoloLens 1	**HoloLens 2**	**Magic Leap 1**	**Magic Leap 2**
Optics	Waveguide	Waveguide	Waveguide	Waveguide
Resolution	1268 × 720 px	2048 × 1080 px	1280 × 960 px	1440 × 1760 px
Field of View	30 × 17.5°	43 × 29°	40 × 30°	44 × 53°
Stand-alone Device	Yes	Yes	Yes (External pad)	Yes (External pad)
SLAM	6 DOF	6 DOF	6 DOF	6 DOF
Eye Tracking	No	Yes	Yes	Yes
Weight	579 g	566 g	345 g	260 g
Interaction	Head, hand, voice	Hand, eye, voice	Controller	Eye, controller
Release Year	2016	2019	2018	2022
Price	$3000	$3500	$2295	$3299

2.1.3 HoloLens 2 and Its Sensors

HoloLens was first introduced in 2016 by Microsoft and has since become a key driving factor in medical augmented reality research [29]. This HMD produces stereoscopic images on the see-through display such that the user perceives volumetric images of the virtual elements. Built-in computer vision algorithms such as Simultaneous Localization and Mapping (SLAM) enable to locate the pose of the device in the environment [30]. Since its release, it has been used in many cases, such as medical and surgical aids, medical education, industrial engineering, architecture, civil engineering, etc. [28, 31].

The second version of the OST-HMD, HoloLens 2, was introduced in 2019. Both devices possess similar sensors and capabilities. However, the main improvements of the second version are advanced hand tracking capability, increased FOV, eye tracking sensors and higher wearing comfort (Table 2.2).

HoloLens 2 comprises several sensors, such as four grayscale cameras to perform real-time visual-inertial SLAM, an inertial measuring unit, a depth camera for hand tracking and to compute spatial mapping, an eight megapixel RGB camera and a microphone array with five channels (Figure 2.3). The so-called research mode enables access to most of these sensors [32]. Throughout this work, the research mode in HoloLens 2 was utilized for several tracking and registration tasks, which is why a more detailed explanation is of interest.

The HoloLens 2 incorporates four grayscale head-tracking cameras and a depth camera for environment perception and articulated hand tracking. In addition, it is equipped with two extra infrared cameras with accompanying LEDs for iris and eye monitoring. Two of the grayscale cameras are set up as a stereo configuration to capture the space in front of the device and for triangulating the total depth of tracked visual features. The two additional grayscale cameras aid in monitoring features by providing a wider field of view. These synchronized global-shutter cameras are capable of taking images at up to 30 frames per second and are more sensitive to light than the color camera. To calculate depth, the depth camera uses phase-based time-of-flight and active infrared (IR) illumination. The camera has two operational modes. The first mode provides low-framerate far-depth sensing (1–5 Hz), which is presently used for spatial mapping, whereas the second mode facilitates high-framerate near-depth sensing (45 Hz), which is typically used for hand tracking. The HoloLens 2 conserves energy by decreasing the number of illuminations, resulting in depth wrapping beyond one meter. This camera's actively illuminated infrared images (in both modes) are largely unaffected by ambient light, making them useful even without the depth information they provide. Although the Azure Kinect employs slightly altered depth modes, the sensor device is identical. HoloLens 2's Research Mode also provides access to the magnetometer, accelerometer and gyroscope readings. In order to protect the privacy of users, raw eye-tracking camera images are not accessible in Research Mode. Researchers can obtain eye-gaze directions using presently available APIs [30].

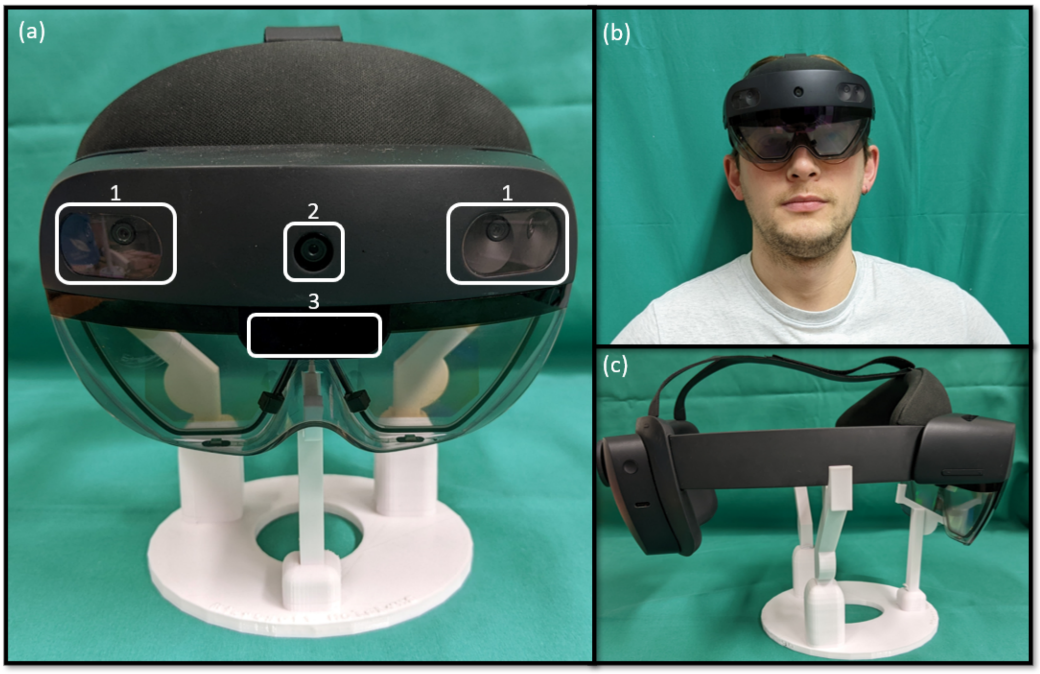

Figure 2.3: (a) Front view of HoloLens 2 with the highlighted four grayscale head-tracking cameras (1), the RGB camera (2) and the depth camera (3). (b) User wearing the OST-HMD. (c) Side view of HoloLens 2.

2.2 Ultrasound

The diagnostic imaging technique most frequently used in clinics around the world is US. It also offers a lot of important benefits for adopting it as a modality for image guidance. In comparison to previously mentioned advantages for vascular diagnostics, these are in general:

- Non-invasive: US does not involve any incisions or the use of radiation, making it a safe and painless option for patients.
- Real-time imaging: US produces images in real-time, which allows healthcare providers to see the structure and function of internal organs and tissues as they are being examined.
- Portable: US machines are portable and can be used in a variety of settings, including hospitals, clinics, and even at the patient's bedside.
- Versatility: US can be used to visualize a wide range of organs and tissues in the body, including the heart, liver, kidneys, and uterus.

However, this imaging modality also has several major drawbacks:

- Limited imaging depth: US has limited penetration depth and may not be able to produce high-quality images of deeper structures in the body.
- Poor bone visualization: US cannot image bone structures.
- Operator dependence: The quality of the images produced by US can depend on the skill and experience of the operator, and may be subject to interpretation.
- Limited in certain patient populations: US may be less effective in certain patient populations, such as those who are obese or have a lot of abdominal scarring.

In general, US is a useful medical imaging modality that can be a valuable tool for the diagnosis and management of a wide range of medical conditions. To better understand its use in image guidance, just the fundamental physical principles of US imaging will be discussed in the next sections of this work.

2.2.1 Physical Principles of Ultrasound Imaging

US imaging is a reflection imaging method in which the reflected amplitudes of previously emitted longitudinal sound waves are used to generate an image of the anatomy. The transmitter and receiver are combined into a single unit to ensure independent placement. This unit, namely the US probe, can then be placed anywhere on the body. Within the probe, many piezoelectric crystals are typically arranged in a line.

These crystals deform when an electrical voltage is applied and the other way around. Therefore, they can be used to produce sound waves or generate an electronic signal based on received ones.

When an US wave travels through tissue, it is attenuated by four main mechanisms: absorption, reflection and refraction, scattering, and divergence. Reflection is the main contributor to anatomical-morphological information. Therefore, this mechanism is explained in more detail.

If a wave hits an interface between tissues with different acoustic properties, a part of it is reflected, analogous to the light reflections on the surface of a pane of glass. The more different the acoustic impedances of the adjacent media are, the more of the initial wave is reflected. The acoustic impedance Z results from the product of density ρ and sound velocity c:

$$Z = \rho \cdot c \tag{2.1}$$

Different impedances lead to reflections of the US wave at interfaces, which in turn form the basis for the generation of the US image. According to the reflection coefficient R, the intensity of the sound wave (I_0) is partially reflected (I_{Echo}) at tissue borders with varied Z values:

$$I_{Echo} = R \cdot I_0 = \frac{(Z_1 - Z_2)^2}{(Z_1 + Z_2)^2} \cdot I_0 \tag{2.2}$$

At an interface between media with vastly differing acoustic impedances, for instance between soft tissue and bone, nearly the full irradiated intensity is reflected. ('total reflection'). With almost 100 % reflection, no significant ultrasonic energy can overcome the interface any more. This means that objects behind this interface are no longer detected, leading to an US artifact called acoustic shadowing [33].

2.2.2 2D and 3D Ultrasound Probes

As explained above, for a probe that generates 2D images (referred to 2D probe) piezoelectric crystals are arranged in a 1D array (Figure 2.4). There are two distinct probe types to generate US volumes. The first type consists of a crystal array moved back and forth in a housing filled with oil (Figure 2.5(a)). This housing is firmly coupled to the surface of the skin via a sound-permeable cap during data recording and enables the recording of a series of adjacent 2D slices. Common application areas of these probes are obstetrics, abdominal and pediatrics.

The second type uses a two-dimensional, grid-like array of ultrasonic transducers that can be controlled in any combination, either linearly or in sectors, to generate a 3D ultrasonic field without delays caused by the mechanical back-and-forth movement of components. As a result, these matrix array probes offer sufficiently high frame rates for a variety of medical applications, ranging from obstetrics and abdominal areas (Figure 2.5(a)) to vascular diagnostics (Figure 2.5(b)). Due to the high cost of developing and producing 2D ultrasonic arrays, these probes are often relatively costly [34].

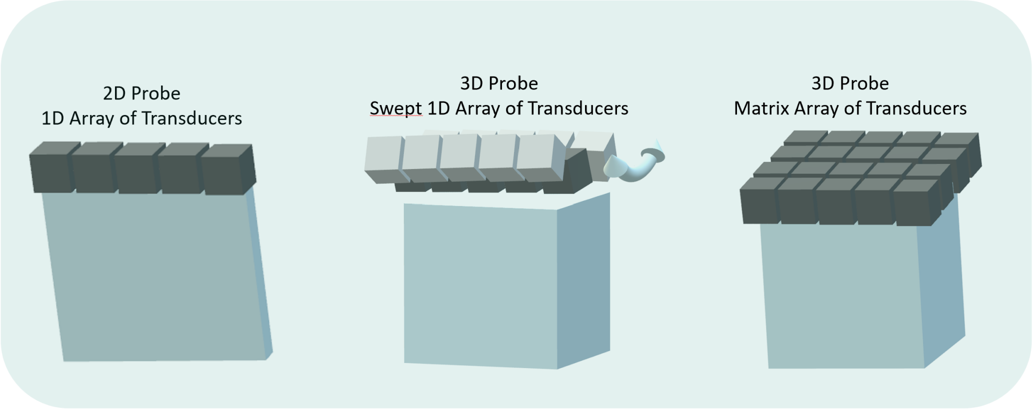

Figure 2.4: Illustration of the arrangement of piezoelectric crystals (transducers) for a 2D probe (left), a mechanically swept 3D probe (middle) and a matrix-array probe (right).

The fundamental benefit of 3D US is the possibility to visualize anatomical structures in 3D instead of a single cross-sectional slice, which in turn enables a more precise volume measurement and can facilitate more intuitive image guidance. It can also address some of the issues with 2D imaging, such as out-of-plane motion resulting in imaging of different undesired anatomical slices and a high mental task load for mentally aligning the 2D cross-sectional US image with the 3D anatomy.

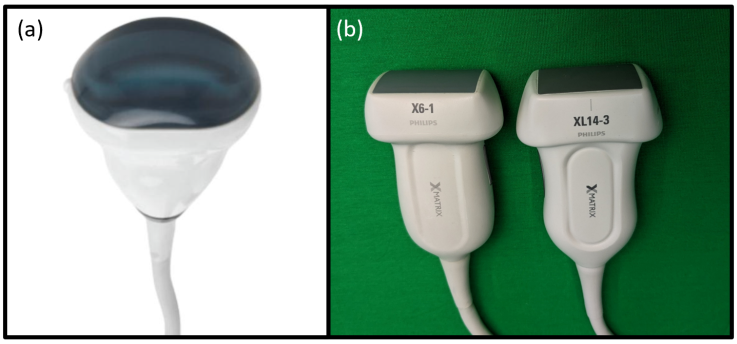

Figure 2.5: Different 3D US probes. (a) The 4DC7-3/40 probe from BK Medical uses a mechanically swept 1D array of crystals to produce US volumes. Image reprinted with permission from Strata Imaging. (b) While the XL14-3 (right) is used in vascular diagnostics, the X6-1 (left) probe offers a broader range of applications in abdominal and fetal diagnostics.

2.2.3 Ultrasound Image Guidance

Any surgery or intervention that uses enhanced imaging to localize, target, monitor and control treatments falls under the umbrella of Image-Guided Therapy (IGT), a field that largely encompasses the fields of interventional radiology and image-guided surgery. In IGT, imaging takes the place of or supplements direct visualization so that interventions are better targeted, less invasive, and have better results [35].

US-guided interventions, as a subdiscipline of IGT, entail moving an instrument to a specific target location as well as placing a transducer to image the target anatomy. Examples of procedures (Figure 2.6) include radiotherapy, stereotactic neurosurgery, percutaneous ablation, and biopsies [36]. Spatial tracking systems (Section 2.3), which indicate the position and orientation of objects in relation to a base coordinate system, can help to maintain spatial awareness while carrying out such tasks.

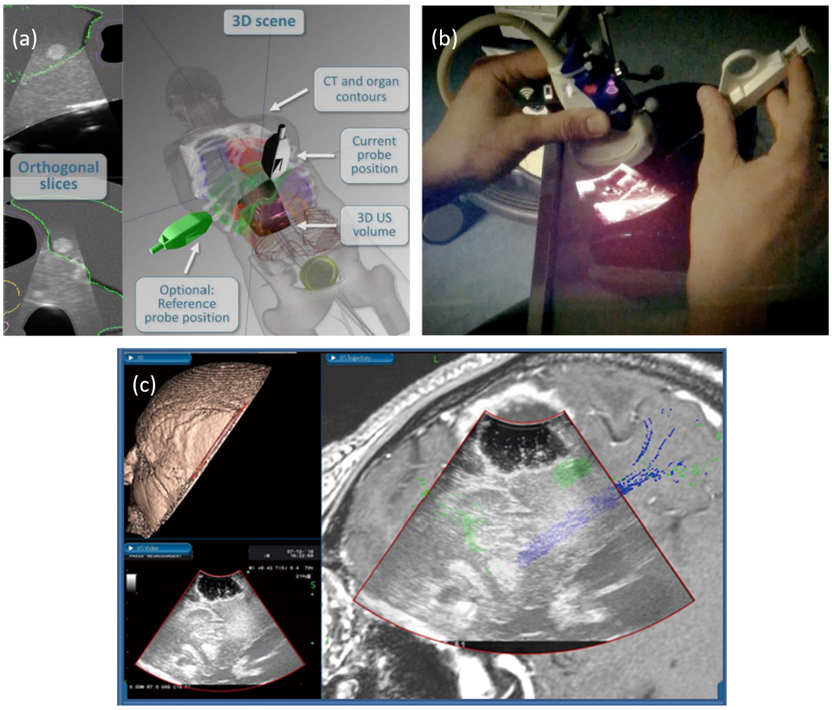

Figure 2.6: Examples of US guidance in therapeutic applications. (a) Guidance system to facilitate US probe placement in radiotherapy. The spatially tracked probe and the US volume are visualized with respect to a previously acquired CT and segmented organs (Copyright © [2018] IEEE. Reprinted with permission from [37]). (b) In-situ visualization of a 2D US image to guide needle placements (Figure by C. Rüger et al. [38] under CC-BY license). (c) Intraoperative US image overlaid on preoperative MRI image, including subcortical association fibers for neuronavigation (Figure by M. Ganau et al. [39] under CC-BY license).

Compared to other common image guidance modalities like CT, US offers unique benefits: CT produces detailed images of the body's internal structures, but does not provide real-time visualization. US, on the other hand, allows the physician to see the needle or other instruments as they are inserted, which can improve the accuracy of the procedure. Furthermore, CT, as discussed, uses ionizing radiation to produce images. US, on the contrary, uses sound waves and does not involve any harmful radiation. CT equipment is generally more expensive than US equipment, and CT-guided procedures may be more costly as a result.

2.3 External tracking devices

A crucial part of an IGT system are tracking devices. These tools are used to track the location of instruments in relation to the anatomy of the patient. Despite the fact that early tracking systems were simply mechanical digitizers, optical tracking methods were quickly adopted by the field due to their high precision and relatively large workspace. A line-of-sight must be ensured between the tracking device and the instrument to be monitored in Optical Tracking System (OTS), which is not always practical and prevents the monitoring of flexible devices within the body. As a result, Electromagnetic (EM) tracking systems were created that could follow objects such as catheters and needle ends within the body without requiring a line-of-sight. The selection of a tracking system depends heavily on the application and requires knowledge of the intended working volume and accuracy requirements [40]. Even though more tracking devices exist nowadays, the focus lies on optical and EM tracking, which are both used throughout this work.

2.3.1 Optical tracking

OTS are widely used in industry, which has led to the introduction of several manufacturers and system versions with a variety of characteristics. Clinical systems are a specialized area, and the technology behind them has not seen drastic changes in recent years. Optical systems can be divided into videometric tracking systems and infrared (IR)-based tracking systems [40]. The devices utilized throughout this work are all based on IR tracking. Hence, a further explanation of this technology is of interest.

An infrared camera is used as part of an OTS over the surgical site. Either Light-Emitting Diodes (LEDs) or markers with retroreflective material on their surface serve as the tracked markers. Since LEDs actively emit signals towards the cameras acting as receivers, position tracking utilizing these markers is defined as active tracking. Passive tracking is the process of tracking with self-reflective markers in which the camera unit can recognize those. As opposed to active markers, such as LEDs in an OTS or receiver trackers in an EM tracking system, passive markers in an OTS do not need tethering wires to supply power or synchronizing signals to the markers. Tracking accuracy is generally higher with active markers. Vendors use various proprietary techniques to identify markers [40].

In active tracking, position triangulation — which is carried out by rapidly flashing one LED at a time and detecting it by the cameras — is used to pinpoint the location of the monitored marker. In passive tracking (Figure 2.7), the centroid of the markers is determined by applying Gaussian fitting to the grayscale values of the markers visible in the camera images.

Despite being the most popular option for tracking in surgical navigation, optical tracking sensors are only useful if line-of-sight can be ensured. Before the operation begins, the position of the camera unit in the OTS must be carefully planned in order to minimize the line-of-sight drawback.

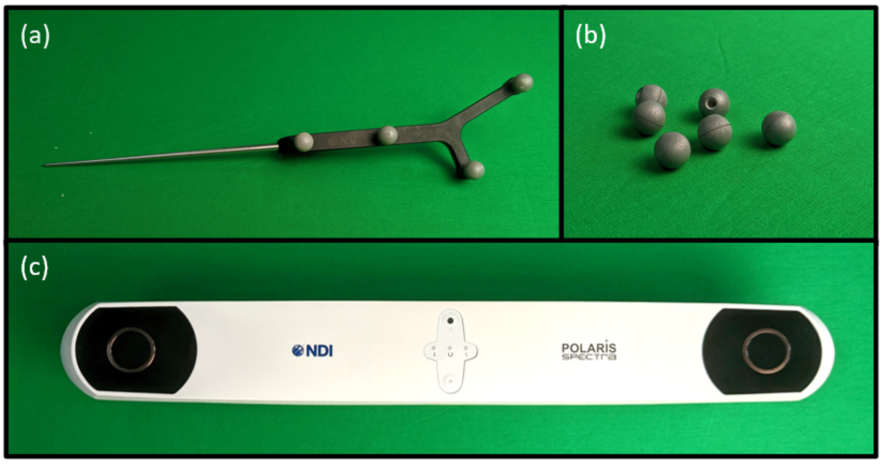

Figure 2.7: (a) Stylus (with attached retroreflective spheres) commonly used for landmark-based registration. (b) Retroreflective spheres with an opening to place them on specific holders. (c) Front view of the NDI Polaris Spectra optical tracking camera. The cameras are placed on the right and left side of the black part of the device.

2.3.2 Electromagnetic tracking

A more recent tracking approach used in medical applications is based on EM tracking. The key benefit is that there is no line-of-sight restriction, but drawbacks include being vulnerable to distortions from surrounding metal sources and having less precision than optical tracking. These devices pinpoint the location of tiny EM field sensors inside a specified EM environment. Therefore, a tracking system always consists of a field generator and sensors.

An alternating current magnetic localizer device called Aurora (Figure 2.8), NDI, Waterloo, Ontario, Canada) generates AC magnetic fields at a maximum frequency of 40 Hz. Small coil sensors that may be implanted in catheters, endoscopes, and other equipment are part of its system, along with a field generator and a control unit. Coils in the field generating unit produce an EM field, and voltages are induced in the embedded sensor coils of the tracked tools when they are positioned inside the magnetic field. The position and orientation of the sensor coils are then determined using the induced voltage. Due to the low field intensity of the magnetic fields, which can safely pass through human tissue, location measurement of the sensor is possible without restrictions imposed by line-of-sight requirements. EM tracking systems have the drawback of creating eddy currents in neighboring conductive materials. The secondary magnetic fields produced by these eddy currents alter the induced voltages detected by the sensors. Tracking errors are produced as a result of this change in the induced voltage [40].

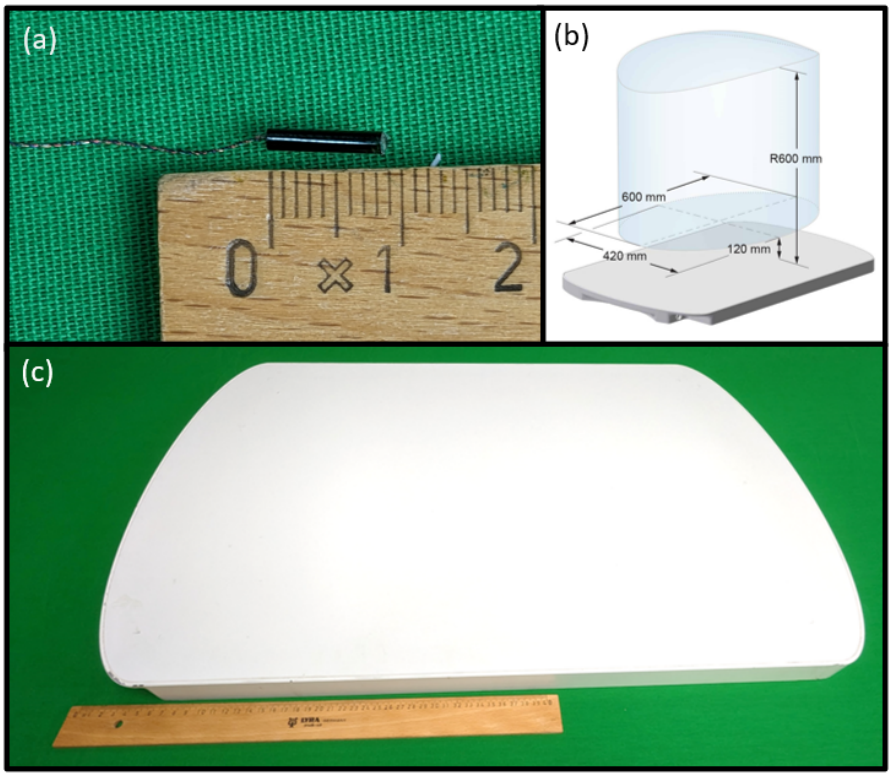

Figure 2.8: (a) A six Degrees of Freedom (DOF) EM sensor next to a caliper. (b) The working volume of the NDI Aurora tabletop field generator (Image courtesy of NDI (Northern Digital Inc.)). (c) Top view of the NDI Aurora tabletop field generator. The EM field generator has a thin barrier to minimize tracking distortions caused by ferromagnetic materials located below it, making it suitable for being placed on a patient table.

2.4 Rigid Point-Set Registration

A frequently occurring task in the development of IGT systems is the spatial registration of various systems for tracking or visualization (HMD glasses, tracking systems) and/or medical image data (CT, US, MRI) including the 3D models based on segmentations. Rigid point-set registration approaches are one way to solve these problems. These methods use landmarks or point clouds in the respective coordinate systems to find the corresponding spatial dependency. In the following, homogeneous transformations are introduced that provide a compact and easy tool for working with spatial transformations. Hereafter, the most common approaches for landmark-based and point-cloud-based registrations are explained.

2.4.1 Homogenous Transformations

Homogeneous transformations are a type of linear transformation commonly used in computer graphics and robotics to represent a combination of translations, rotations, and scalings in a unified mathematical framework. These matrices allow for a compact representation of multiple transformations and can be combined by matrix multiplication to form concatenated transformations. These transformations are widely used in robotics for the representation of the position and orientation of objects in space, as well as in computer graphics for modeling and animation.

Mathematically, let ${}^{\mathcal{A}}\mathbf{x}$ be a vector in a 3D Euclidean space $\mathcal{A}$ and let ${}^{\mathcal{A}}\mathbf{T}_{\mathcal{B}} \in \mathbb{R}^{4\times4}$ be a homogeneous transformation. Then, the transformed vector ${}^{\mathcal{B}}\mathbf{x}$ is given by:

$$
{}^{\mathcal{B}}\mathbf{x} = \begin{bmatrix} \mathbf{R} & \mathbf{t} \\ 0 & 1 \end{bmatrix} \begin{bmatrix} {}^{\mathcal{A}}\mathbf{x} \\ 1 \end{bmatrix} = {}^{\mathcal{B}}\mathbf{T}_{\mathcal{A}}\, {}^{\mathcal{A}}\mathbf{x} \tag{2.3}
$$

where $\mathbf{t} \in \mathbb{R}^3$ is the translational offset and $\mathbf{R} \in \mathbb{R}^{3\times3}$ is an orthogonal rotation matrix.

2.4.2 Landmark-Based Registration using Least-Squares Fitting and Single Value Decomposition

If the point-to-point correspondence is known and a rigid transformation can be assumed, then the method developed by Arun et al. [41] can be applied to find the homogeneous transformation ${}^{\mathcal{A}}\mathbf{T}_{\mathcal{B}}$ between two point sets of the same size ${}^{\mathcal{A}}P = \{{}^{\mathcal{A}}\mathbf{p}_i \in \mathbb{R}^3, 1 \leq i \leq N\}$ and ${}^{\mathcal{B}}P = \{{}^{\mathcal{B}}\mathbf{p}_i \in \mathbb{R}^3, 1 \leq i \leq N\}$.

The method tries to minimize the following cost function:

$$
\Sigma^2 = \sum_{i=1}^{N} \left\| {}^{\mathcal{B}}\mathbf{p}_i - (\mathbf{R}\,{}^{\mathcal{A}}\mathbf{p}_i + \mathbf{t}) \right\|^2 \tag{2.4}
$$

The algorithm employs a decoupled strategy. Let ${}^{\mathcal{B}}\mathbf{p}$ and ${}^{\mathcal{A}}\mathbf{p}$ be the centroids of the point sets, it first calculates $\mathbf{R}$, after which it determines $\mathbf{t}$ by $\mathbf{t} = {}^{\mathcal{B}}\mathbf{p} - (\mathbf{R}\,{}^{\mathcal{A}}\mathbf{p})$.

The fact that the centroid of $(\mathbf{R}\,{}^{\mathcal{A}}\mathbf{p}_i + \mathbf{t})$ and ${}^{\mathcal{B}}\mathbf{p}_i$ overlap allows us to apply this method. Thus, if we calculate ${}^{\mathcal{B}}\mathbf{p}'_i = {}^{\mathcal{B}}\mathbf{p}_i - {}^{\mathcal{B}}\mathbf{p}$ and ${}^{\mathcal{A}}\mathbf{p}'_i = {}^{\mathcal{A}}\mathbf{p}_i - {}^{\mathcal{A}}\mathbf{p}$, Eq. 2.4 can be reduced to:

$$\Sigma^2 = \sum_{i=1}^{N} \left\| {}^{\mathcal{B}}\mathbf{p}'_i - \mathbf{R}\,{}^{\mathcal{A}}\mathbf{p}'_i \right\|^2 \tag{2.5}$$

The actual algorithm consists of four steps, whereas one first calculates the previously mentioned centered point sets:

$${}^{\mathcal{B}}\mathbf{p}'_i = {}^{\mathcal{B}}\mathbf{p}_i - {}^{\mathcal{B}}\mathbf{p} \tag{2.6}$$

$${}^{\mathcal{A}}\mathbf{p}'_i = {}^{\mathcal{A}}\mathbf{p}_i - {}^{\mathcal{A}}\mathbf{p} \tag{2.7}$$

In the next step, the 3 × 3 matrix

$$\mathbf{H} = \sum_{i=1}^{N} {}^{\mathcal{B}}\mathbf{p}'_i \, {}^{\mathcal{A}}\mathbf{p}'^{T}_i \tag{2.8}$$

is calculated. In the third step, one needs to find the singular value decomposition (SVD) of $\mathbf{H}$

$$\mathbf{H} = \mathbf{U}\Lambda\mathbf{V}^T \tag{2.9}$$

which finally allows to calculate

$$\mathbf{R} = \mathbf{V}\mathbf{U}^T \tag{2.10}$$

2.4.3 Iterative Closest Point

In contrast to the previous approach, the Iterative Closest Point (ICP) algorithm [42] does not require knowledge of point-to-point correspondence. The likelihood of discovering the global optimum, however, is dependent on the properties of the point cloud, the number of points, and the initial spatial relationship between the two clouds.

Let ${}^{\mathcal{A}}P = \{{}^{\mathcal{A}}\mathbf{p}_i \in \mathbb{R}^3, 1 \leq i \leq M\}$ and ${}^{\mathcal{B}}P = \{{}^{\mathcal{B}}\mathbf{p}_j \in \mathbb{R}^3, 1 \leq j \leq N\}$ be two point sets that contain M and N points, respectively. The algorithm seeks to identify the rigid transformation ${}^{\mathcal{A}}\mathbf{T}_{\mathcal{B}}$ that minimizes the Euclidean distance between the supplied sets. The general steps of the algorithm are:

1. For each point in ${}^{\mathcal{A}}P$, calculate the minimum Euclidean distance with respect to ${}^{\mathcal{B}}P$ to find the nearest and therefore corresponding point:

$$d_m({}^{\mathcal{A}}\mathbf{p}_i, {}^{\mathcal{B}}P) = \min_{{}^{\mathcal{B}}\mathbf{p} \in {}^{\mathcal{B}}P} d({}^{\mathcal{A}}\mathbf{p}_i, {}^{\mathcal{B}}\mathbf{p}) \tag{2.11}$$

2. Using the least square technique for minimizing the distance as described in Section 2.4.2, determine the rotation matrix $\mathbf{R}$ and translation vector $\mathbf{t}$.
3. Compute the transformed point cloud of ${}^{\mathcal{B}}P$ using calculated values $\mathbf{R}$ and $\mathbf{t}$.
4. Calculate the error $E(\mathbf{R}, \mathbf{t})$ using the following equation and iterate until the required accuracy is reached. Corresponding points are defined by the minimum distance.

$$E(\mathbf{R}, \mathbf{t}) = \sum_{j=1}^{N} \sum_{i=1}^{M} \left\| {}^{\mathcal{A}}\mathbf{p}'_i - \mathbf{R}\,{}^{\mathcal{B}}\mathbf{p}'_j \right\|^2 \tag{2.12}$$

Even though, ICP tends to get stuck in a local optimum if a good initial relationship is not provided, it is still an often used point set registration technique because it is simple to comprehend and apply.

3 Facilitating Vascular Diagnostics

Contents

In this chapter, the two included sections present approaches to facilitate vascular diagnostics (Figure 3.1). First, a method is presented that enables probe pose tracking with minimal technical complexity for in-situ visualization of US images. Hereafter, this work presents a technique for automatic segmentation of arteries in US images.

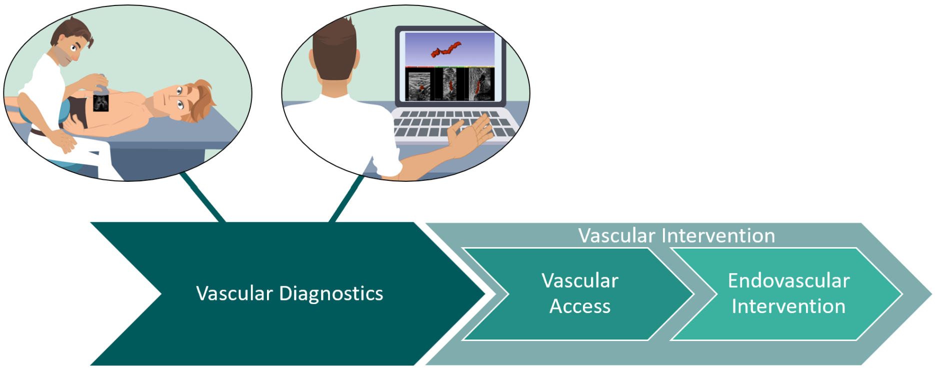

Figure 3.1: Workflow of vascular treatments with illustrations of futuristic systems to facilitate vascular diagnostics.

3.1 Augmented Reality In-Situ Visualization of Ultrasound Images

As elaborated in Chapter 1, the aim is to develop an AR system that can visualize US images in-situ with low technical complexity to provide a less laborious workflow during diagnostics. The question that arises with this specification is therefore:

RQ1 How can the probe be tracked with minimal technical complexity, and how accurate is the tracking?

To avoid a laborious setup, a method for tracking a rigid body based on retroreflective spheres by using the integrated depth camera of the AR glasses HoloLens 2 is described. Herewith, this work demonstrates the first inside-out six DOF tracking approach with HoloLens 2 for passive marker spheres that neither requires additional expensive tracking hardware nor illumination of the spheres. Additionally, the application is able to stream live images from a US station and display them in-situ – resulting in intuitive and realistic visualization. To provide other researchers in this field with an easy-to-set-up tracking approach, the algorithm is implemented with the Unity game engine (Unity Technologies, San Francisco, CA, USA). The code is available at `https://github.com/BIIG-UC3M/IGT-UltrARsound`. A further aim of this work was to provide thorough technical details of this approach, such as tracking accuracy in a static and dynamic setting, frequency and latency of displayed US images.

Parts of this section have been published in [43].

3.1.1 Related Work - Tracking With HoloLens and Ultrasound Image Streaming

The idea of using AR to support US examinations was already described in 1996 by Fuchs et al. [44], demonstrating its research interest. Due to their early stage of development, the AR glasses weighed nearly 3 kg, and the probe was spatially tracked using a mechanical arm. Thus, the whole setup was still far from being usable in daily practice. More than two decades later, the tetherless standalone HoloLens 2, with a weight of 566 g, improved image resolution and self-localization, hand gestures and voice commands for interactions, could bring the initial idea closer to the actual clinical application. In-situ visualization of US with AR is certainly possible with other sate-of-the-art visors [45], however, the following section concentrates on HoloLens as it provides the previously mentioned key features.

Tracking With HoloLens

Two approaches for instrument tracking with AR glasses exist. On the one hand, outside-in techniques utilize external sensors (e.g., optical or EM tracking) placed statically in the room to track the instrument as well as the HoloLens. On the other hand, inside-out techniques perform tracking via cameras and sensors integrated into the AR glasses – thus, neither additional hardware nor a cumbersome calibration would be necessary. Furthermore, incorporating an external tracking system leads to a more laborious system setup and workflow.

Outside-in Tracking

A clear advantage of outside-in techniques is the achievable accuracy and precision that certain medical interventions require. However, the use of an external tracking system in combination with HoloLens requires an often cumbersome registration to have a common coordinate system. In many cases, OTS facilitate tracking of medical instruments [38, 46–48]. In this scenario, line-of-sight between tracked tools (e.g., AR glasses and US probe) and OTS needs to be ensured at all times, which limits the possibilities of movement. EM tracking, on the other hand, does not have this disadvantage but suffers from interference with metallic parts. However, this modality is the only one that offers accurate tracking without line-of-sight in situations like AR-guided endovascular interventions [49, 50].

Inside-Out Tracking

The most common way of tracking surgical tools is to utilize the front-facing central camera for detecting AR markers [51–55]. A general drawback, nonetheless, is that the markers constantly need to point towards the front camera, limiting the movement and rotation of the tracked tool. Additionally, the tracking process heavily depends on light conditions. As an alternative, retroreflective spheres can be used for rigid body tracking with HoloLens. Kunz et al. [56] showed the feasibility of this approach with HoloLens 1 by either using the integrated depth camera or two of the four front facing cameras via triangulation. However, tracking with the front-facing cameras requires placing an IR light emitter on the HoloLens. Additionally, this work only evaluates relative translations (three DOF) of the spheres, thus, no conclusions can be drawn regarding the six DOF rigid body tracking. A recent proposal by Gsaxner et al. [57] showed promising results of rigid body tracking with retroreflective markers via triangulation, obtaining an accuracy of 1.70 mm / 1.11° with an extended Kalman filter. However, this approach again involves a supplementary light source on the HoloLens to illuminate the spheres, which might impair the mobility of the AR glasses. Considering the previous approaches and the requirements for the ideal system, the aim is to exploit the advantages of tracking retroreflective spheres with an inside-out approach, namely less light-dependency and no need for expensive external tracking systems, without the necessity of additional hardware to illuminate the spheres.

2D Ultrasound Visualization With Hololens

Only a few studies have investigated the combination of US imaging and HoloLens. Some of them rely on outside-in approaches to track the US probe and display the image [38, 47, 58]. Existing works utilizing inside-out approaches are, on the other hand, performed using an AR marker [49, 59, 60]. To acquire and stream images from the US station to HoloLens, one can either use a frame grabber at the display output of the US station or, if available, a software development kit providing access to the image data. Nguyen et al. [60] followed the latter approach and then downsampled the images to 100 × 100 pixels to send them as a single UDP package. However, this resizing comes with an image quality loss. On the other hand, Rüger et al. [38] and Kuzhagaliyev et al. [47] grabbed the screen output of the US stations and sent the trimmed images to HoloLens. Here again, depending on the image output, an image quality loss is possible. This loss of quality may become relevant when the US image in HoloLens is enlarged ex-situ to see finer structures. This work overcomes these disadvantages by streaming US images in original image quality with minimal latency and using a commonly used open-source network communication interface (OpenIGTLink).

3.1.2 Retroreflective Sphere and Rigid Body Tracking With HoloLens

The developed application runs directly on HoloLens 2 and was built with Unity 2019.4.22. The research mode was incorporated within Unity [61], allowing access to the depth camera, which operates in two modes for different distances – each one providing a depth image and an Active Brightness (AB) image [32]. On top of that, OpenCV was integrated within Unity for image processing tasks. As mentioned in Section 2.1.3, the depth camera offers two different modes, whereas in this work only the Articulated HAnd Tracking (AHAT) mode was used because it provides more frames per second and the maximum distance of 1 m is sufficient for tracking a hand-held US probe. The depth and AB image of the AHAT mode have a resolution of 512 × 512 pixels with 16 bits per pixel acquired at 45 frames per second. To track the pose of the rigid body composed of retroreflective spheres, the workflow described next consists of the following steps: (1) Measure the position of each sphere with respect to the world coordinate system using the depth camera. (2) Apply some filtering to reduce the noisy measurements of the depth camera. (3) Calculate the pose based on the resulting positions.

In order to compute ${}^{\mathcal{W}}\mathbf{s} = [x, y, z, 1]^{\mathrm{T}}$, which is the surface position of a retroreflective sphere with respect to a world coordinate system $\mathcal{W}$, the following equation is applied:

$$ {}^{\mathcal{W}}\mathbf{s} = {}^{\mathcal{W}}\mathbf{T}_{\mathcal{L}} \; {}^{\mathcal{L}}\mathbf{T}_{\mathcal{D}} \; {}^{\mathcal{D}}\mathbf{s} \tag{3.1} $$

where ${}^{\mathcal{W}}\mathbf{T}_{\mathcal{L}} \in \mathbb{R}^{4\times4}$ is the pose of the left-front camera of HoloLens 2 (Figure 3.2) with respect to the world coordinate system, ${}^{\mathcal{L}}\mathbf{T}_{\mathcal{D}}$ is the extrinsic camera matrix of the depth camera, which can be accessed via the research mode and ${}^{\mathcal{D}}\mathbf{s}$ is the surface position of a sphere with respect to the depth camera coordinate system. ${}^{\mathcal{W}}\mathbf{T}_{\mathcal{L}}$ is provided by the research mode for each frame, while the origin of the world coordinate system is placed at the device's pose at application start. To track the retroreflective spheres and thereby the marker in the camera space, one first needs to detect the spheres in the AB image of the AHAT mode, which then allows finding the corresponding points in the depth image of the AHAT mode.

A blob detection algorithm provided by OpenCV is utilized to detect the spheres in the AB image (Figure 3.3(a)). For each of the $i = 1 \ldots 4$ spheres in the image, the method returns the pixel coordinates $\mathbf{p}_i$ corresponding to the center of the circular image of the sphere. Then, the corresponding pixel value $d_{\mathbf{p}}$ in the depth image (Figure 3.3(b)) is multiplied by the appropriate vector from a static lookup table $\mathbf{L} \in \mathbb{R}^{512\times512\times3}$ (also accessible via the research mode) to compute the initial guess of the surface sphere position ${}^{\mathcal{D}}\mathbf{s} = [x, y, z, 1]^T$ in the depth camera coordinate system:

$$ {}^{\mathcal{D}}\mathbf{s} = \begin{bmatrix} x \\ y \\ z \\ 1 \end{bmatrix} = d_{\mathbf{p}} \begin{bmatrix} \mathbf{L}(\mathbf{p}) \\ 1 \end{bmatrix} = d_{\mathbf{p}} \begin{bmatrix} u \\ v \\ w \\ 1 \end{bmatrix} \tag{3.2} $$

where $[u, v, w]^{\mathrm{T}}$ is the entry of the lookup table corresponding to the image position $\mathbf{p}$.

As this approach does not directly allow tracking the center position of the spheres, but just a point on the surface, a correction vector is added to the surface position

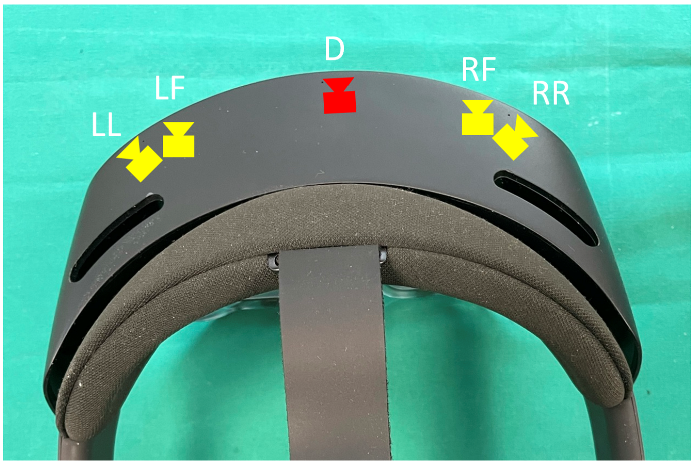

Figure 3.2: Top view of HoloLens 2, the different visible light cameras (yellow), and the depth camera (red). The research mode provides for each acquired frame the pose of the left-front (LF) visible light camera. The extrinsic transform from the left-front camera to the depth camera can also be accessed via the research mode.

${}^{\mathcal{W}}\mathbf{s}$. This vector's direction and length can be computed by subtracting the position of the measured surface point ${}^{\mathcal{W}}\mathbf{s}$ and the depth camera ${}^{\mathcal{W}}\mathbf{c}_d$ with a length equal to the sphere radius r_s (NDI passive sphere, $r_s = 5.9\,\text{mm}$). Thus, the final center sphere position $\mathbf{s}_c$ is calculated as:

$$
{}^{\mathcal{W}}\mathbf{s}_c = {}^{\mathcal{W}}\mathbf{s} + \frac{{}^{\mathcal{W}}\mathbf{s} - {}^{\mathcal{W}}\mathbf{c}_d}{\|{}^{\mathcal{W}}\mathbf{s} - {}^{\mathcal{W}}\mathbf{c}_d\|} r_s \tag{3.3}
$$

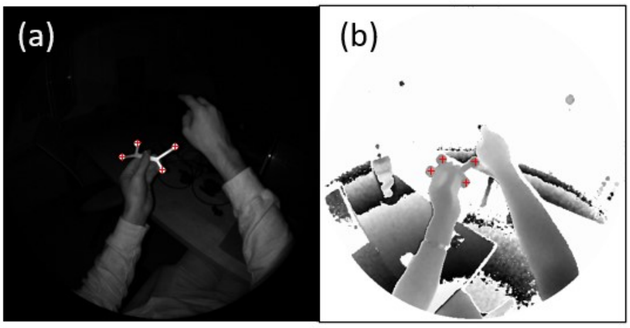

Figure 3.3: (a) The AB image with the detected centers of the spheres (red). (b) The corresponding depth image. The corresponding pixel values are used to calculate the position of the spheres using a lookup table.

Position Estimation Using a Kalman Filter

A Kalman filter [62] is a mathematical method for the iterative estimation of parameters describing system states on the basis of potentially erroneous observations. As the measurements of the depth camera of HoloLens 2, which is hardware-wise the same as the Azure Kinect camera, show a noisy behavior [63], a Kalman filter is implemented to reduce the influence of erroneous measurements. To this end, a 3D constant acceleration model served as the underlying motion model for each measured sphere position. The optimal values of the process noise covariance σ_Q and measurement noise covariance σ_R are determined through testing on a prerecorded sequence, obtaining $\sigma_Q = 0.0001$ and $\sigma_R = 0.001$ for the static setting. In a dynamic environment, the optimal values were $\sigma_Q = 0.0001$ and $\sigma_R = 0.0001$.

Marker Pose Calculation

The four sphere center positions ${}^{\mathcal{W}}\mathbf{s}_{c,i}$ in the world coordinate system can be used to calculate the pose ${}^{\mathcal{W}}\mathbf{T}_{\mathcal{M}}$. Therefore, to avoid an ambiguous identification of the order, the relative distances between the spheres need to be unique. The 3D coordinates of the sphere centers are expressed in a common reference frame whose origin can be placed at a desired position and orientation. In this work, an OTS, more precisely Polaris Spectra from NDI, was used to measure the distances and create the origin of the reference frame, including the positions ${}^{\mathcal{RF}}\mathbf{s}_{c,i}$ of the sphere centers. The tool definition was performed beforehand and provided to the tracking algorithm. Within the tracking algorithm and for each cycle, first the distances of the spheres to each other are calculated to identify corresponding points. Hereafter, a landmark-based registration [41] using ${}^{\mathcal{RF}}\mathbf{s}_{c,i}$ and ${}^{\mathcal{W}}\mathbf{s}_{c,i}$ is performed to compute ${}^{\mathcal{W}}\mathbf{T}_{\mathcal{M}}$.

3.1.3 Ultrasound Image Streaming

For US acquisitions, the portable system MicrUs from TELEMED (Vilnius, Lithuania) in combination with the linear US probe L12-5L40S-3 is utilized. This system offers access to the US images without requiring a frame grabber. Hereafter, the network communication interface and the registration approach required to find the spatial transformation from the tracked marker to the origin of the image is described.

The US images were sent via the open-source-toolkit PLUS [64] from the computer to the Unity application running on HoloLens 2. As no library exists in Unity supporting the OpenIGTLink protocol [65] used by PLUS, a custom-made client side is implemented. In order to display the US images in-situ on the AR glasses, it is necessary to find the spatial transformation from the tracked marker to the origin of the image ${}^{\mathcal{M}}\mathbf{T}_{\mathcal{US}}$. To this end, a phantom-free approach [66] that requires an external OTS is performed. This approach was chosen because it shows better results than the commonly used N-wire phantom [67]. For the calibration, the static pose of the optically tracked US probe marker ${}^{\mathcal{OT}}\mathbf{T}_{\mathcal{M}}$ immersed in saltwater is recorded. Using a tracked and pivot-calibrated stylus, eight stylus tip positions in the US beam were measured (Figure 3.4). To ensure that the tip and not the body were visible in the image, the stylus was slowly pulled out of the US beam and the image that last showed a bright spot was used. Identifying the positions of the stylus tip in the eight US images and simultaneously in the OTS space allows for the calculation of the transformation of the US image in the OTS coordinate space ${}^{\mathcal{OT}}\mathbf{T}_{\mathcal{US}}$ by means of a landmark-based registration [41]. Finally, one can compute the desired transformation by closing the transformation loop with:

$$ {}^{\mathcal{M}}\mathbf{T}_{\mathcal{US}} = {}^{\mathcal{M}}\mathbf{T}_{\mathcal{OT}} \; {}^{\mathcal{OT}}\mathbf{T}_{\mathcal{US}} \tag{3.4} $$

The 3D models for the attachment of the markers used in this work were retrieved from PLUS [68].

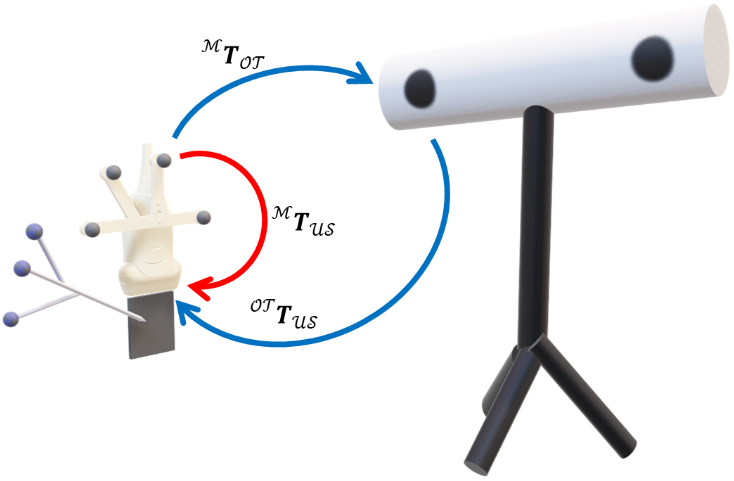

Figure 3.4: Transformations (arrows) available and calculated for the spatial calibration between the US marker and the US image. The measured positions of the stylus tip in the US images and tracking space allow the calculation of ${}^{\mathcal{OT}}\mathbf{T}_{\mathcal{US}}$ and thereafter close the loop to compute ${}^{\mathcal{M}}\mathbf{T}_{\mathcal{US}}$ (red arrow).

3.1.4 Evaluating Tracking Accuracy and Latency

Apart from testing the feasibility, the aim was to perform a technical evaluation of the proposed approach. To this end, the tracking accuracy of the sphere's positions and the pose estimation in a static scenario were measured. To further evaluate the system in a realistic environment, the pose tracking accuracy was evaluated in a dynamic scenario. Additionally, the time duration of one tracking cycle and the latency of the displayed US images on HoloLens 2 were measured.

Retroreflective Sphere Tracking

To quantify the accuracy of the tracking method in a static scenario, relative movements of the marker with the AR glasses and, as a ground truth, the highly accurate OTS were measured (Figure 3.5). 20 different poses of the marker in a range of approximately 0.3 to 1 m were recorded, acquiring 30 samples for each pose. Thereafter, for each sample and each pose, the relative distance of each sphere to the corresponding sphere in the first pose was computed and compared to the value obtained with OTS. For example, to calculate the distance error d_e between the second and first pose for one sphere, one computes:

$$d_e = \left\|{}^{\mathcal{W}}\mathbf{s}_{c,p_2} - {}^{\mathcal{W}}\mathbf{s}_{c,p_1}\right\| - \left\|{}^{\mathcal{OT}}\mathbf{s}_{c,p_2} - {}^{\mathcal{OT}}\mathbf{s}_{c,p_1}\right\| \tag{3.5}$$

where ${}^{\mathcal{OT}}\mathbf{s}_{c,p_1}$ is a sphere center position for the first pose in the OTS coordinate system.

To additionally evaluate the actual marker pose tracking accuracy, the pose change of each marker, which is based on the four sphere positions, was also analyzed. Here, the relative translational and rotational movements between poses measured with HoloLens 2 and the OTS were compared. Again, for example, to measure the translation error $\mathbf{t}_e$ and rotational error $\mathbf{r}_e$ between the second and first pose, one first measures the pose error $\mathbf{T}_e$:

$$\mathbf{T}_e = \left(\left({}^{\mathcal{W}}\mathbf{T}_{\mathcal{M},p_1}\right)^{-1} {}^{\mathcal{W}}\mathbf{T}_{\mathcal{M},p_2}\right)^{-1} \left(\left({}^{\mathcal{OT}}\mathbf{T}_{\mathcal{M},p_1}\right)^{-1} {}^{\mathcal{OT}}\mathbf{T}_{\mathcal{M},p_2}\right) \tag{3.6}$$

which can be used to extract $\mathbf{t}_e$ and $\mathbf{r}_e$ in Euler angles. Note that here $\mathbf{T}_e = {}^{\mathcal{M},p_2}\mathbf{T}_{\mathcal{M},p_2}$ and that one could also use $\mathbf{T}_e = {}^{\mathcal{M},p_1}\mathbf{T}_{\mathcal{M},p_1}$. Both poses are valid options.

Figure 3.5: Setup for the static tracking accuracy evaluation. HoloLens 2 and the OTS are fixed, while the US probe with its marker is moved to 20 different poses for measurement acquisition.

For the dynamic scenario, on the other hand, a trajectory of the marker with the statically placed AR glasses and the OTS was acquired (trajectory illustrated in Figure 3.6). As line-of-sight of the spheres is necessary, the possible rotation around the x- and y-axes is limited. For the temporal calibration between the measured trajectories of HoloLens 2 and the tracking system, a sinusoidal trajectory before the actual acquisition was measured. Thereafter, the sinusoidal signals were downsampled to have matching frequencies. Finally, the maximum position of the cross-correlation of both signals allows one to calculate the time shift between both measurements. As in the static scenario, one computes $\mathbf{t}_e$ and $\mathbf{r}_e$ with the initial pose as the reference. To measure the tracking frequency, the time interval of 500 tracking cycles was obtained.

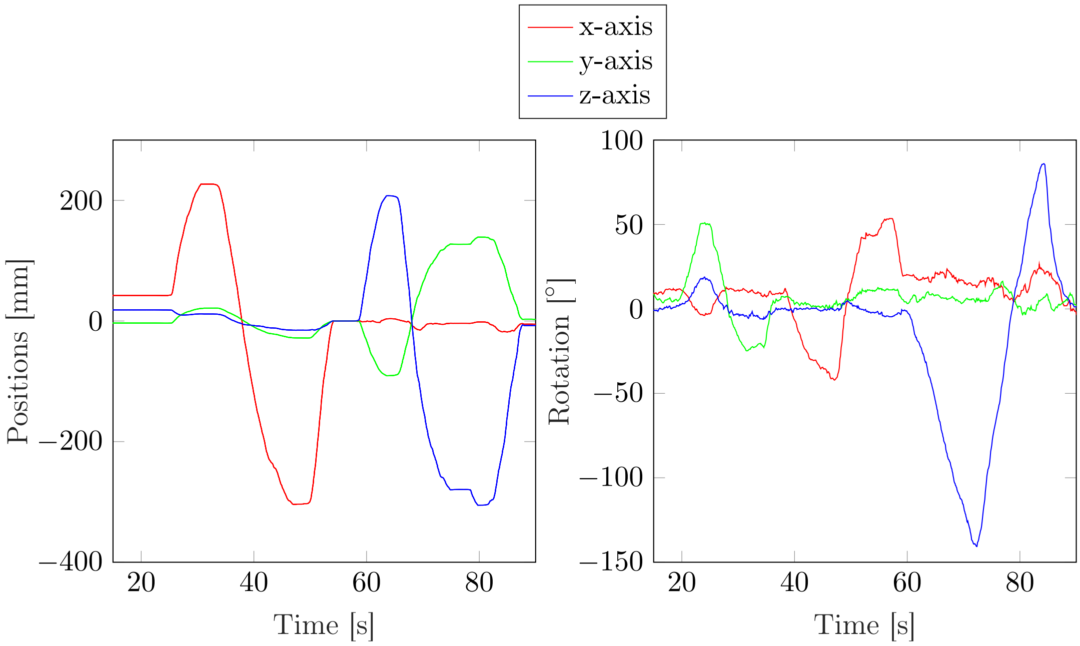

(a) (b)

Figure 3.6: The trajectories obtained with the OTS for the dynamic analysis. (a) Relative positions and (b) relative rotations for each axis with respect to the initial pose.

Ultrasound Image Streaming

Apart from the correct in-situ placement of the US image, it is essential that the latency of displayed US images on HoloLens 2 is low enough for real-time perception. To measure the latency, a slow motion video is recorded at 120 Hz which results in a temporal resolution of 8 ms. The video is recorded through the lenses of the AR glasses such that the virtual canvas, including the US image and the US image on the real screen are visible. To measure the delay, the depth of the US image is changed, and the frames are counted from the change on the real US station screen until the change becomes visible on the virtual canvas. For the evaluation, the latency was measured 30 times. Images with a matrix size of 512 × 512 pixels and 8 bits per pixel were sent. Note that the image matrix size does not change even if the depth is modified.

3.1.5 Tracking Accuracy and Latencies

Following, the evaluation results of the tracking accuracy, tracking frequency and the US streaming latency are described. Within the tracking accuracy evaluation, the results of the static and dynamic scenario are first presented separately and then compared.

Retroreflective Sphere Tracking Accuracy

The accuracy of the sphere position tracking with and without the implemented Kalman filter is compared hereafter. The mean distance error and standard deviation without filter was $d_{e,RMS} = 3.27 \pm 1.90\,\text{mm}$. On the other hand, the Kalman filter lowered the distance error to $d_{e,RMS} = 2.23 \pm 1.38\,\text{mm}$ (Figure 3.7(b)). As shown in Figure 3.7(a), the error depends on the distance to the depth camera and increases roughly by 1.5 mm between 0.3 and 1 m. For all distances except one, the standard deviation decreases once the filter is applied.

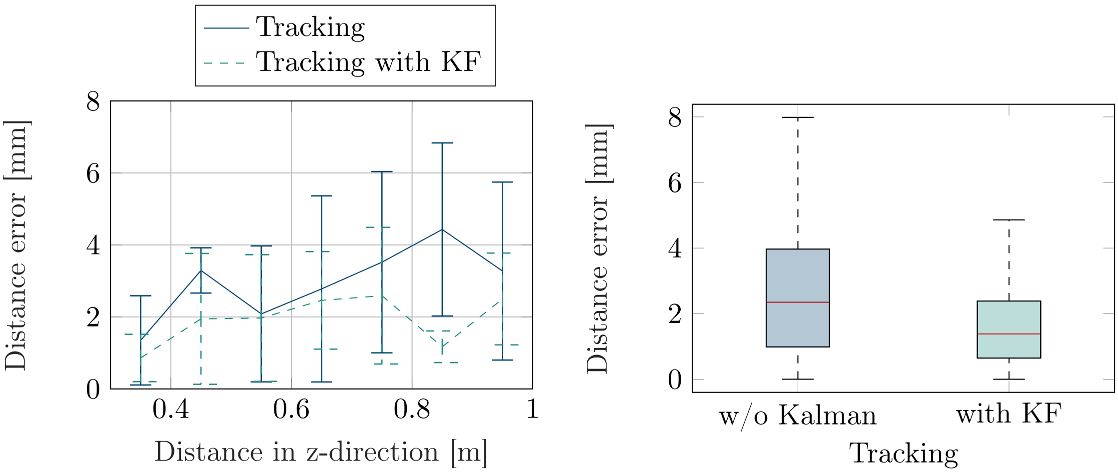

(a) (b)

Figure 3.7: Results of the accuracy evaluation for position tracking with HoloLens 2. (a) Mean and standard deviation of $d_{e,RMS}$ versus the distance to the depth camera. (b) Distribution (median, 25th and 75th percentile, minimal and maximal errors) of $d_{e,RMS}$ for tracking with and without Kalman filter.

In a second step, the accuracy of the pose tracking with and without Kalman filter for a static scenario is compared. Again, only the relative movements to the first obtained pose are evaluated. In Figure 3.8, $\mathbf{t}_{e,RMS}$ and $\mathbf{r}_{e,RMS}$ are visualized for each axis. When looking at $\mathbf{t}_{e,RMS}$, it is visible that applying a Kalman filter lowers the median error for each axis. Except for the x-axis, the 75th percentile and the maximum error are lower when using a Kalman filter. For the rotational error $\mathbf{r}_{e,RMS}$, only a slight improvement can be achieved with the filter. In all cases, the median is close to or lower than 1°.

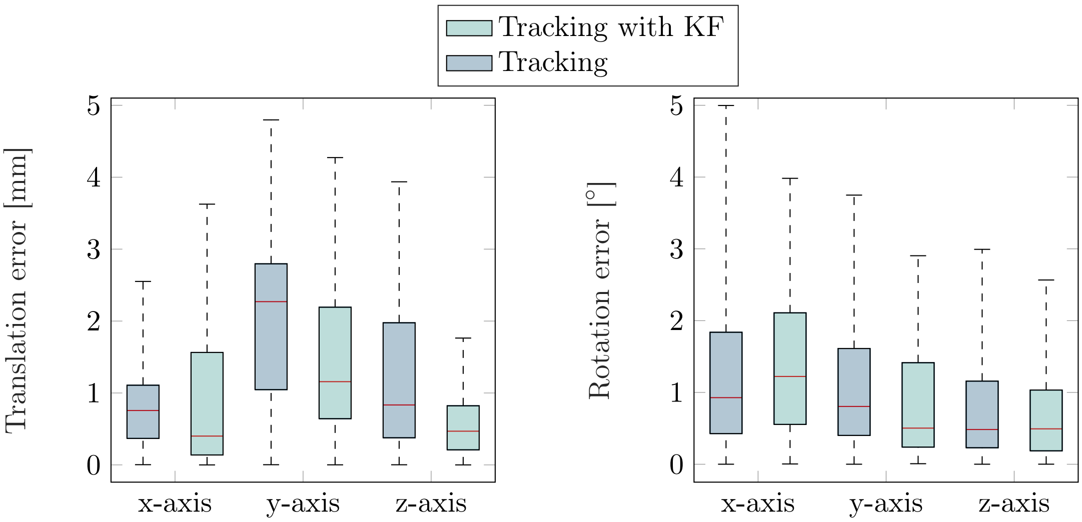

(a)

(b)

Figure 3.8: Results of the accuracy evaluation for pose tracking with HoloLens 2 in a static scenario. (a) The distribution of the translational error and (b) the distribution of the rotational error with and without Kalman filter.

In a third step, the accuracy of the pose tracking in a dynamic scenario is compared. Figure 3.9 shows the distribution of $\mathbf{t}_{e,RMS}$ and $\mathbf{r}_{e,RMS}$ for each axis. One can clearly see that in a dynamic scenario, errors higher than roughly 3 mm for one fourth of the measurements with maximum errors of around 15 mm are obtained. On the other side, the median values are below 2 mm. The Kalman filter is able to lower the higher errors to a maximum value of 10 mm while the median values are similar in both cases. Overall, we see a similar behavior for the rotational error $\mathbf{r}_{e,RMS}$, namely partially higher errors with low median errors. In this case, however, the Kalman filter brings only a slight improvement regarding the accuracy.

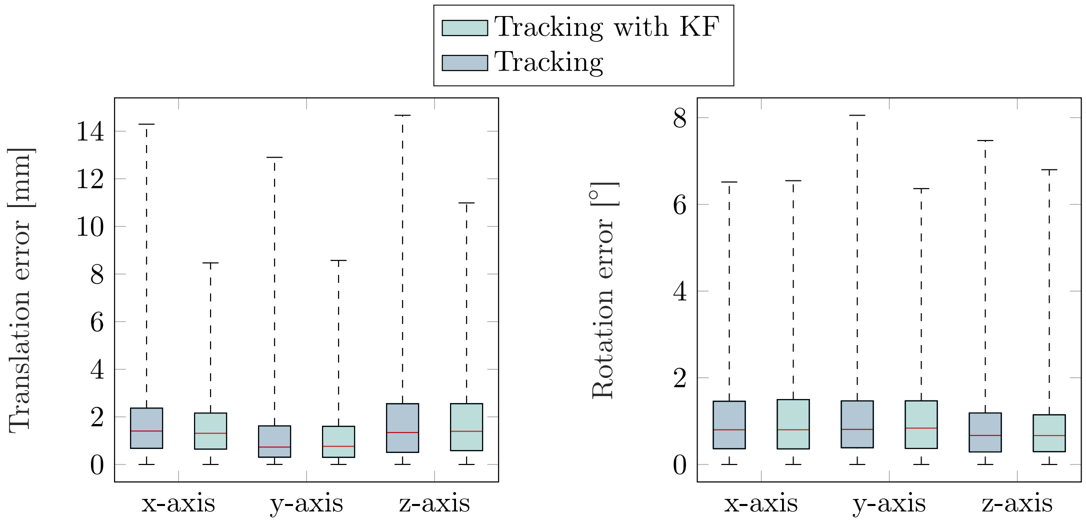

(a)

(b)

Figure 3.9: Results of the accuracy evaluation for pose tracking with HoloLens 2 in a dynamic scenario. (a) The distribution of the translational error with and without Kalman filter. (b) The distribution of the rotational error for each axis with and without Kalman filter.

Tab. 3.1 shows the statistics of the errors obtained in both scenarios for a comparative analysis. Note that, to this end, the magnitudes of $\mathbf{t}_e$ and $\mathbf{r}_e$ are computed, which is a valid option in this case [69]. When looking at $\|\mathbf{t}_e\|$, one can see that the median only slightly increases without any filter. The RMS value decreases by roughly 1 mm when applying the filter in both scenarios. For $\|\mathbf{r}_e\|$, the median as well as the RMS values remain similar for all cases. To summarize, the Kalman filter improves the accuracy of the translation measurements while not having a noticeable effect on the rotational values.

Table 3.1: Error statistics of $\|\mathbf{t}_e\|$ and $\|\mathbf{r}_e\|$ for dynamic and static scenarios with and without Kalman filter.

		Min	**25th p**	**Median**	**75th p**	**Max**	**RMS**
		Translation error [mm]					
Static	Tracking only	0.03	1.73	2.71	3.50	5.93	3.07
	With Kalman filter	0.02	1.24	1.98	2.58	4.70	2.14
Dynamic	Tracking only	0.15	2.02	3.01	4.42	17.58	4.79
	With Kalman filter	0.08	1.96	2.81	3.79	16.15	3.76
		Rotation error [°]					
Static	Tracking only	0.10	1.21	2.01	2.74	4.32	2.24
	With Kalman filter	0.01	1.11	1.81	2.67	4.11	2.16
Dynamic	Tracking only	0.19	1.17	1.75	2.49	8.51	2.25
	With Kalman filter	0.23	1.18	1.70	2.46	10.07	2.19

Finally, the average time and standard deviation for one tracking cycle were 50.64 ± 7.11 ms resulting in a frequency of around 20 Hz.

Ultrasound Image Streaming Latency

83 % of the frames had a delay of 2 or fewer frames and thus a maximum delay of 16 ms (Figure 3.11). Figure 3.10 shows the application running on HoloLens 2. The US image of a breast phantom is visible on the computer screen, while the user can see the image in-situ through the AR glasses. Although only shown with a breast phantom, the application can be used for vascular diagnostics without further adaptions.

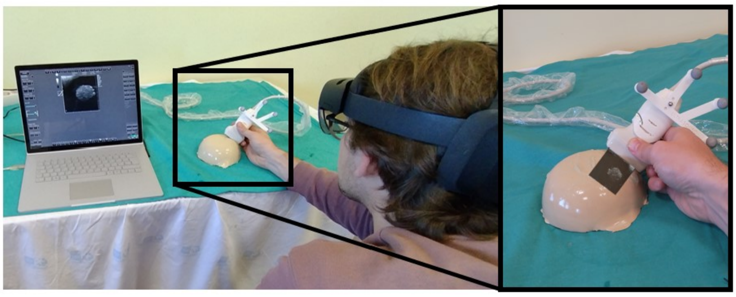

Figure 3.10: The HoloLens 2 user holding the US probe with the attached retroreflective spheres during a breast phantom acquisition, showing the US image on the computer screen (left). The view through the AR glasses enables to see the image in-situ (right). Even

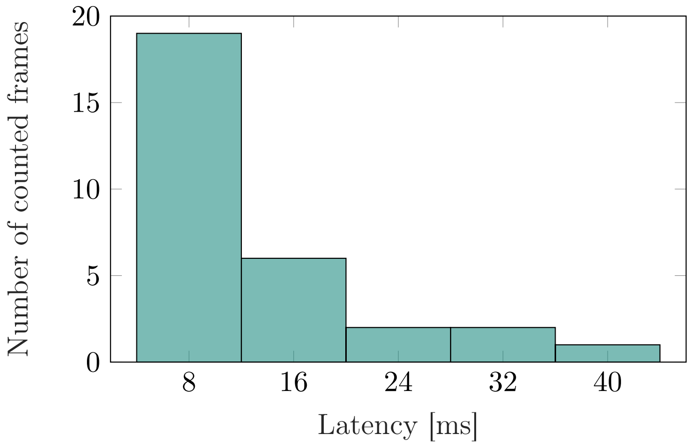

Figure 3.11: Results of the latency measurement of displayed US images on HoloLens. A careful examination of the slow-motion video with 120 Hz allows to count the frames until a change in the US image is visible on HoloLens 2.

3.1.6 Discussion

US requires skilled and experienced sonographers for correct and accurate vascular diagnostics. This is partially explained by the mental workload of aligning small cross-sectional 2D images in the 3D anatomy of the patient. This AR application overcomes this disadvantage by displaying live US images in-situ using the AR glasses HoloLens 2. In this section, an approach to track the US probe with retroreflective spheres with an inside-out technique is described, utilizing solely the depth camera of HoloLens 2. Accordingly, no expensive additional hardware is necessary, and no high technical effort is necessary to use the system. Further, it is shown how to stream US images from a US station with minimal latency. For a final evaluation, a technical characterization of the application by measuring spatial tracking accuracy and latency of displayed US images is performed.

The accuracy is measured by comparing relative movements obtained with HoloLens 2 and a high accuracy OTS. The results show that position tracking accuracy improves when applying a Kalman filter. Not only does the median of $d_{e,RMS}$ decrease, but so do the 75th percentile and maximum values. Consequently, a decrease is visible in $\mathbf{t}_{e,RMS}$ for each axis. The rotation error, otherwise, remains similar. A possible explanation is that if the same incorrect position shift is measured for each sphere, the translation error increases while the rotation error stays the same. Indeed, the measured errors align with previously published works on the accuracy of the depth camera [63], in which errors between 1.5 and 2.5 mm are stated for distances of 0.5 to 1 m in the binned wide mode. A study published by Microsoft [70] states slightly lower values (1-2 mm). However, they do not differentiate between different modes, which makes a comparison difficult. To conclude, it is assumed that a majority of the measured error in a static setting is due to hardware limitations. Nevertheless, the following software-related steps could improve the results. It is assumed that the static lookup table **L** used to calculate the positions is perfect. A re-calibration might lower $d_{e,RMS}$ and therefore $\mathbf{T}_e$. Additionally, this approach assumes that the measurement vector of the Kalman filter consists of the calculated positions in all three dimensions. Another option that could potentially further improve the results, is to use the measured blob location **p** in the AB image as measurement vector instead. However, to calculate the predicted measurement from the state prediction, one would need to know the inverse version **L** which is not available. Therefore, this work relies on a simplified model for the Kalman filter.

Regarding the dynamic measurements, it is to be expected that the errors increase. However, it is striking that a quarter of the measurements (Figure 3.9) range from 4 to 15 mm. In this case, as no literature exists that investigates the accuracy of the depth camera in a dynamic scenario, it is difficult to determine if the error is hardware- or software-related. Applying a Kalman filter improves the accuracy regarding the translation measurements in both settings. To obtain the best results, it was necessary to apply different values of the noise covariance and measurement noise covariance for the static and dynamic scenarios, respectively.

Gsaxner et al. [57] showed slightly lower errors for translation and rotation with 1.70 mm and 1.11° in a static setup. In a dynamic setting, their approach outperforms this one with 1.90 mm and 1.18°. However, the presented approach does not need an additional light source to illuminate the retroreflective spheres. Additionally, Gsaxner et al. [57] compared absolute positions and rotations of HoloLens 2 and an OTS in the same coordinate system, which was achieved by means of a hand-eye calibration. Thus, a direct comparison between the two approaches is challenging. For this system, it was decided to compare only the relative movements of the marker, as it is not clear how much the hand-eye-calibration influences the measured error.

With the current arrangement of the spheres, it is inevitable that there will be some blind spots where the rigid body cannot be tracked. For the proposed application, it is assumed that the possible rotations are sufficient, as the sonographer will not look at the US image turned by 90° so that only the edge of the image is visible. It is possible to add more spheres to the rigid body, which would allow it to track the body with less or even no movement constraints. However, this would impair the handiness and maneuverability of the US probe with the attached rigid body. As a result, this system uses the rigid body that the PLUS library offers while sacrificing some movement freedom.

Overall, the tracking accuracy reported here is promising for vascular diseases in US diagnostics, in which a sub-millimeter accurate overlay of real and imaged anatomy is not required. It is worth mentioning that the accuracy might be lower in a real-life scenario in which HoloLens also moves. In this work, the AR glasses are placed statically throughout the measurements. Thus, the error of the self-localization of HoloLens is not taken into account. A previous study showed that the error of self-localization may be up to 2 cm in a room-scale environment [71]. Consequently, the accuracy of this approach may be greatly influenced by a movement of the HoloLens. A combined error of about 2.5 cm could still be acceptable for US diagnostics, where the main goal is to find the target anatomy and improve ergonomics. For the subsequent stitching of the 2D images into a tUS, it is crucial whether the error is systematic or random. A systematic error would result in the 2D images still being correctly positioned relative to each other, which would still be acceptable. In [71], it seems that self-localization error follows a systematic behavior.

Using the proposed approach, a tracking frequency of 20 Hz was achieved. The tracking frequency should ideally be ≥ 60 Hz to match the frame rate of HoloLens 2 and provide smooth visualization. Therefore, future work could consist of an analysis of the algorithm to identify the most time consuming parts. An initial improvement might be achieved by performing the blob detection only in a region of interest defined by the previous locations of the blobs.

Low latencies are crucial for in-situ visualization of US images - especially when guiding interventions such as biopsies. For this system, the latency of displayed US images was sufficiently low for real-time perception, with a majority of frames being $<$ 16 ms delayed, proving that this approach is faster than the 80 ms reported by Ngyuen et al. [60]. García-Vázquez et al. [49] stated a latency of 259 ms for US volumes; correspondingly, a significantly higher amount of data was transmitted, which makes a comparison difficult. Other studies mentioned in Section 3.1.1 did not measure any latencies. The development of the client-side based on the OpenIGTLink protocol additionally allows connecting any other US station that supports streaming via the PLUS toolkit. Nevertheless, the US calibration needs to be performed for each new US probe.

3.1.7 Section Summary

The goal of this study was to provide a HoloLens 2 application for in-situ visualization of live US images. To answer **RQ1**, an application was developed that enables inside-out tracking for commonly used retroreflective spheres, and the tracking accuracy was evaluated in a static and dynamic setting.

The inside-out tracking is performed through the depth camera of HoloLens 2. Accordingly, neither an external tracking system nor illumination of the spheres with additional hardware is required and, thus, it provides a cost and space efficient alternative to other approaches. The achieved accuracy is promising for diagnostic US examinations and partially for image-guided therapies, in which no sub-millimeter accuracy is necessary.

In the context of facilitated vascular diagnostics, this work presents an important step towards ergonomic and intuitive image acquisition. Furthermore, the simultaneous recording of the image and its pose in space offers the option to create a tUS after a sweep along the artery. This, however, requires that the self-localization error follows a systematic pattern such that images are stitched with a common offset. For post-acquisition pathology evaluation, the tUS and an automatic segmentation of arteries play important roles and are addressed in the next section.

3.2 Automatic Segmentation of Arteries in Ultrasound Images

In the previous section, US images were displayed in-situ with minimal technical effort to facilitate image acquisition. This implicitly means that for each acquired image, both position and orientation are known in a common coordinate system. Looking again at the workflow and the ideal system in Figure 3.12, the next step is the visualization of a tUS image, including orthogonal planes. This visualization and the automatic segmentation of arteries in the images may further facilitate the diagnostic process by providing the physician with a 'roadmap'.

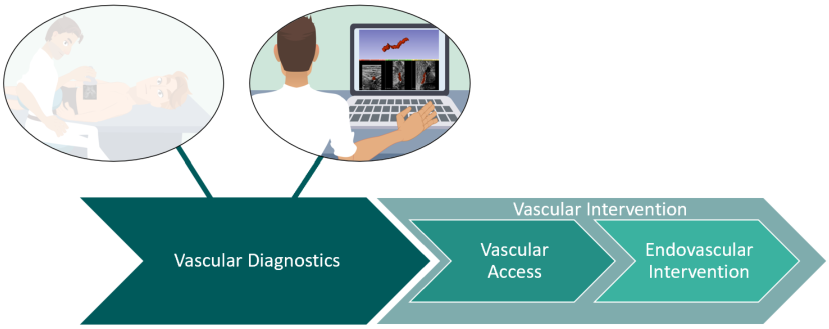

Figure 3.12: Workflow of vascular treatments with a highlighted illustration of the futuristic systems to facilitate vascular diagnostics after acquisition.

3D Slicer [73] in combination with PLUS [64] already offers algorithms and features to stack up 2D images to a volumetric image if positions and orientations are known. The combination allows for temporal and spatial calibrations between the transducer and tracking system. This framework incorporates functions for data gathering from US systems and positioning devices, as well as volume reconstruction from US pictures (Figure 3.13), among others, and offers a user-friendly interface for performing each stage of calibration.

Therefore, the only remaining technical hurdle in the development of the system is the reliable automatic segmentation of the arteries. As US is characterized by a high amount of noise and a low signal-to-noise ratio, standard image processing processes may not be adequate for successful segmentation. Therefore, the following research question was raised:

RQ2 How can arteries be reliably segmented in US images, and what accuracy is achievable?

Parts of this section have been published in [72].

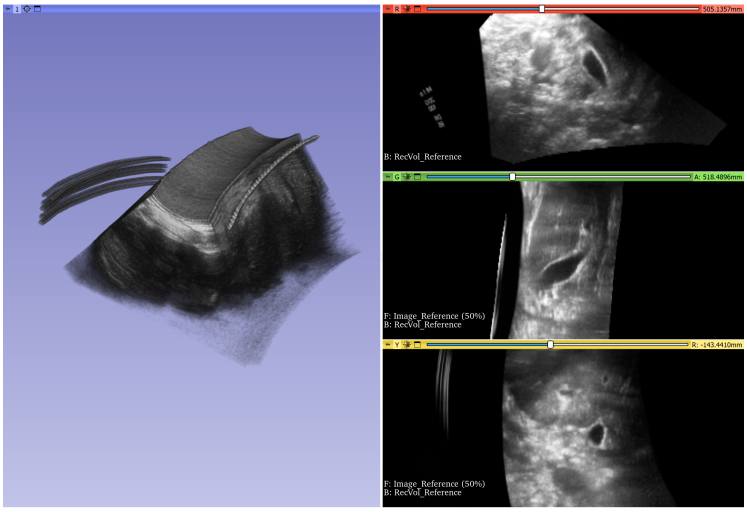

Figure 3.13: View of a tUS in 3D Slicer reconstructed from single 2D US images. On the left, the volume is rendered and on the right, three cross-sectional images from the tomogram in the main sectional planes (axial, sagittal, coronal) are shown. The imaged anatomy comprises the liver and the aorta. Image used with permission from Sven Böttger (Institute for Robotics and Cognitive Systems, University of Lübeck).

In recent years, the gold standard in research for medical image segmentation relies on deep learning based approaches, especially the U-Net architecture [74]. With 2D US images of the femoral artery acquired consecutively over time using a handheld US probe, a stacked volume can be created. In this section, an attempt is presented to leverage this sequential fashion as prior spatial information by using the segmentation results of the previous slice as additional input to different variations of an U-Net while iterating through the stacked volume. Even though these attempts are only carried out for femoral arteries, which is interesting for PAD interventions, one can assume that the approach would also work for AAA [75] and consequently for an EVAR procedure.

3.2.1 Related Work - Automatic Segmentation of Vessels in Ultrasound

In past years, deep Convolutional Neural Networks (CNN) have achieved outstanding results in image classification, segmentation, and object recognition, even on US images that are typically difficult to analyze. CNNs have also been used to identify blood vessels within US pictures. Smistad et al. [76] classified image regions of vessel-like features using a classification network for images. In 2018, Smistad et al. [77] employed a CNN of the U-net type to segment distinct nerves and blood vessels from US augmentations to increase accuracy. Groves et al. [78] used a Region Based Convolutional Neural Networks (R-CNN) to automatically segment the carotid artery and internal jugular vein from transverse neck US. Using the Mask R-CNN, a 3D reconstructed vasculature structure with the same precision as a manually segmented CT image was created. This implementation therefore provides analysis of the neck vasculature and facilitates 3D reconstruction of the vessels.

3.2.2 Data Acquisition

Data acquisition was performed by an experienced vascular surgeon with US expertise with a 2D linear US probe (L12-3, Philips Medical Systems International B.V., Best, The Netherlands) along with a US station (EPIQ7, Philips Medical Systems International B.V., Best, The Netherlands) and images were transferred to a computer using a network protocol provided by the manufacturer. The complete data set consisted of US images along the femoral artery from five healthy volunteers between the ages of 27 and 31. The scan for each one of the subjects started below the inguinal ligament, following a superior-to-inferior movement and ending at the adductor hiatus. This protocol was repeated three times for each subject, resulting in a total of 10,557 2D US images (Table 3.2) with a size of 512 × 323 pixels and an intensity range of [0, 255]. Binary ground truth masks consisting of two classes, the background and the femoral artery [0, 1], were manually segmented with the guidance of an experienced sonographer. Once every image had its corresponding mask, training, validation and testing data sets were defined, with an approximate split of 60 %, 20 % and 20 %, respectively.

Table 3.2: Summary of images per subject.

	Run 1	Run 2	Run 3	Total
Subject 1	733	767	669	2,169
Subject 2	1098	938	917	2,953
Subject 3	522	530	548	1,600
Subject 4	704	756	683	2,143
Subject 5	566	551	575	1,692
Total				10,557

3.2.3 Image Segmentation Architectures

To allow for comparison of the approaches used, the well-known U-Net architecture [74] is used as a baseline and referred to as U-Net Baseline. Conformed by five levels, each block in the encoder path has a two 3 × 3 convolution, each followed by an activation function; in this case, a Rectified Linear Unit (ReLU) and a 2 × 2 max pooling with a downsampling stride of 2. In the decoder path, each block consists of a 2 × 2 up convolution, a concatenation with the output block having the same shape in the encoder path and a double 3 × 3 convolution, each followed by a ReLU.

The following approaches are considered sequential U-Net architectures. In these cases, the 2D US images were stacked to form a continuous representation of the femoral artery. The sequential U-Nets iterate through the volume slice by slice, each time using the segmentation of the previous slice with the current US image to form an input to the network, as shown in Figure 3.14. This way, prior spatial information is incorporated into the network to potentially improve segmentation results. Two different variations of this sequential U-Nets are used: U-Net Concatenated Input and U-Net Concatenated Bottleneck. The former concatenates the previous slice segmentation and the current US image, forming a two-channel input to the U-Net. In the latter, the segmentation and US image are processed by their own encoders and the concatenation occurs at the bottleneck of the U-Net. This aims to independently extract the spatial information from the previous segmentation without compromising the extraction of the most characteristic features of the US image.

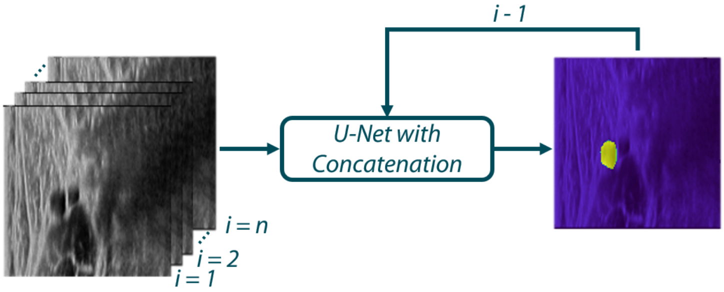

Figure 3.14: U-Net sequential architecture proposals iterate through the volume slice by slice, using the segmentation of the previous slice with the current US image to form an input to the network.

3.2.4 Training

The networks were coded in Python with PyTorch as the preferred deep learning framework and trained on an NVIDIA DGX A100. Images from the data sets were down-sampled from 512 × 323 to 128 × 128, in order to decrease memory and computational requirements. The networks were trained using a Binary cross entropy loss with a starting Learning Rate (LR) of 0.0001. If the validation loss did not decrease after four epochs, the LR was multiplied by a factor of 0.1. Each network training consisted of 30 epochs with a batch size of 25. Data sets of subjects 1, 3 and 4 were used to train the network. Validation and test sets were defined by subjects 2 and 5, respectively and were solely used for evaluating the performance of the networks.

3.2.5 Accuracy of Segmentation

The segmentations of the different approaches were assessed and compared to the manual segmented ground truth by calculating the Dice score. The resulting Dice scores are 0.633, 0.725 and 0.819 for the U-Net Concatenated Input, U-Net Concatenated Bottleneck and U-Net Baseline, respectively. Comparing the results between the approaches quantitatively (Table 3.3) as well as qualitatively (Figure 3.15) the U-Net Baseline achieved the highest performance with a Dice score of 0.819.

Table 3.3: Dice scores of the different approaches.

Approach	**Dice Score**
U-Net Baseline	0.819
U-Net Concatenated Input	0.633
U-Net Concatenated Bottleneck	0.725

3.2.6 Discussion

Surprisingly, the Dice score for the sequential architectures was not higher than the standard architecture. This might be due to the fact that the stacked images that represent the 3D volume were not spatially aligned in this scenario, causing some notable discrepancies on the location of the vessel from one slice to another, making it harder for the network to learn the vessel features. Since the stacked slices are considered a volume, it is expected that one image is the continuation of the other. In the U-Net Concatenated Input, this misalignment is considered as part of the input and by consequence, carried on. In the U-Net Concatenated Bottleneck, this misalignment error does not impact the results as much due to the separate feature extraction. The vessel segmentation is not compromised because the US image has a greater impact on the prediction.

It is also important to remark that due to the surrounding tissue and its anatomy, the femoral artery varies significantly from person to person. Considering this, the current number of subjects for training and validation could be increased, along with a greater age range between the volunteers. The latter improvement would enable one to assess the network's accuracy taking into consideration noteworthy vascular differences associated with age, such as vascular calcification and stenosis.

For the used data set, the U-Net Baseline was the most accurate approach to segment the femoral artery due to its highest Dice score. Although the presented ideas of the U-Net Concatenated Input and U-Net Concatenated Bottleneck are promising, the evaluation results can be improved. In order to do this, a spatially calibrated and tracked US probe, as described in the first section of this chapter, must be implemented for the US scan. Apart from this solution, one could improve the misalignment between slices by integrating a spatial transformer that allows one to align an image prior to segmentation.

Even though tested on different vessels (carotid artery and internal jugular vein), which somewhat weakens the comparability, the Mask R-CNN approach by Groves et al. [78] outperforms the presented methodology with a Dice score of 0.90. It seems that a two-stage detection algorithm providing region proposals provides benefits during the segmentation process. It is therefore recommended to use the approach by Groves et al. for the segmentation of vessels in 2D US images.

3.2.7 Section Summary

In this section, the aim was to provide an approach for reliable segmentation of arteries in US images to address research question **RQ2**.

By using a state-of-the-art deep learning approach for this segmentation task, a robust indication of the artery's location and size is provided to the physician and therefore facilitates the diagnostic process. The segmentation network has been trained and tested on US images of the femoral artery of healthy volunteers and thus proves its feasibility on realistic images. The segmentation does not only facilitate diameter measurements but also simplifies the differentiation between femoral artery and vein within the image. A limitation of this work is the lack of feasibility testing for abdominal aortas. However, as previously mentioned, it can be assumed that it is also applicable for this anatomy [75].

So far, approaches have been presented to support and simplify vascular diagnostics. On the one hand, by an in-situ visualization of the US images and on the other hand, by marking the position and size of the arteries in US images. In the following chapter, applications are presented and described that, according to the workflow, support and simplify the interventions.

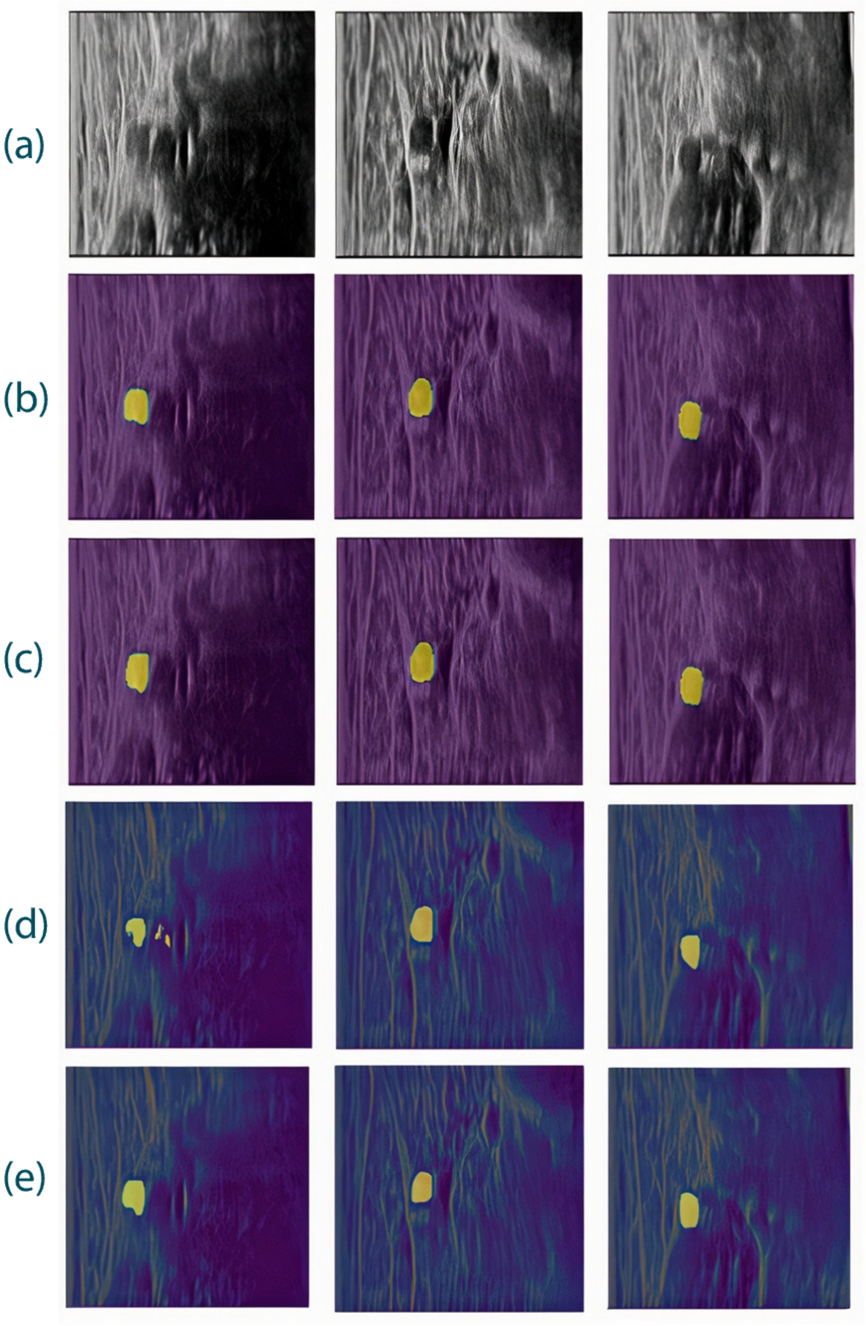

Figure 3.15: Comparison between (a) original US image (b) ground truth, (c) U-Net Baseline, (d) U-Net Concatenated Input, (e) U-Net Concatenated Bottleneck for three different sample images.

4 Facilitating Endovascular Interventions

Contents

In the previous chapter, facilitating systems for vascular diagnostics were discussed. In this context, a new approach for image acquisition (**RQ1**) was presented, plus an additional system for the actual diagnosis (**RQ2**). In this chapter, the two included sections present approaches to facilitate vascular access and endovascular interventions (Figure 4.1). These possess different requirements and are therefore separated into two sections.

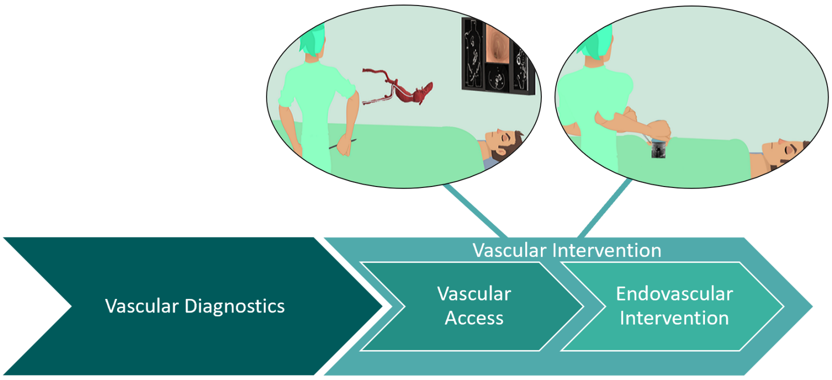

Figure 4.1: Workflow of vascular treatments with illustrations of futuristic systems to facilitate endovascular interventions.

4.1 Augmented Reality In-Situ Visualization of 3D Ultrasound for Femoral Access Guidance

Prior to the endovascular intervention, the physician needs to accurately puncture the femoral artery in order to provide an access port for the guide wires, catheters and stent graft systems. These punctures are usually guided using US imaging. To mentally align the 2D cross-sectional US image with the 3D anatomy of the groin area, a skilled and experienced sonographer is required for this approach as well. Especially for a US-guided arterial cannulation, an AR based in-situ visualization of the image may be beneficial as it shows the artery to be hit in the correct physical location. HoloLens 2 can be especially beneficial because it provides the user with an egocentric perception of the environment and enables hands-free interaction. Recent user studies have investigated the combination of 2D US with AR for needle guidance tasks with respect to conventional US. It was shown that the combination leads to reduced required time for the task [59, 60] and increased accuracy [38, 59, 80]. To overcome remaining disadvantages displayed by US (out-of-plane motion, difficulties in placing the probe to view both needle and target anatomy), this section continues in the direction of recent developments in AR US: It proposes the in-situ visualization of real-time 3D US using an HMD for needle guidance purposes to further improve image guidance. The difficulty with HoloLens 2, which has relatively limited computational power, is to achieve volume rendering at a target refresh rate of 60 Hz for a smooth and realistic visualization. Moreover, with the constant transfer of huge amounts of data, the difficulty is to show the volumes with minimal delay. This leads to the following research question:

RQ3 Is it possible to provide a target frame rate of 60 Hz when volume rendering

---

Parts of this section have been published in [79].

US volumes on a stand-alone AR device? Can the system achieve a latency close to real-time perception?

Additionally, the purpose of this section is to look into whether 3D US with AR results in higher success rates and shorter task durations because in-situ volumetric images might provide better image guidance. Since 2D US with AR has been shown to be advantageous over conventional 2D US, this work refrains from comparing it with conventional US and solely compares the combination of 3D US with AR versus 2D US with AR. To test initial feasibility of the setup, a qualitative study to gather feedback is first conducted. Based on the findings of this pre-study, the design of a quantitative main study for a US-guided femoral artery puncture is developed. In this context, it is hypothesized that 3D US with AR could result in increased success rates and decreased task length due to the enhanced visual guidance provided by volumetric pictures. As a secondary endpoint, the perceived task load for both combinations is measured with the assumption of a lower task load with the 3D US AR setup compared to the 2D US AR setup.

To this end, this work followed a mixed-methods approach, consisting of a qualitative pre-study followed by a quantitative main study. The conclusions of the pre-study were used to improve the HMD application and to design and implement the main study, which in turn serves to test the hypotheses. Furthermore, the methodically collected subjective assessments by experts within the pre-study do provide important information regarding the clinical applicability of the overall system, which is of interest to other researchers in this field. A technical evaluation, including latency of visualized images and frame rate of the application, is additionally performed to answer the research question.

Related Work—HMD-Based 3D Ultrasound Guided Interventions

Two recent studies [45, 81] showcased a similar system, namely, an AR HMD navigation system with a 3D US imaging system to guide surgical interventions. In [45], an in vitro study simulating a biopsy intervention showed that 80 % of participants were able to perform a biopsy on a 5 mm lesion. In [81], the platform was extended by a tracked standard scalpel to provide real-time information on the pose of the instrument. An in vitro experiment showed that the system can be used to guide a dissection task with a mean accuracy of 0.65 mm. Even though both studies showed promising results, the systems did not visualize the live volumetric US image, but instead a segmented structure from a previously acquired US volume. Therefore, any potential positional shift of the target anatomy may result in misleading visual guidance. In this work, on the other hand, the system streams and visualizes live volumetric images from a commercially available US station. Accordingly, any change in position or orientation of the target anatomy becomes immediately visible.

So far, technical setups for visualizing sonography in spatially-aligned real-time AR have been limited to 2D images. Accordingly, the main contributions to the field are:

1. A novel technical setup for visualizing volumetrically 3D US through an AR HMD with minimal latency and a sufficiently high frame rate;
2. A demonstration that this type of setup can offer benefits in image-guided tasks;
3. To show that 3D/volumetric data can offer additional benefits in spatial understanding over 2D data in this context.

At the same time, this work presents the difficulty of clearly visualizing relevant structures when surrounded by occluding objects and highlights the need to address this issue.

4.1.1 System Description

The centerpiece of the system is HoloLens 2, which provides the visualization of intraprocedural image data and performs US probe tracking (Figure 4.2).

The HoloLens 2 application was developed with Unity 2020.3.7f1 (Unity Technologies, San Francisco, CA, USA). Instead of relying on the HoloLens' onboard hardware, which might be insufficient for computationally expensive real-time volume rendering, the Holographic Remoting Mode (HRM) [82] was utilized. This mode enables remote rendering on a capable workstation, streaming the rendered images to the HMD while the user is wearing them. The remote rendering workstation in this experiment was equipped with an Intel Xeon(R) E5-2697 v4 CPU, an NVIDIA Quadro M6000 GPU, and 64 gigabytes of RAM. Consequently, even computationally expensive stereoscopic volume rendering could potentially be performed at a target frame rate of 60 Hz. To visualize US images and volumes in-situ, i.e., attached to the US probe, the probe must be tracked spatially. To minimize technical complexity, an inside-out tracking approach compatible with the HRM by using the built-in QR code tracking was the preferred option [83]. As the HRM does not provide access to the sensor data, it was not possible to utilize the tracking approach using retroreflective spheres (Section 3.1). For US data acquisition, an EPIQ 7 station (Philips Medical Systems International B.V., Best, The Netherlands) was used that allows real-time streaming of image data to the computer via a proprietary network protocol provided by Philips.

4.1.2 Ultrasound Image Data Streaming and Volume Rendering

For the qualitative pre-study, which was not limited to a specific use case, the X6-1 3D US probe was utilized. The quantitative main study, on the other hand, was performed with a novel 3D probe (XL14-3) that has a linear matrix array consisting of 65,000 elements. Therefore, it features the advantages of a linear probe (same line density at depth, including high lateral resolution) while at the same time being able to acquire a real-time volumetric US image.

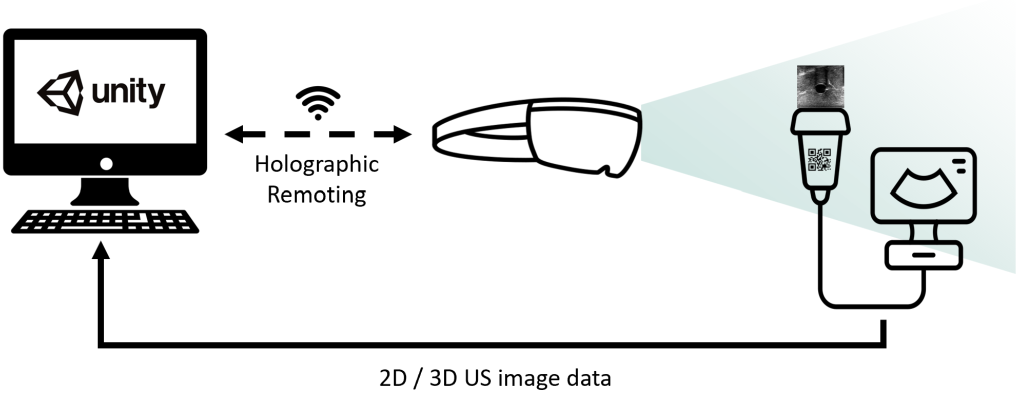

Figure 4.2: The general technical setup consisting of remote rendering workstation running the Unity application, the HoloLens 2 displaying the rendered images while tracking the US probe and the US station sending images or volumes to the workstation. Solid lines indicate an Ethernet connection and dashed ones wireless connections.

Eight bit 2D and 3D image data were transmitted in real-time from the US station to the Unity instance running on the computer using the proprietary network protocol. To perform volume rendering (GPU-based raycasting in this case), the choice of an appropriate Opacity Transfer Function (OTF) is needed [84]. This transfer function maps the intensity value I of each voxel to an according opacity value α. A simple piecewise linear OTF is sufficient for visualization of structures embedded in areas with low signal intensity [85]. A US volume showcasing vascular structures in a homogeneous hypoechoic tissue can be considered as such a case. Therefore, the OTF for this application is defined as

$$\alpha(I) = \begin{cases} 0, & \text{if } I < L_l \\ a(I - L_l), & \text{if } L_l < I < L_u \\ a(L_u - L_l), & \text{if } I > L_u \end{cases} \tag{4.1}$$

where L_l is the lower limit, L_u is the upper limit, and $a \in [0, 1]$ is a scaling factor. Before the participant's task began, supervisors prepared the US settings (including volume rendering parameters) to produce the optimal visualization of anatomical structures in 2D and 3D images. The settings are summarized in Table 4.1.

4.1.3 Spatial Calibration for Tracked Ultrasound Probe

In this work, the marker had a size of 6 × 6 cm, which was the minimum size to reliably track the code at an arm's length distance. To increase rotational movement freedom and based on the feedback of the pre-study, the probe was equipped with

Table 4.1: The US station settings used for the pre-study (probe X6-1) and the main study (probe XL14-3).

	X6-1		**XL14-3**	
	2D	**3D**	**2D**	**3D**
Depth [cm]	Variable	Variable	4.5	4.5
FOV (azimuth × elevation)	Variable	Variable	NA	0°× 90°
Gain [dB]	0	0	0	0
Image brightness	Variable	Variable	25	35
$L_l; L_u; a$	NA	0; 255; 0.40	NA	0; 255; 0.14
Refresh rate [Hz]	Variable	Variable	8	8

a second QR code. Therefore, even if line-of-sight is not guaranteed for the first QR code, the pose of the probe is still known due to the second tracked QR code. According to [83], the QR code can be detected up to an angle of ±45°. Assuming that one can just add the rotational shift of the second QR code with respect to the first one (50°), the adapted system offers a detection range of up to ±70°. The calibration was performed for one marker only. Having the relative transformation between the two codes enables them to extend the calibration to the second one.

The attached QR code provides the current position and orientation of the US probe with respect to the HoloLens coordinate system. To visualize the US image based on the QR code pose in-situ, it is necessary to find the spatial transformation from the QR code origin to the US image coordinate system by means of a spatial calibration. The approach in this work is based on point cloud matching of geometrical shapes (spheres and cylinders) within a commercial US calibration phantom (CIRS Inc., Norfolk, VI, USA).

In order to visualize a voxel $\mathbf{v}$ (or pixel for 2D) of a US image in-situ, the following equation is required:

$$ {}^{\mathcal{HL}}\mathbf{v} = {}^{\mathcal{HL}}\mathbf{T}_{\mathcal{PR}}\,{}^{\mathcal{PR}}\mathbf{T}_{\mathcal{USMM}}\,{}^{\mathcal{USMM}}\mathbf{A}_{\mathcal{US}}\,{}^{\mathcal{US}}\mathbf{v} \tag{4.2} $$

where ${}^{\mathcal{A}}\mathbf{v}$ is a voxel in coordinate system $\mathcal{A}$ and ${}^{\mathcal{A}}\mathbf{A}_{\mathcal{B}} \in \mathbb{R}^{4\times 4}$ is an affine transformation between coordinate system $\mathcal{B}$ and $\mathcal{A}$. The coordinate systems $\mathcal{HL}$, $\mathcal{PR}$, $\mathcal{USMM}$, and $\mathcal{US}$ refer to HoloLens, US probe, volume in mm, and volume, respectively. The unknown transformation ${}^{\mathcal{PR}}\mathbf{T}_{\mathcal{USMM}}$ can be calculated by closing the transformation loop as illustrated in Figure 4.3 and by using the following equation:

$$ {}^{\mathcal{PR}}\mathbf{T}_{\mathcal{USMM}} = \left({}^{\mathcal{HL}}\mathbf{T}_{\mathcal{PR}}\right)^{-1}\,{}^{\mathcal{HL}}\mathbf{T}_{\mathcal{PH}}\,{}^{\mathcal{PH}}\mathbf{T}_{\mathcal{CT}}\,{}^{\mathcal{CT}}\mathbf{T}_{\mathcal{US}}\,{}^{\mathcal{US}}\mathbf{T}_{\mathcal{USMM}} \tag{4.3} $$

where the coordinate systems $\mathcal{PH}$ and $\mathcal{CT}$ refer to phantom and CT, respectively. In order to calculate ${}^{\mathcal{PR}}\mathbf{T}_{\mathcal{USMM}}$, the two missing transformations ${}^{\mathcal{PH}}\mathbf{T}_{\mathcal{CT}}$ and ${}^{\mathcal{CT}}\mathbf{T}_{\mathcal{US}}$ have to be determined. A landmark-based registration provides ${}^{\mathcal{PH}}\mathbf{T}_{\mathcal{CT}}$, as the QR code is placed on the phantom surface in a known position, and the corner positions can be defined both in the CT and HoloLens coordinate system. On the other hand, a point cloud matching of the segmented geometrical shapes of the phantom within the CT and US coordinate system can be used for calculating ${}^{\mathcal{CT}}\mathbf{T}_{\mathcal{US}}$. Point clouds from CT and US data are created by applying a Canny edge detection to the volumes. Having both point clouds and an initial pre-alignment, ICP is applied to find ${}^{\mathcal{CT}}\mathbf{T}_{\mathcal{US}}$ with 200 randomly sampled points from each model. Further details on the calibration and its accuracy can be found in [86].

For displaying the 2D US image, the middle slice of the US volume was selected. Since the pose of the 2D plane in the volume is known, no further calibration was necessary to display the image in-situ.

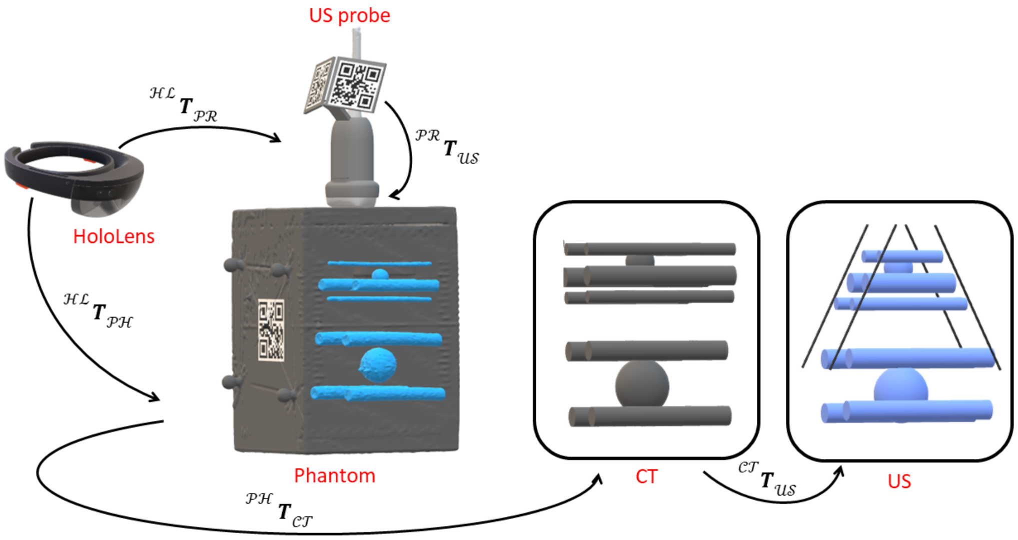

Figure 4.3: Transformations (black arrows) between the different coordinate systems (red) necessary for probe calibration. A multi-modality calibration phantom containing spheres and cylinders is used for the point cloud based registration approach.

4.1.4 Phantom Fabrication

As the qualitative pre-study was not limited to any specific medical field, and due to its exploratory purpose, an anthropomorphic torso phantom was used (Figure 4.4, FAST Trauma Training Model, CAE Inc., Blue Phantom, Montreal, QC, Canada). This US-capable phantom contains several vessels and organs (e.g., pulmonary vessels, ascending aorta, liver, heart, spleen, bladder, and kidneys).

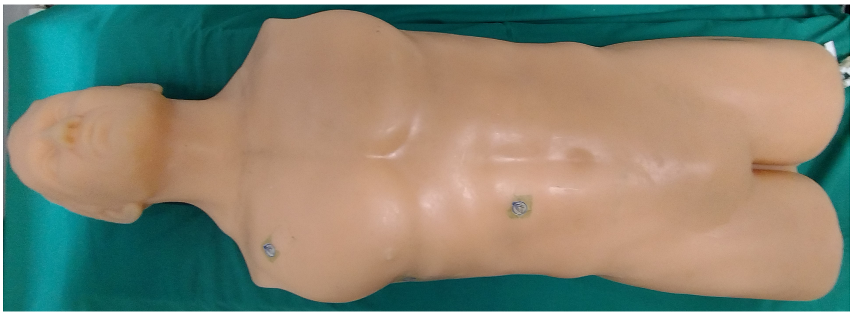

Figure 4.4: The US-capable torso phantom contains several organs and vessels and is therefore suitable for the exploratory purpose of the qualitative pre-study.

For the main study, phantoms were custom-made to fulfill the following requirements: US-capable, perfusable artificial vessels, including a bifurcation, repairable, and a transparent tissue with an opaque skin layer. To avoid any bias from seeing previous insertion channels in the US image, which was also mentioned in a previous work [38], the repair function was essential. To this end, ballistic gel (Clear Ballistics, Greenville, SC, USA), which allows remelting once heated, was chosen [87–89].

A total of 1.5 kg of gel was cut into small pieces, placed in an oven dish, and heated in a kitchen oven at 125°C for 2 hours. Thereafter, 2 w/w % paraffin wax (Bayerwald Brennstoffe GmbH, Arrach, Germany) and 0.5 w/w % solid glass spheres (⌀ 0–63 μm, Boud Minerals, Lincolnshire, UK) were slowly added to increase acoustic attenuation and backscattering, respectively [90]. Hereafter, the mixture was placed in the oven for another 3 hours at 125°C to remove introduced air bubbles. The liquid gel with additives was then poured into a rectangular container (70 × 130 × 150 mm) with a silicone vessel including a bifurcation (Vascular International, Kerns, Switzerland), as illustrated in Figure 4.5(a). It was then allowed to cool down for 24 h, and the silicone vessel was removed by gently pulling it out (Figure 4.5(b)). To produce the skin layer, a brown liquid silicone dye was added to the remaining gel until it was opaque and then poured into a different container of the same size until a height of ~5 mm was reached (Figure 4.5(c)). In total, six phantoms were produced according to this procedure.

To perfuse the vessel with a pulsatile flow, the single end within the custom-made phantom is connected to the vi-box (Vascular International, Kerns, Switzerland). This device features a water reservoir and two small, battery-operated pumps, which supply pulsatile or continuous flow. The custom-made phantom, the skin layer, and the vi-box form the setup for the quantitative main study (Figure 4.5(d)).

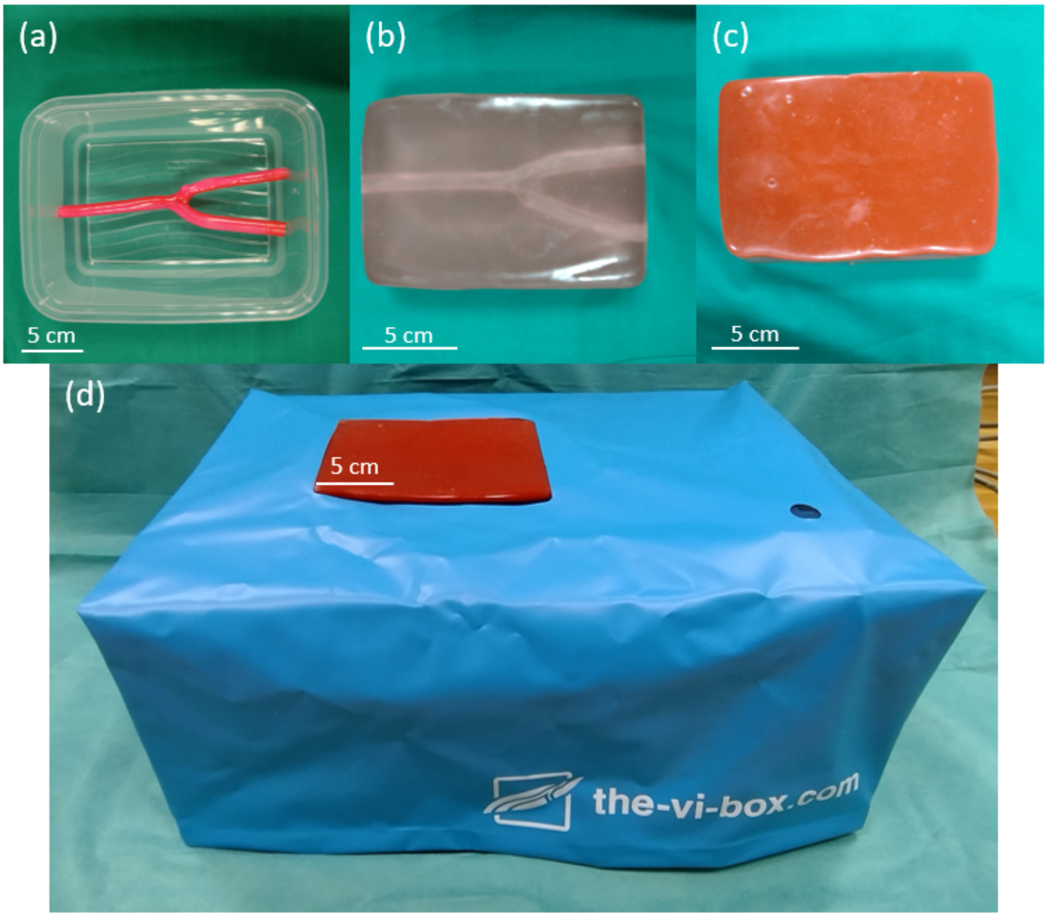

Figure 4.5: The vessel phantom for the main study. (a) The container, including a silicone vessel with bifurcation before adding ballistic gel. (b) The gel phantom after removing it from the container and the vessel. (c) The opaque skin layer on top of the phantom prevents the participants from seeing the vessel. (d) The phantom placed inside the vi-box which contains a water reservoir and pumps to perfuse the artery with a pulsatile flow.

4.1.5 Mixed Methods & Technical Evaluation

This research followed a mixed-methods approach, combining a qualitative pre-study with a quantitative main study. With this exploratory sequential design, the results and conclusions of the pre-study were used to improve the application and inform the planning and execution of the main study. To acquire participants for both studies, convenience sampling was performed, resulting in eight participants for the pre-study and 18 for the main study.

Qualitative pre-study

The pre-study consisted of a think-aloud session followed by a semi-structured interview. First, participants were introduced to the context and agenda of the experiment, as well as asked to read and sign the consent. In the following think-aloud session, participants were asked to voice their thoughts while freely using the setup shown in Figure 4.2 on a US torso phantom (Figure 4.4), e.g., trying to locate and view various organs. Participants first had the opportunity to familiarize themselves with the US station, particularly its 3D mode, before beginning the session with the AR visualization. All participants started with conventional 2D US, followed by 3D US. After they decided that they had sufficiently tested each mode, the semistructured interview took place. The experiments' audio was recorded and transcribed by the interviewer. The same person then performed a structuring qualitative content analysis (based on methods proposed by Kuckartz [91]) on the transcripts using Taguette [92]. Categories were initially formed deductively based on the existing literature [38] and then iterated upon inductively throughout the coding process, particularly the more granular subcategories for each major category. Segments were coded on a level of semantically closed and coherent phrases, usually encompassing a full sentence, but occasionally also multiple sentences.

Quantitative Main Study

As before, participants were introduced to the context of the experiment, and asked to read and sign the informed consent. Each participant was asked to puncture the vessel above the bifurcation with a needle (1.4 mm diameter, 17G, length 70 mm). The participants were supposed to perform the task once with 2D US and the HMD and again with 3D US and the HMD. The order was randomly chosen to minimize carryover effects. For each mode, a different phantom was used such that no insertion channels were visible. Note that the (usually echogenic) insertion channels were closed after each individual experiment by means of local heat using a soldering iron to prevent them from accumulating and interfering with later experiments.

Before the actual experiment, each participant was allowed to familiarize themselves with the in-situ visualization for 2D and 3D images by scanning the calibration phantom (Figure 4.3) without a time limit. As this phantom contains cylinders, the users had the chance to experience the visualization of vessel-like structures in the 2D and 3D mode.

The primary endpoints were task duration (time to identify the bifurcation and placing the needle) and successful puncture of the vessel above the bifurcation. To this end, the time was taken from the initial placement of the probe on the phantom until the participant signaled that the task was finished. A visual inspection of the transparent phantom by the supervisor allowed him/her to verify if the vessel was successfully punctured (Figure 4.6). After both attempts, the participant was then asked to fill out two NASA Task Load Index (TLX) questionnaires [93], once for each modality.

Statistical analysis was performed in Python (version 3.7.4 for Windows), including the scientific utility package *pingouin* (0.5.0) to perform hypothesis tests ($\alpha_{total} = 5\%$, individual test α include Bonferroni–Holm corrections for multiple testing).

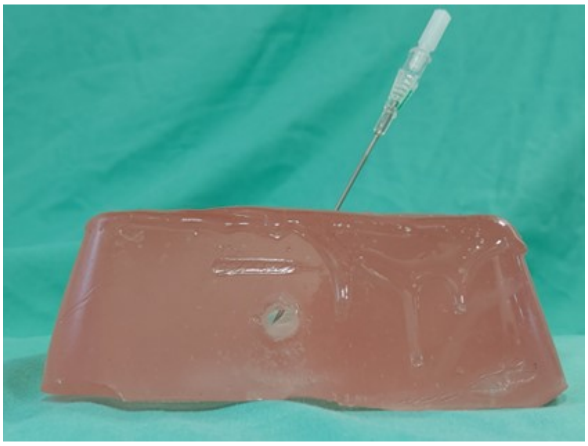

Figure 4.6: Photograph of the phantom with a placed needle to illustrate the easily identifiable successful puncture.

Technical Evaluation

Low latency of visualized US volumes and images is crucial for the proposed use-case, as advancing the needle towards a critical structure should be shown in near real-time. In this setup, the latency was measured by recording a slow motion video through one lens of HoloLens 2 while capturing the rendered volume on the lens and on the US station screen (Figure 4.7). During the recording, the depth of the US image was changed frequently. With a recording frequency of 240 Hz, a temporal resolution of 4.17 ms was achieved. For the actual measurement, the frames were counted between the visible change on the US station and the virtual US volume. The latency is therefore the delay between the visualization of the US station and the HMD visualization.

The target frame rate for any display-based application is 60 Hz to ensure smooth visualization for the user. The HRM provides a feature to measure the current frame rate [94]. Therefore, the refresh rate was simply obtained by checking the according value when tracking the QR code and visualizing the US volume. In the pre-study, participants mentioned latency issues only with 3D US. Accordingly, these two measurements were only conducted for this modality, and 2D US can be assumed to have equal or lower latency.

Figure 4.7: The schematic setup for measuring the latency of displayed US volumes. A slow-motion video captures the US station screen and the rendered US volume.

4.1.6 User Study Results, Latencies & Frame Rate

Qualitative Pre-Study

The qualitative pre-study included eight participants ($\mu_{age} = 31.9, \Sigma_{age} = 4.3$, five were female, three male). Six participants were physicians. Specializations included radiology, vascular surgery, anesthesiology, and internal medicine; all but one were residents. The other two participants were medical students close to finishing their studies and with minor clinical experience. Except for the two medical students, all participants regularly performed sonography (either diagnostically or interventionally), with four of them performing this routinely. All but one participant had no prior experience with AR.

Figure 4.8 illustrates the HoloLens 2 user's view of the imaged bladder. Six major categories were identified and are outlined in Table 4.2, with the examples translated from German to English. Each category was also divided into subcategories, e.g., 'Benefit—Manual Coordination', 'Use Case—Biopsies', or 'Limitation—Tracking Unwieldy'.

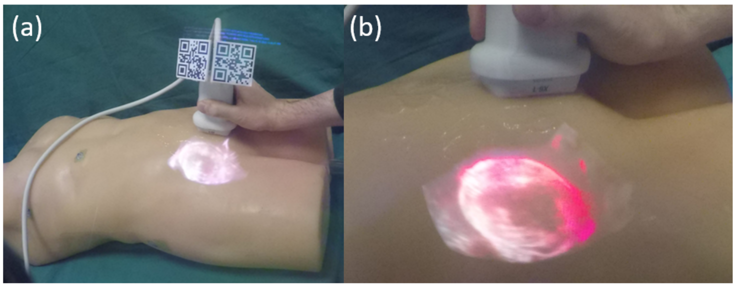

Figure 4.8: Photographs taken through a lens of HoloLens 2. Note that this results in worse overlay accuracy and color shifting compared to wearing the HMD. (a) US probe, including QR codes and the in-situ visualized virtual volume of the bladder. (b) Close-up photograph of the volume.

Table 4.2: Main categories identified in the qualitative content analysis, including definitions, examples and summaries per category

Category	**Definition**	**Example**	**Summary**
Benefit	Segments mentioning a positive/helpful aspect of viewing US in AR (both 2D and 3D)	’I liked it better with the glasses [HMD] simply because the image was larger [. . .]’ (Participant 6) ’You basically see how the image changes, directly, without having to somehow reconstruct and think about the 3D from the screen’ (Participant 5)	The main benefits that were noted were that AR allowed for better manual coordination (both with the stationary and tracked overlay) and spatial understanding, often noting the ‘tomographic’ and ‘scrolling’ impression AR offers. Other benefits were that the AR image could be visualized larger and positioned freely.
Familiarity	Coded when voicing unfamiliarity, being used to something different or mentioning familiarization with our system	’Yes, I’m looking at the stationary image up here because then I can move the US probe like I’m used to.’ (Participant 1) ’Right, now this is tricky. Because of course now you really only see the 3D image, right? Hm, that takes some getting used to, just because you don’t do that often.’ (Participant 7)	Many participants mentioned that they were unfamiliar with 3D sonography and its issues of occlusion and noise. Many also said they were used to a stationary image at the side (often in context of looking at or preferring the stationary AR image, rather than the tracked view.) The majority opined that getting used to this technology is only a matter of practice and not a major hurdle. Additionally, some radiologists mentioned that they are used to viewing volumetric images and framed this as learning to view just another imaging modality.
Limitation	Segments describing negative aspects, expressing frustration or not being able to do things in a certain way	’Okay, it’s delayed again here’ (Participant 3) ’Well you can’t just go through your motions like that. This stupid QR code has to be visible somehow.’ (Participant 4)	All participants either struggled with or criticized the tracking of the probe as being unwieldy. Many noted that they found the volumetric visualization unintelligible, some describing it as “tiny clouds” in front of the organs. Several participants were confused by or commented on the unusual anatomy of the dummy (e.g. the position of the right kidney.) Some also noted latency issues in the 3D mode.

Preference	Statements indicating preference for a type of visualization, e.g. conventional or 3D AR	’And that was a bit easier without the glasses [HMD] in the 3D mode’ (Participant 2) ’Difference from Augmented to screen is relatively big and Augmented is just much more user-friendly because you could orient yourself.’ (Participant 5)	Half of the participants noted preference for the floating mode, often in context of being used to a stationary image away from the situs. Other than that, preferences seemed to vary and were often tied to specific issues like tracking issues, volumetric readability or spatial understanding.
Use Case	Coded when participants suggest or speculate on use cases/applications of our setup	’I actually think if you’re getting started with sonography it’s going to be much easier if you’re doing it with the glasses [. . .]’ (Participant 4) ’Generally I feel like this is for needle placements, like I said, with the HoloLens, if you look at it and insert the needle where you’re looking, that is better than looking at a screen.’ (Participant 7)	By far the most commonly mentioned use-case were image-guided procedures, particularly needle placements/biopsies. This not only occurred in the interview when being specifically asked about biopsies as a use-case but also occurred spontaneously (e.g. during the think-aloud phase.) Some participants noted that it would be particularly useful for complex and elective procedures rather than routine tasks with low accuracy requirements. Another commonly suggested use case was for beginners learning the basics of sonography. Others noted situations where the AR-HMD could replace screens to make more room, e.g. crowded operating or trauma rooms.
Verdict	Judgements about the technology in its entirety, particularly regarding whether it is useful or practical. If specific aspects are mentioned, either positively or negatively, they are coded as ‘Benefit’ or ‘Limitation’, accordingly.	’Yeah, well, somehow this 3D thing isn’t really useful for me I’d say.’ (Participant 4) ’But that’s pretty sexy, having the US image directly on top of the body somehow, like, overlaid.’ (Participant 6)	Verdicts were often unspecific and either positive (e.g. calling the technology ‘awesome’ or ‘pretty’) or negative, mentioning difficulties with AR, particularly the volumetric view. Several participants also mentioned that this setup may be unnecessary or not helpful, particularly in diagnostic contexts. Some also mentioned that they have learned US-guided procedures without AR and perform them sufficiently well, i.e. they do not see a need for additional technology.

Quantitative Main Study

The experiment included 18 participants ($n = 18$), of whom five were physicians with varying specializations and degrees of experience, as well as one medical student. The remaining participants were engineers with previous experience working with sonography.

Participants completed the task significantly faster when using 3D AR compared to 2D AR ($\mu_{2D} = 187.4$ s, $\mu_{3D} = 134.1$ s, $\mu_{\Delta} = -53.3$ s, $\Sigma_{\Delta} = 105.6$ s), with a relative decrease in task completion time of 28.4 %. As the intraparticipant differences in task completion time sufficiently followed a normal distribution (Figure 4.9(b)), the hypothesis was tested with a paired t-test, and the significance level of 5 % was adjusted for multiple testing ($H_1 : \mu_{3D} < \mu_{2D} \approx 2.36\,\% < 2.5\,\%$).

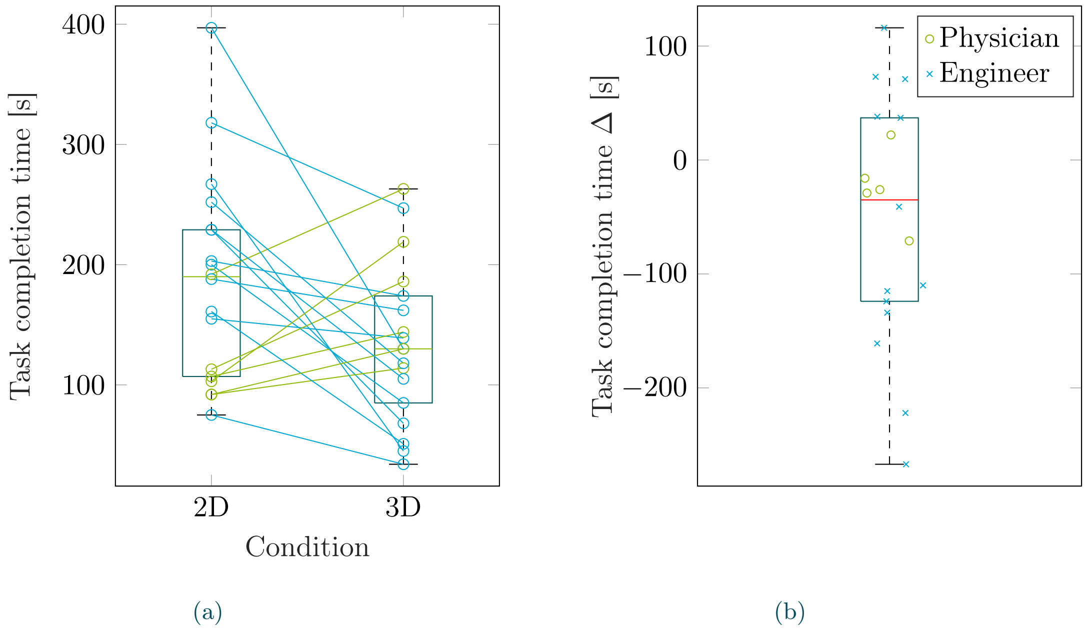

(a)

(b)

Figure 4.9: (a) Box-plot and dot-plot showing task completion time; lines connect the data points that belong to an individual participant. The blue color indicates a decrease in time, while the green color indicates an increase. (b) Box-plot and dot-plot showing the difference in task completion time. Negative values indicate less required time with 3D US and the HMD.

To test the second hypothesis, i.e., that participants successfully hit the target structure more frequently with 3D AR than with 2D AR, an exact McNemar test was performed. However, the differences (Table 4.3) were not statistically significant ($p \approx 28.91\,\% > 2.5\,\%$). Due to the small sample size and the correspondingly low statistical power, it was decided not test the secondary hypothesis, i.e., that performing the task with 3D US reduces the subjective workload (measured via TLX) compared to 2D US. Another reason for this decision was that participants noted that they felt some items to be irrelevant (e.g., temporal demand) and accordingly answered them somewhat arbitrarily. Because per-item weighing was not included, this introduces further noise and in turn, further lowers the power of a potential test. Figure 4.10 shows the HoloLens users' perspective of the 2D and 3D US image in-situ.

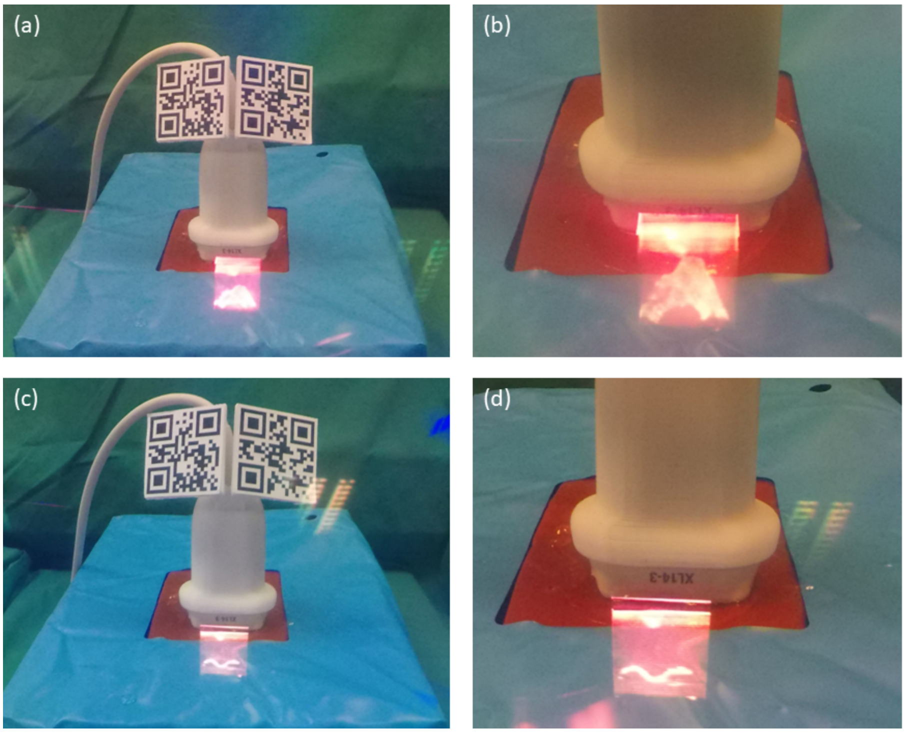

Figure 4.10: Photographs taken through a lens of HoloLens 2. (a) US probe, including QR codes and the in-situ visualized virtual volume. (b) Close-up photography of the volume showing the beginning of the bifurcation. (c) US probe, including QR codes and the in-situ visualized virtual image. (d) Close-up photography of the cross-sectional image showing the beginning of the bifurcation.

Table 4.3: Results of the vascular puncture attempts.

	2D US with HMD	**3D US with HMD**
Successful puncture	9	13
Unsuccessful puncture	9	5

Technical Evaluation

Latency was measured at 49.90 ± 12.92 ms (mean ± standard deviation) with minimum and maximum values of 25 and 75 ms, respectively. The diagnostics tool provided by the HRM showed a constant frame rate of 60 Hz while tracking the QR codes and rendering the streamed US volumes.

4.1.7 Discussion

The results show that in-situ overlays of real-time 3D US images can offer benefits over 2D images for US-guided needle placements, i.e., a reduction in task completion time. It appears, though, that this may depend on several conditions, i.e., when viewing US through an AR HMD, 3D images are not, per se, superior to 2D images. Particularly, it must be ensured that target structures can be clearly distinguished from noise or occlusion – an issue not present with 2D US images due to their cross-sectional nature. This may be solved by choosing an appropriate use-case/anatomical structure, through fine-tuned volumetric rendering or potentially through additional segmentation and tracking within the US volume. All approaches are promising topics of research that can further evaluate how and in which contexts real-time 3D US can be advantageously utilized via an AR HMD. The qualitative results also support notions from previous publications that AR visualization of live US images can improve spatial understanding and reasoning as well as facilitate hand-eye coordination. The latter appears to be the case even when images are not spatially overlaid and instead 'float' above the probe, i.e., when hands and US images can be viewed simultaneously. This is relevant because removing the need for accurately tracking the probe can reduce the technical complexity considerably. Regarding spatial understanding, the proposed setup does not only alleviate the need for mentally transforming 2D US images into 3D anatomical structures—viewing 3D US images also enables a more three-dimensional impression (Figure 4.8), given sufficiently echogenic structures.

In cases where even a sophisticated volume-rendering technique fails to adequately visualize the target anatomy or medical instruments, it is worth investigating the display of the three orthogonal slices as an alternative. This approach was also suggested by a participant in the pre-study who routinely performs ultrasound-guided procedures. Combined with an automatic detection of the needle and visualizing the according slice, as shown in [95], one can utilize the advantages of 2D and 3D US simultaneously.

Though the results can show the general potential and properties of visualizing 3D US via AR HMDs, it should be cautioned against generalizing them into clinical contexts due to various limitations outlined below.

Limitations

For both the pre-study and the main study, a potential bias due to a novelty effect or social desirability cannot be excluded. It was attempted to minimize these effects by comparing only AR HMD conditions and not explicitly mentioning what is considered as technical innovation. In addition, the qualitative study consisting of the interviews and data analysis was conducted by a person who was not involved in the technical development and is therefore less prone to bias the results.

Pre-study

The sonography setup of the experiment was different from those typically used for clinical diagnostics: As opposed to sitting on a chair with the US system located towards the head of the patient, participants had to stand (due to the height of the dummy lying on the experiment's table) with the US system located at the dummy's feet. Multiple participants remarked that this was slightly confusing. As a result, the arrangement for the main study was changed accordingly, and it is suggested that, even for studies in a lab setting, arrangements should attempt to accurately reflect those found in the field.

The anatomy of the dummy (location and echogenicity of anatomical structures) was repeatedly mentioned to be surprising or confusing to participants. Furthermore, the tracking via the QR marker was an unwieldy addition to an already large 3D US probe. It also required users to move the probe in a way that kept the QR marker visible. All of these factors were likely an unwanted distraction throughout the task. Investigating other probe tracking approaches, e.g., using retroreflective spheres, as described in Section 3.1, would be an important step to further develop this system.

Main Study

The quantitative main study consisted of a relatively small sample size of 18. Additionally, only five participants were physicians, the intended user group of the system. Accordingly, the results cannot be generalized to physicians who perform US-guided tasks on a regular basis. Both aspects were due to difficulties in acquiring a sufficient number of volunteering physicians and time constraints.

Task completion times were relatively high when considering previous studies (mean completion times: 66.4 s [38]; 13 s [59]; 116.9 s [60]). An actual comparison is difficult as the tasks and previous familiarization differ between each study. Exemplary, the participants in [59] performed not only one but ten punctures in a vessel phantom. Further, it remains unclear if the orientation phase was part of the measurement. This work showed that the task completion time was significantly reduced with 3D US and the HMD. However, it is necessary to emphasize that this is only valid for this lab scenario, which does not accurately reflect a vascular puncture in a real patient.

The power of the data set regarding the second hypothesis (improved accuracy when using 3D AR compared to 2D AR) was low due to a small sample but also because of the binary nature of the measured variable. However, even though a continuous variable (e.g., distance to a target) may offer a more granular and statistically robust measure of accuracy, it may also significantly complicate the technical complexity by requiring a highly accurate tracking modality.

The success rates of 50 % and 72 % for 2D and 3D US, respectively, appear to be relatively low in this setup, which might be due to the fact that the majority of the participants were engineers. However, it is assumed that another major influencing factor is the limitations of the phantom used. The main purpose of the fabricated phantoms was to generate a realistic US-capable test subject while avoiding animal experiments. Even though the chosen materials feature important characteristics such as a repair function and realistic acoustic attenuation and back-scattering, several drawbacks were experienced during the main study. First, the perceived haptic feedback during needle insertion was different compared to human tissue. In particular, physicians mentioned that more force was necessary to insert the needle. Moreover, the wall-less structure of the dummy vessel did not provide any feedback once the lumen was reached, whereas in a real case, physicians may feel the perforation of the vessel wall. Additionally, blood will discharge from the external end of the needle once successfully it is placed in an artery, providing important feedback. However, the pulsatile pump of the vi-box could not provide sufficient pressure to do so in this setup. Lastly, the visibility of the needle in the US image and volume was challenging, which led to a limited visual guidance during the task. This restricted visibility of the needle may be due to the ballistic gel surrounding the needle, in addition to the probe, which, although a state-of-the-art linear 3D probe, does not provide the same image quality as a linear 2D probe.

Based on the feedback of the participants, the vessel structure, including bifurcation, was easily identifiable in the rendered US volume. Indeed, the volume rendering approach might be insufficient in a real patient as the vessel is surrounded by more hyperechogenic tissues, such as different muscle layers. This is an important factor because differentiating between target and occluding structures was identified as a major difficulty in the pre-study. Accordingly, this phantom can be considered a best-case scenario for the approach. As this is a study in a lab setting with a small sample size, it may be argued that it is acceptable to have best-case conditions to establish a theoretical base for more complex and realistic experiments in the future. Accordingly, future work could further investigate how real-time US volume renderings could more clearly visualize structures and instruments.

Technical Evaluation

The latency measurements show that the system introduces only a slight delay in visualizing the US volumes. However, the measured time span does not reflect the time from image generation until image visualization but just the additional delay compared to the normal visualization on the US station screen. Still, a mean latency $< 50\,\text{ms}$ is a satisfactory result, also due to the fact that 50 ms is considered to be the threshold above which user experience seems to degrade in some of the most time-critical games [96].

The diagnostics tool of the HRM mode showed that the application runs at the target frame rate of 60 Hz, which confirmed the initial assumption that the HRM provides sufficient computing power for QR code tracking and volume rendering. A standalone application running solely on HoloLens 2 would be generally preferable but is currently not possible due to the small size of the HMD and its therefore limited hardware capabilities.

In this work, technical overlay accuracy tests were not performed. Even though this is an important evaluation criterion, one can argue that sub-millimeter accuracy is not crucial for this application as (1) the in-situ visualization is just an indication of the actual target anatomy position, and (2) the needle and the target anatomy are visualized in the same coordinate system (US volume or image), reducing the required tracking and registration accuracy. To be more precise, even if the in-situ visualization error leads to a slightly incorrect initial insertion of the needle, the interventionist can compensate for this once the needle becomes visible in the US volume, in which the target anatomy is also visible. According to [83], a QR code's position may drift up to $\pm\ 2.5\,\text{mm}$ during continuous detection, while the probe calibration error was quantified to 3 mm [86], leading to a maximum error of around 5 mm.

4.1.8 Section Summary

In this section, an AR system was presented that enables in-situ visualization of real-time 3D US image data to facilitate femoral artery punctures by showing volumetrically the artery and the needle. To address **RQ2**, the system uses a remote rendering approach, and the technical evaluation showed that this solution indeed provides the computational power for a sufficiently high frame rate and minimal latency.

Furthermore, the experiments show that this may offer additional benefits in US-guided tasks (i.e., reduced task completion time) over 2D US images viewed in AR. It was also possible to reproduce the results from the previous related literature that in-situ visualization of US with AR can positively influence spatial understanding. At the same time, difficulties in distinguishing relevant structures from noise and occlusion were identified as a major limitation of this technology. However, when target structures are well distinguishable, AR HMDs offer a vivid spatial visualization of real-time 3D US. As a result, one can argue that future research should aim to overcome the issue of visual occlusion so that this promising technology may be tested in more practical contexts.

In the context of workflow (Figure 4.1), this application provides a simplified and radiation-free way to accurately puncture the femoral artery so that the endovascular intervention can subsequently begin.

4.2 Endovascular Navigation via Holographic Catheter Tip Visualization and Virtual Angioscopies

Once access to the vessel is established and the endovascular instruments are positioned in the artery, the physician needs guidance to advance the instruments to the respective pathologies. As elaborated in Section 1.3.5, the system should therefore provide a 3D visualization of the vascular structure, including the position and orientation of endovascular instruments with respect to it. From a technical standpoint, the following research question was raised:

RQ4 How can we register the vascular 3D model with the tracked endovascular tools for a combined visualization? Which tracking approach can be utilized for this kind of intervention, and what accuracy is achievable?

To answer this question, this section proposes the combination of several navigation and imaging techniques and uses an intuitive and innovative way of visualization. The approach includes the use of an EM tracking system that does not require line-of-sight for guiding the catheter tip within 3D models based on preoperative CT scans. HoloLens 1, which enables hands-free interaction, is used to render the navigation data (namely the 3D aortic model including the catheter tip, orthogonal views of the preoperative CT scan, and pose-dependent Virtual Angioscopy (VA) images built from this scan) in the real environment (Figure 4.11). The aim of this study was to describe the navigation system and evaluate the position accuracy of the catheter tip in an end-to-end experiment with a 3D printed patient-specific phantom and two different markers for the registration between the EM and CT coordinate system. This work also assessed the feasibility and latency of transmitting and displaying pose-dependent VA images using two different lossy compression formats on the AR glasses.

Parts of this section have been published in [97, 98].

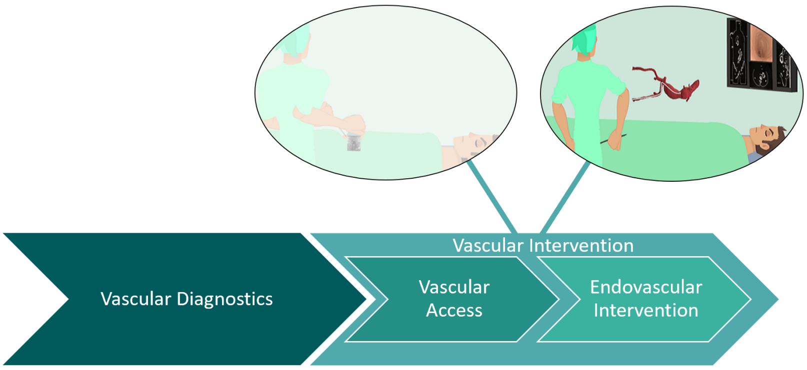

Figure 4.11: Workflow of vascular treatments with a highlighted illustration of a futuristic system for endovascular interventions.

4.2.1 Related Work - Guiding Endovascular Procedures

An approach to overcome the current disadvantages of EVAR procedures is to combine Intravascular Ultrasound (IVUS) and EM tracking [99–101]. In these studies, the combination of an IVUS system, which yields inner cross-sectional 2D images of the aorta, and the pose of the IVUS probe from an attached EM sensor allowed the reconstruction of the 3D aortic model. An additional EM sensor at the catheter (used for placing the stent graft) provided navigation within the aortic model [102]. In [100], an optical shape sensor based on Fibre Bragg Gratings (FBGs) was also included to obtain the catheter shape. No accuracy evaluation of the combined setup took place. Sieren et al. [103] proposed the combination of FBGs and preoperative CT scans to visualize the stent graft shape within a virtual 3D model of the aorta. Other studies suggested the combination of EM tracking systems and preoperative CT scans [104–106]. A registration of the EM coordinate system and the CT coordinate system with an EM sensor attached to the catheter allowed for a radiation-sparing guidance, including 3D information. Notwithstanding, an intraoperative imaging modality (for example, IVUS or Optical Coherence Tomography (OCT)) is necessary to update the preoperative CT images to the current patient's anatomy. Prior studies have already proposed the generation of VA images based on CT data [107, 108] for diagnostic purposes. Due to the intended purpose, however, the images were not generated and displayed in real-time, which is necessary for image guidance tasks.

As in the aforementioned studies, the approach of this work includes the use of an EM tracking system for guiding the catheter tip using preoperative CT scans. The novelty of this system – in contrast to previous studies – lies in the intuitive visualization of the tracked catheter tip and the aorta using HoloLens with additional guidance by means of a VA. Accordingly, the HMD is used to render the navigation data (namely the 3D aortic model including the catheter, orthogonal views of the preoperative CT scan, and VA images built from this scan) in the real environment.

4.2.2 Catheter Tip Tracking and Virtual Angioscopy Visualization

The tip of a custom-made 9 F catheter (FT030, Thorlabs GmbH) is tracked with the Aurora EM tracking system (Northern Digital Inc.), specifically with the Tabletop Field Generator (Figure 4.12) and an EM sensor (Aurora Mini 6 DOF) inside the catheter being close to the catheter tip. The EM field generator has a thin barrier to minimize tracking distortions caused by ferromagnetic materials located below it, making it suitable for being placed on a patient table. The device has an oval-shaped cylindrical measurement volume of 420 x 600 x 400 mm. The EM sensor has a length of 9 mm, a diameter of 1.8 mm and is preferable over the 5 DOF version as the former additionally provides the rotation along its longitudinal axis and shows a lower root mean square position error than the latter [109].

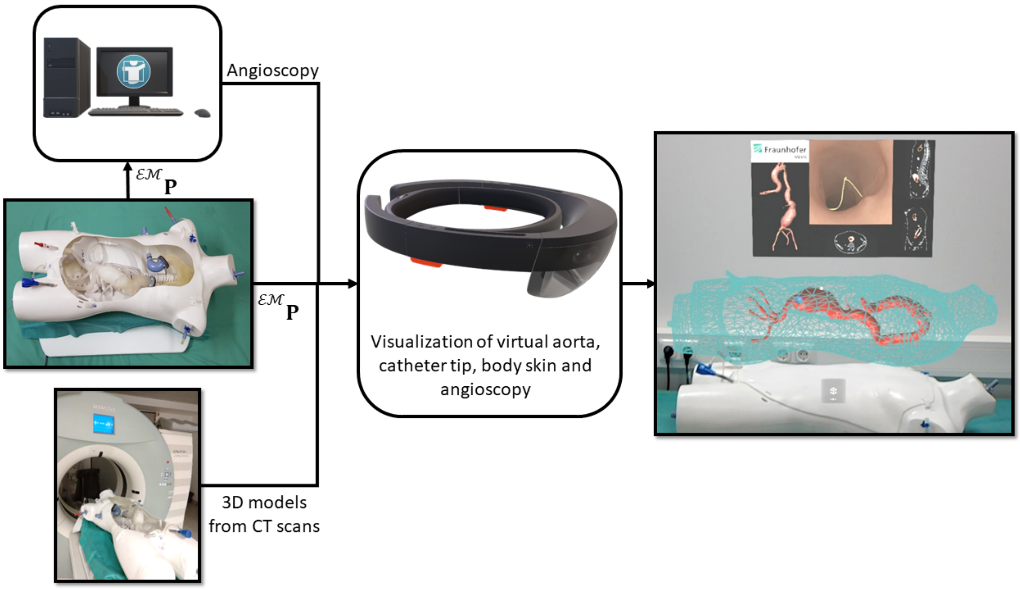

Figure 4.12: The connectors at the groins of the torso model (left middle image) facilitate the insertion of the catheter, including an EM sensor. A landmark-based registration provides the transformation matrix ${}^{\mathcal{EM}}\mathbf{T}_{\mathcal{CT}}$ from the EM coordinate system to the CT coordinate system. A CT scan of the model (left bottom image) allows for generating 3D models. EM sensor poses are sent to a computer (left top image) and to HoloLens and transformed to the CT coordinate system (center image). 3D models and a 2D panel with the VA image are displayed above the torso model (right image, phantom with top cover).

The position of the catheter tip in the EM coordinate system is converted into the CT coordinate system to visualize the catheter tip in the preoperative CT scan and within the 3D aortic model. A landmark-based registration [41] provides the transformation matrix ${}^{\mathcal{EM}}\mathbf{T}_{\mathcal{CT}}$, which describes the transformation from the EM coordinate system to the CT coordinate system. The registration is based on the position of several fiducial radiopaque markers placed around the area of interest in both coordinate systems. The coordinates of each marker in the EM coordinate system are gathered with the tip of an EM tracked and pivot calibrated pointer.

A Universal Windows Platform (UWP) application was developed for HoloLens 1[1] using Unity 2018.2.8f1 to render the 3D models of the aorta (virtual aorta), the catheter tip, the body surface (virtual body surface), and a 2D panel that includes the aortic model, the orthogonal views of the CT scan and the VA image (Figure 4.12). The 3D models of the aorta and body surface are created using MeVisLab (MeVis Medical Solutions AG and Fraunhofer MEVIS) after segmenting these structures in the preoperative CT scan. Every pose-dependent virtual angioscopy image reflects the point-of-view of the catheter tip within the vessel. It is created at runtime in MeVisLab using the Open Inventor library [110] from the aorta segmentation of a previous CT scan and the appearance is based on ex vivo and in vivo angioscopies [111, 112].

The current position of the catheter tip within the virtual aorta and its corresponding VA image are displayed on the HoloLens as follows: A middleware system sends the current position of the EM sensor inside the catheter to the AR glasses via Wi-Fi. After transforming the position to the CT coordinate system by applying ${}^{\mathcal{CT}}\mathbf{T}_{\mathcal{EM}}$, the catheter tip is displayed as a virtual sphere within the aortic model. At the same time and when requested by HoloLens, the last encoded virtual angioscopy image is sent from MeVisLab to the AR glasses via Wi-Fi using a remote procedure call (gRPC) [113]. Accordingly, in MeVisLab, the thread of image generation and encoding and the thread of image transmission run asynchronously. On HoloLens, the image is decoded after transmission and displayed on a virtual 2D canvas within the application (Figure 4.13).

---

[1] At the time of this work, HoloLens 2 was not yet available, which is why the first version was used. It can be assumed that the application can be developed for HoloLens 2 without any further problems.

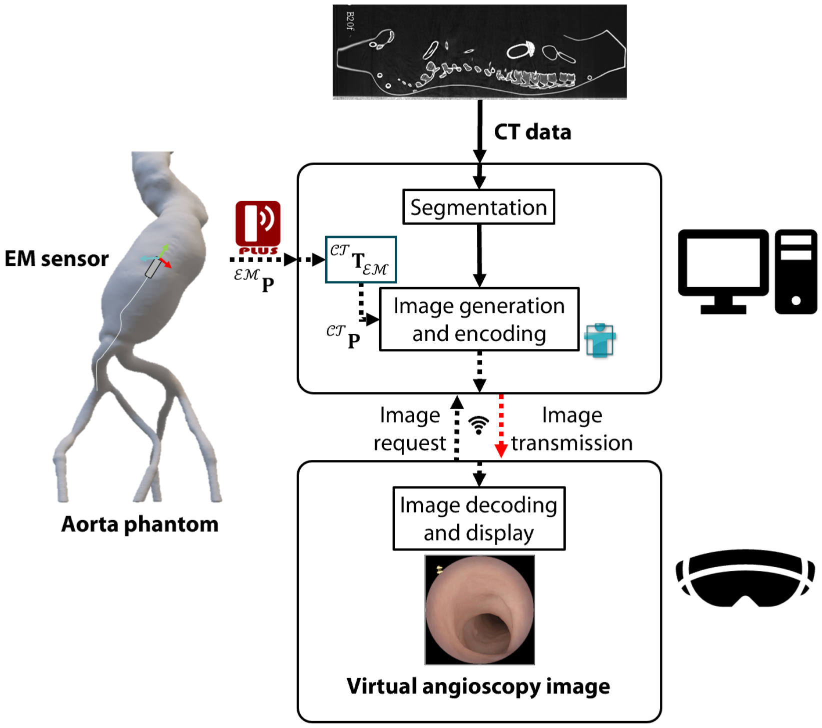

Figure 4.13: The EM sensor pose ${}^{\mathcal{EM}}\mathbf{P}$ in the aorta phantom was sent to MeVisLab and transformed to the CT coordinate system (${}^{\mathcal{CT}}\mathbf{P}$) by applying ${}^{\mathcal{CT}}\mathbf{T}_{\mathcal{EM}}$. In MeVisLab, the aorta was segmented using the CT data. Based on the pose ${}^{\mathcal{CT}}\mathbf{P}$ sent via PLUS and the segmented aorta, a virtual angioscopy image was created. Dotted lines indicate continuous data flow, while solid lines show a single data input. The red line shows the critical path of data flow as the largest amount of data is transmitted via Wi-Fi to HoloLens.

4.2.3 Evaluating Tracking Accuracy and Latency

Pointer Error

The accuracy of the tracked pointer used to acquire the marker positions was assessed using a precision-machined measurement plate similar to that described in [114]. The 6 DOF EM sensor was firmly attached to the pointer (Figure 4.14(b)), and pivot calibration was carried out using the NDI 6D Architect Version 3 to obtain the tip position and not the sensor position with the EM tracking system. Figure 4.14(a) shows the polyacetal measurement plate manufactured using a computer numerical control mill. The quadratic plate (20 mm thick and 350 mm length) included 6 × 6 holes (1.1 mm diameter and 3 mm depth) drilled row- and column-wise with a uniform distance of 50 mm. The plate was placed on top of the EM field generator with the required offset of 120 mm. The pointer (0.98 mm diameter and 3 mm length) was placed within each hole (Fig 4.14(c)), and 500 consecutive measurements were taken to calculate the mean position of each hole. The position of the four corner holes was used for a landmark-based registration to convert EM coordinates into the coordinates of the measurement plate (physical coordinates). Hereafter, the transformation matrix was applied to the coordinates of the four landmarks and the remaining 32 holes to calculate the Fiducial Registration Error (FRE) and the pointer error, respectively. FRE is the residual distance between the transformed and physical positions of the landmarks. On the other hand, the pointer error is the residual distance between the transformed and physical positions of the 32 holes.

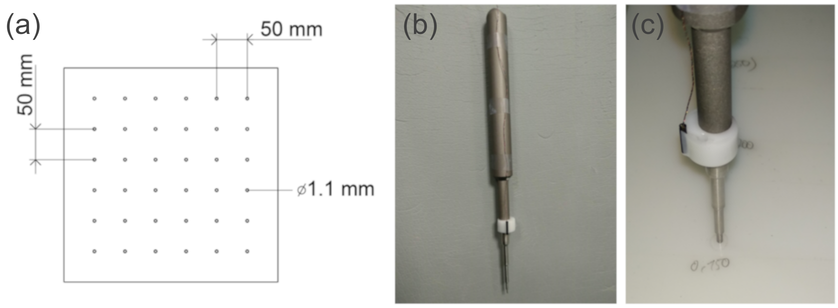

Figure 4.14: Setup for evaluating the pointer error. (a) Measurement plate. (b) Pointer and its attached EM sensor. (c) The pointer tip placed inside a hole of the measurement plate.

Marker Evaluation and Catheter Tip Error

The catheter tip accuracy was assessed with a torso model that included vascular structures. This phantom consisted of a body surface, a patient-specific aortic model, the spine from the thoracic vertebra IV until the coccyx, the pelvis and several connectors to build up a circulatory system (Figure 4.15(a)) [115]. The pathological aortic model and bones were generated from preoperative CT scans of a patient with aortoiliac aneurysm disease. The abdominal part of the aortic model and the bones were 3D printed using silicone and polylactic acid, respectively. Two entry points at the groin allow inserting a catheter.

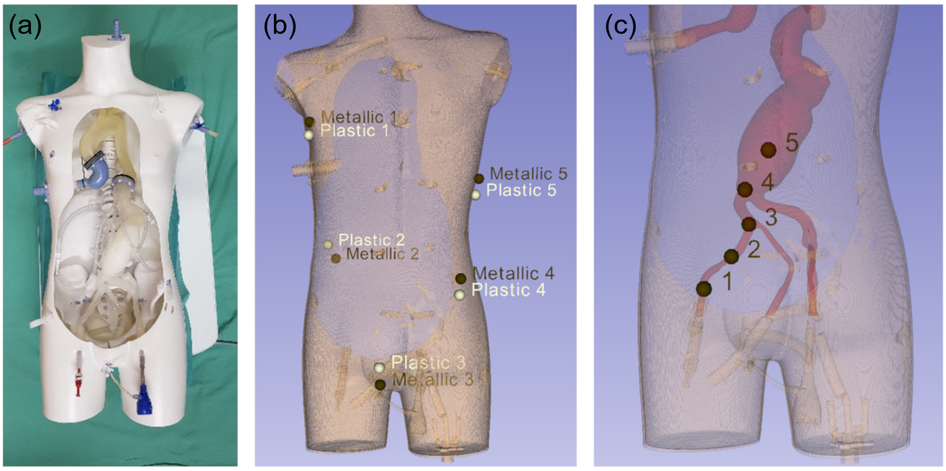

Figure 4.15: Setup for evaluating the catheter error. (a) Torso model. (b) Position of the fiducial markers on the body surface. (c) Measurement points of the catheter tip within the aorta

In this study, two different types of fiducial radiopaque markers were evaluated as landmarks for calculating ${}^{\mathcal{EM}}\mathbf{T}_{\mathcal{CT}}$ (Figure 4.16). On the one hand, commercially available lead balls with a diameter of 1 mm (SL-10, Suremark, AZ, USA – referred hereafter to as "metallic marker"). The limitation of these markers is that the pointer tip could easily slide on their surface when acquiring their position with the EM tracking system. On the other hand, hollow cylinders made from polyacetal with an inner diameter of 1 mm, an outer diameter of 8 mm and a height of 3 mm (referred hereafter to as "plastic marker"). The latter had the negative geometrical shape of the pointer tip to ensure a more stable tip placement. Five markers of each type were placed on the phantom surface around the area of interest, more precisely the aorta (Figure 4.15(b)). Below the plastic markers, a small point was drawn before attaching them to the phantom to enable reattachment by looking through the hollow cylinder. The small points simulated skin marking (for example, a tattoo) as used in radiotherapy [22].

The torso model was fixed with the required offset above the EM field generator, on the CT table of a Siemens SOMATOM Definition AS+ scanner. The position of each plastic marker was acquired with the pointer three times in order to check the repeatability when reattaching the marker after each repetition according to the

Figure 4.16: Plastic marker (top) and metallic marker (bottom)

drawn point. The coordinates of each marker corresponded to the mean value of 500 consecutive measurements with the EM tracking system. After that, a CT scan of the torso model, including the markers, was performed. This and the following CT scans were obtained using the same bed origin, slice thickness of 0.6 mm, pixel spacing of 0.86 mm, voltage of 120 kVp and exposure of 210 mAs. Afterwards, the positions in the EM coordinate system of both marker types were gathered three times in the EM coordinate system to check the repeatability without moving any marker. Another CT scan was carried out afterwards to ensure that the phantom did not move while obtaining the marker positions with the pointer tip. After that, the catheter, including the 6 DOF EM sensor at its tip, was then inserted into the right femoral artery. The catheter accuracy was assessed at five different positions along the abdominal aorta (Figure 4.15(c)) as follows. At each catheter position, the sensor coordinates were acquired with the EM tracking system. Afterwards, a CT scan was carried out to obtain the sensor position in the CT coordinate system as a ground truth. The sensor position in the EM coordinate system was performed again after the CT scan to ensure that the sensor did not move during the CT acquisition. Regarding the CT scans, the coordinates of each metallic marker were determined by segmenting it with a region growing method and calculating its centroid. The coordinates of each plastic marker were manually selected by choosing the hollow center close to the phantom surface. ${}^{\mathcal{EM}}\mathbf{T}_{\mathcal{CT}}$ was calculated using the positions of each type of marker in the EM coordinate system (first repetition) and the CT coordinate system. The FRE was calculated after transforming the marker positions in the EM coordinate system. The sensor position within the catheter was obtained in the CT scan by calculating its centroid in the closest slice to that in which the cables that connected the sensor with the EM tracking system were visible. The five sensor positions in the CT coordinate system and their corresponding transformed positions in the EM coordinate system were then used to calculate the error of the catheter tip.

Latency of Virtual Angioscopy Images

The computer and HoloLens were connected using the wireless dual band gigabit router TP-Link AC 1750 via Ethernet and Wi-Fi, respectively. The wireless mode 802.11ac, 5 GHz band and 80 MHz channel bandwidth were selected to optimize data transfer speed. For latency comparison, two different image compression formats were evaluated (JPEG (80 % quality) and DXT1). The latency of transmitting and displaying virtual angioscopy images on HoloLens was assessed by measuring the interval between requesting a virtual angioscopy image (matrix size 512 × 512, 24 bits per pixel) from MeVisLab until displaying it on HoloLens using timestamps. This process was repeated for one minute for images of both formats.

4.2.4 Tracking Results and Latencies

Pointer Error

The FRE using the four corner holes of the measurement plate was 0.21 mm. The pointer error of the remaining 32 holes was 0.62 ± 0.25 mm (mean ± Standard Deviation (SD)).

Marker Evaluation

Regarding the repeatability after reattaching the plastic markers, the distance between their positions was 0.65 ± 0.24 mm (mean ± SD) with a minimum and maximum distance of 0.23 and 1.03 mm, respectively. On the other hand, the distance without detaching the plastic markers was 0.53 ± 0.18 mm (minimum 0.25 mm and maximum 0.79 mm). Even though the plastic markers were removed, the mean value, SD, minimum and maximum differed less than 0.25 mm compared to the undetached case. No statistical difference was found (Student's t-test, paired sample). Regarding the metallic markers, the distance between their positions was 0.64 ± 0.52 mm with a minimum distance of 0.10 mm and a maximum distance of 1.45 mm. No statistical difference was found when comparing both types of markers without moving them (Student's t-test, paired sample). The SD of the distances measured for the metallic markers was more than double regarding both measurements for the plastic markers. Additionally, the maximum distance for the metallic markers was 0.4 mm higher than that obtained for the detached plastic markers. The maximum distance of the metallic markers between both CT scans was 0.13 mm.

Catheter Error

The maximum distance of the catheter sensor between the EM measurement before and after the CT scan was 0.28 mm, proving that no unintended movement happened. On the other hand, the maximum distance of the metallic markers was 0.31 mm across all experiments compared to the first CT scan. For the end-to-end error, the FRE and the catheter error were calculated for both the metallic and the plastic markers. The FRE was 2.59 ± 1.49 mm (mean ± SD) for the metallic markers and 2.99 ± 1.26 mm for the plastic markers. The mean and SD of the catheter error (Table 4.4) between the two different markers showed a difference of around 0.2 mm. The catheter error of the second position was more than 1 mm lower for the setup with the plastic markers and only one value exceeded 2 mm for the plastic markers (first position). Low errors can be found in both setups for the fourth position (around 0.5 mm). The student's t-test showed no statistical difference between both markers for the catheter error.

Table 4.4: Catheter error for the different catheter positions within the aorta.

Catheter error [mm]	Catheter position					Mean ± SD
	1	2	3	4	5	
Metallic markers	2.34	2.56	1.55	0.54	1.02	1.60 ± 0.86
Plastic markers	2.11	1.51	1.18	0.50	1.59	1.38 ± 0.59

Latency of Virtual Angioscopy Images

The proposed system was capable of generating and streaming the VA images corresponding to the catheter tip pose to HoloLens (Figure 4.17). User interaction based on hand gestures allowed the placement of the virtual 2D canvas anywhere in the real world. Table 4.5 shows the results of the latency measurements. The DXT1 format leads to a latency reduction of 87 %. While the request and image transmission times are similar for both formats, the decoding and display intervals are around 20 times shorter for images encoded with the DXT1 format. The mean encoding time in MeVisLab was 4 ms for the JPEG compression (129 measurements) and 20 ms for the DXT1 compression (136 measurements). The image quality for both approaches appeared to be similar after decoding and displaying on HoloLens.

4.2.5 Discussion

This study presented a system that included a catheter with an attached EM sensor and HoloLens to display navigation data such as 3D models and VA images based

Table 4.5: Results of the latency measurements for two different compression formats.

Latency in ms (Mean ± SD)	JPEG	DXT1
Request and image transmission	10 ± 3	8 ± 7
Decoding and display	72 ± 3	3 ± 1
Total	82 ± 4	11 ± 7

Figure 4.17: The virtual body surface (turquoise wireframe), aorta (red), catheter tip (blue sphere) and 2D panel above the torso model (white phantom without its top cover). This 2D panel displayed the aortic model, the VA image with its centerline (yellow) and the orthogonal views of the preoperative CT scan corresponding to the current position of the catheter tip (red sphere).

on preoperative CT scans for 3D guidance during EVAR procedures.

The goal of the first experiment was to obtain the pointer error since this factor may influence the following measurements. The results with the measurement plate showed an acceptable pointer error compared with the accuracy of 0.80 mm provided by the manufacturer for this sensor in combination with the used field generator. The key-lock principle for the pointer and the holes ensured a precise placement of the tip on the target. Even though this experiment was performed in 3D space, not the entire EM working volume was evaluated, and the measurement plate was placed close to the field generator. According to data provided by the manufacturer, the position error increases with the distance of the EM sensor from the center of the EM field generator. The repeatability measurements regarding the plastic markers showed similar distances with and without detaching the markers. Thus, placing the plastic markers in a similar position after removing them, as done in radiotherapy, seems to provide similar accuracy. On the other hand, even though the mean distance regarding the metallic markers was similar to that of the plastic markers, the SD was twice as high. This might be related to the fact that the lead ball does not allow the placement of the pointer tip in the same fixed position as the plastic marker's hollow cylinder does. Therefore, it is recommended to use a similar marker, as the plastic markers can be reattached and present a lower SD compared to the metallic markers.

The catheter tip error was assessed in an end-to-end experiment with a torso model. The low maximum distance of the metallic markers and EM sensor indicate that the experimental setup was stable. The FRE was almost twice as high as the catheter error. Nevertheless, it is important to be aware that both measures are related but not correlated [116]. One potential reason for the higher FRE was that the markers and, accordingly, the sensor attached to the pointer were close to the edges of the EM working volume and thus in an area with higher error. An initial study with a similar setup evaluated the general acceptance among clinicians and showed satisfying results [50]. The catheter tip error was comparable to other previous studies [104–106]. Even though the presented setup contained a non-rigid aorta, the catheter error was measured relative to the firm body surface – similar to the rigid setups in previous studies. In [104], a reference plate was used for a manual registration. Accordingly, the relative pose between plate and body must be the same during and after the CT acquisition. Additionally, the manual registration is a user-dependent process. In [105], the authors proposed a path-based registration. The path of the EM sensor inside the left and right aortoiliac branches was tracked and registered to the lumen of the aorta extracted from CT scans. This seems to be a practical solution, as no landmarks are necessary. However, fluoroscopy is needed to safely obtain the trajectory paths in a clinical setting. In [106], the authors used a calibration phantom with holes to accommodate the EM sensor in order to obtain two point clouds for the rigid registration. Nevertheless, the 3D models were obtained with a C-arm, which provided a smaller field of view. When compared to these three studies, this setup provides a larger working volume, an intuitive 3D visualization with HoloLens and allows reattaching the markers when the intervention is not performed after the CT acquisition. Nevertheless, this initial study evaluated the accuracy of the EM tracking without considering anatomical deformations (for example, due to the pulsation of arterial vessels) that occur in a real-life scenario. Future work should therefore focus on intraoperative imaging techniques, such as intravascular ultrasound, for updating the current anatomy [99] using a non-linear optimization framework that does not depend on any prior knowledge of ${}^{\mathcal{EM}}\mathbf{T}_{\mathcal{CT}}$.

The pose-dependent VA, including corresponding CT slices, may add valuable additional information for navigation in radiation-sparing EVAR procedure approaches. The feasibility of the workflow as shown in Figure 4.13 was proven. Nevertheless, a direct visual comparison with a real angioscopy of that specific aorta is not possible. However, García-Vázquez et al. [117] compared the generated images with images from a VGA camera inside a 3D printed aorta. They conclude that similar images of the vessel were acquired in both cases except for the different perceived depths. Additionally, small differences can be identified, probably due to the lumen segmentation. The latency measurements suggest using the DXT1 format for HoloLens, as the decoding and displaying time is clearly shorter than using the JPEG format. This is due to the fact that DXT1 is directly supported by the graphics processing unit – unlike JPEG. The end-to-end latency was not evaluated in this study as image generation and encoding, on the one hand, and transmission, decoding and display, on the other hand, run independently. Nevertheless, the end-to-end latency can be assumed to be lower for the DXT1 compression since the sum of encoding, decoding and display time is still around three times faster and the transmission time is in the same range for both image formats.

4.2.6 Section Summary

To create an AR environment for radiation-free endovascular interventions, it is necessary to merge the virtual 3D models with the spatially tracked instruments into a common coordinate system. Furthermore, the question is how to track the tools without line-of-sight. These issues are reflected in **RQ4** and have been addressed in this section.

The developed system enables tracking of endovascular instruments by EM tracking and intuitive hands-free visualization with HoloLens. An in-depth evaluation of the tracking accuracy, including landmark-based registration, showed promising results. In this context, landmarks were presented that can be removed and re-applied, which is especially necessary for pre-interventional image acquisition. A major limitation of this study is the rigid setup. Future research should therefore focus primarily on non-rigid approaches. The system provides additional navigation through position-dependent VA images. Here, minimal latency could be achieved by choosing the appropriate image format.

This section concludes the systems presented in the context of the workflow for vascular diagnosis and intervention. Another component, which is not covered in this thesis, are systems for assessing successful treatment in the post-interventional setup.

5 Conclusions, Challenges & Outlook

With 46 % of fatalities for women and 39 % of deaths for men, CVD represent the most common cause of death in Europe. Diagnostic and interventional approaches that are easy-to-use, safe and accurate are therefore of high interest. Many of the current diagnostic and interventional approaches rely on X-ray imaging with ionizing radiation to classify pathologies, create a 'roadmap', and navigate endovascular instrumentation. In contrast, US is a safe, inexpensive, and often available imaging modality, but requires an experienced physician, does not create a 'roadmap', and continues to suffer from artifacts. For endovascular interventions, the problem of spatial tracking of instruments remains unless fluoroscopy is used, which in turn uses carcinogenic X-rays.

In this work, several AR-based applications were presented to facilitate vascular diagnostics and interventions – always with a focus on avoiding or at least reducing the use of carcinogenic X-rays and nephrotoxic contrast agents. The use of the AR HMDs device HoloLens served primarily the purpose of intuitive visualization. However, the HoloLens integrated camera systems were also used for novel tracking approaches, which are necessary in many applications. The objectives of this thesis, summarized in four research questions, have been addressed in the previous chapters, with promising results highlighting the great potential of AR and US for vascular diagnostics and interventions.

RQ1 How can the probe be tracked with minimal technical complexity, and how accurate is the tracking?

In this work, a novel approach is described to track US probes using HoloLens 2 which itself displays live ultrasound images in-situ on the imaged anatomy. The approach uses retroreflective spheres attached to the US probe and tracks them using the infrared light-based depth camera integrated into the AR HMD, eliminating the need for an external tracking system. A Kalman filter is implemented to improve tracking accuracy. The dynamic tracking error of 2.81 mm is promising, and the latency of displayed images is minimal, allowing for real-time perception for the sonographer. This approach is a cheap and easy-to-use alternative to traditional tracking systems for AR-assisted US examinations. The open-source application may help sonographers learn and perform US-based vascular diagnostics more effectively by providing an intuitive and ergonomically friendly in-situ visualization of the 2D US image.

RQ2 How can arteries reliably be segmented in US images, and what accuracy is achieved?

To answer this question, this segmentation task was carried out by different variations of a state-of-the-art deep learning approach to provide physicians with a reliable indication of the artery's location and size, streamlining the diagnostic process. The performance of different segmentation approaches was evaluated by comparing their segmentations to the manual ground truth through calculating the Dice score. The resulting scores were 0.633, 0.725, and 0.819 for the U-Net Concatenated Input, U-Net Concatenated Bottleneck and U-Net Baseline, respectively. The U-Net Baseline outperformed the other approaches with a Dice score of 0.819. The segmentation network was trained and tested on US images of the femoral artery in healthy volunteers, demonstrating its feasibility on realistic images. In addition to facilitating diameter measurements, the segmentation also simplifies the differentiation between the femoral artery and vein within the image. It is worth noting that the lack of feasibility testing for abdominal aortas is a limitation of this work; however, it is believed that this approach can also be applied to this anatomy.

RQ3 Is it possible to provide a target frame rate of 60 Hz when rendering US volumes on a stand-alone AR device? Can the system achieve a latency close to real-time perception?

The proposed system employs a remote rendering approach, and the technical evaluation has indicated that this solution provides adequate computational power to achieve a sufficiently high frame rate with minimal latency. The HRM thus allows the volume rendering to be executed on a powerful workstation and further enables data transfer of the volumes from the US station to this very computer via Ethernet cable and accordingly a very high transfer rate. Additionally, the experiments have demonstrated that this approach may confer advantages over viewing 2D US images in AR for US-guided tasks, such as reducing task completion time. However, a significant limitation of the technology is its inability to separate pertinent structures from noise and occlusion. Nevertheless, when target structures are readily distinguishable, AR HMDs provide a vivid spatial visualization of real-time 3D US. As a result, it may be argued that future research should strive to overcome visual occlusion issues so that this technology can be evaluated in more practical contexts.

RQ4 How can we register the vascular 3D model with the tracked endovascular tools for a combined visualization? Which tracking approach can be utilized for this kind of intervention, and what accuracy is achievable?

The system that has been developed facilitates the tracking of endovascular instruments through the use of electromagnetic (EM) tracking and provides an intuitive, hands-free visualization experience via HoloLens. An in-depth evaluation of the tracking accuracy, which involved landmark-based registration, has demonstrated promising results. Landmarks were identified and presented that can be removed and reapplied as needed, particularly during preinterventional image acquisition. A major limitation of this study is the rigidity of the setup. As such, future research should prioritize the exploration of non-rigid approaches. By choosing the right image format, the system also enables navigation through pose-dependent VA images with a minimum of latency.

In Chapter 1, based on the elaborated disadvantages of current diagnostics and interventions, realistic and achievable approaches to the ideal systems were presented. Figure 5.1 shows these initial ideas and juxtaposes them illustratively with the systems developed in this thesis.

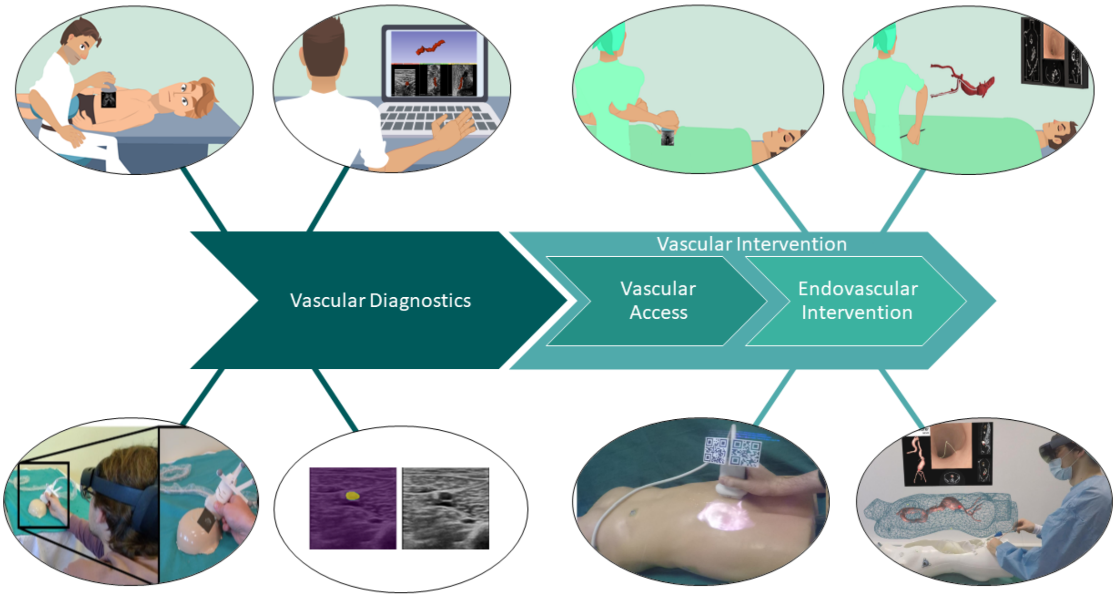

Figure 5.1: The workflow of vascular diagnostics and interventions, with illustrations of the initial ideas (top row) and pictures of the actual developed systems (bottom row).

Challenges

In the previous chapters, AR applications have been presented that can support both vascular diagnostics and interventions. Nevertheless, there are still some challenges that should be addressed in the coming years to enable widespread use of the presented applications. These will be briefly presented and discussed in the following.

AR HMDs are seminal devices for AR-guided medical applications as they allow hands-free interaction, give a 3D impression of virtual objects through stereoscopic displays and enable a variety of useful features through the built-in camera systems (tracking, workflow analysis, remote assistance, etc.). However, these devices still have disadvantages that need to be overcome in order to be widely used. With 2-3 hours of battery life, the HoloLens 2 is not yet mature enough for longer use in the daily clinical routine of physicians. The interaction with virtual objects with

HoloLens 2 is based on hand gestures. This kind of interaction is generally new to most users – even though gestures for translation and rotation are relatively intuitive. Balani et al. [118] investigated the usability of interactions between different devices, such as HoloLens 2, VR glasses and an AR smartphone. They conclude that, in comparison to the familiar touch screen based AR interaction, the free-hand AR interaction posed a challenge for participants. They observed that users found the HoloLens 2 hand tracking interaction overwhelming and difficult to use, which could explain the lower scores in terms of perspicuity and dependability for the HoloLens 2. Therefore, one can argue that until AR HMDs are widely used, a proper introduction to the interactions used is needed. Lastly, OST HMDs such as HoloLens provide an unobstructed view of the real world and thus perfect image quality without latency. However, this usually comes with a limited FOV for the virtual objects within the real world. This limitation is commonly mentioned [119] and should be improved in future iterations of these devices.

For this work, Philips provided a research interface through which US images and volumes could be streamed to a workstation or HoloLens. While this is sufficient in these cases, it would be useful to have a common and open interface for all US stations. Indeed, a capture card does enable streaming the screen output, but usually comes with an image quality loss and requires post processing techniques to select the region of interest and read image parameters like imaging depth. Furthermore, the transmission of 3D US data via a capture card is not possible and therefore not an option for future 3D US AR applications.

Spatial tracking of medical instruments and the US probe is an essential part of IGT applications. In this work, a novel approach was presented that tracks retroreflective spheres using only the HoloLens' integrated camera systems. Although this methodology is a significant improvement in terms of technical effort compared to external OTS, the attached spheres lead to a rather clumsy handling. In this context, it would make sense to explore other tracking options. One possibility are potentially retroreflective stripes that are attached to the surface of the probe and can still be tracked with the camera systems. Another option are sophisticated computer vision methods that use RGB images to estimate the position and orientation of an object [120].

In Section 4.1, it was shown that 3D US with AR HMDs is a promising combination for IGT applications. Real-time volumetric imaging of moving anatomical structures, including medical instruments, with a stereoscopic display provides a unique opportunity to perform motion compensation during the procedure without moving the transducer. In addition, US remains a safe and radiation-free imaging technique. However, the difficulty in distinguishing relevant structures from noise and occlusion has been identified as an unresolved limitation. Therefore, the challenge here is to develop appropriate methods that automatically segment the anatomies to be examined and/or render the volume in such a way that the region of interest is appropriately visualized and not obscured.

Section 4.2 presented an initial system for facilitating radiation-free endovascular intervention. This first approach used landmark-based registration for the rigid 3D model of the aorta. Since some time may elapse between preoperative CT and intervention and the pulsation of the artery is not negligible, the challenge in the future is to adopt a non-rigid registration approach. Furthermore, with an intraoperative imaging modality, the anatomy should be updated as regularly as possible. Shi et al. [100] proposed such a method for vasculature reconstruction and catheter modeling using IVUS imaging, EM tracking, and shape sensing. The system involves using an IVUS probe to obtain inner cross-sectional images of the aorta, fusing this information with pose data from an EM sensor to construct a 3D virtual model of the aorta, and reconstructing the catheter shape using optical fibers with FBGs. The method was tested on in-vitro silicone aortic phantoms using a hybrid probe consisting of an IVUS sensor, an EM sensor, and an optical shape sensor.

Potentials

In recent years, many large tech companies have entered the field of mixed reality (Qualcomm, Meta, Apple etc.) and this trend will continue – also in the healthcare sector (Figure 5.2). The investment power and thus the progress of research and development in this area are correspondingly high. We will probably experience mixed reality in the future in ways we cannot currently imagine. But there are now a lot of impending technological advancements to look forward to. There will be HMD technology that is quicker, lighter, and more inexpensive. 5G wireless networks will also play an important role when it comes to remote rendering setups. Two famous examples of the built-in technologies that will be added to HMDs more frequently are hand detection and eye tracking. Users may be more expressive and engage with their mixed reality experience more deeply thanks to hand detection, which enables users to direct movements without bulky controllers. The system can concentrate the best resolution and image quality solely on the areas of the image that the user is actually looking at thanks to the use of eye-tracking technology. It is possible that mixed reality technologies will start to connect more naturally with the human body. Contact lenses with microLEDs to produce an AR environment are one method (Mojo Lens, Mojo Vision) that brings the initial idea of X-ray vision (Figure 1.3) closer to reality. In the context of this work, the mentioned future developments mean that, above all, the user-friendliness of the HMD devices for the clinic staff is increased, and thus longer wearing times become possible. If the devices are small and light enough, offer access to relevant clinical information and are easy to use, it is conceivable that doctors will wear them during their entire working hours – similar to their stethoscope. For vascular diagnostics and intervention, 3D perception using the stereoscopic display and hand gestures for interaction offers a meaningful and intuitive representation for facilitated procedures.

With the help of cutting-edge matrix-array probes, US can be used to acquire volumetric image data with large FOVs in real-time without the use of ionizing radiation. Ideally, the previously mentioned interface also provides access to DUS images

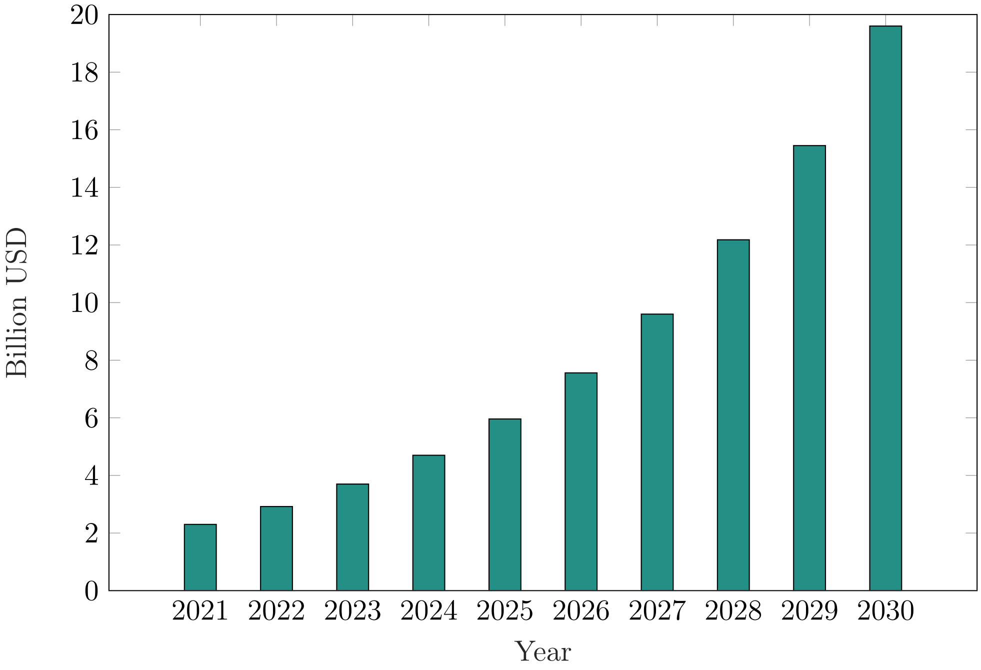

Figure 5.2: The global AR and VR market size in the healthcare sector and its forecast until 2030 [121].

which could greatly improve AR-based US vascular diagnostics. Access to DUS images is not even available through the Philips research interface. Furthermore, 3D DUS volumes in combination with sophisticated volume rendering techniques and AR could present a unique imaging modality and visualization as the physician is provided with a real-time volumetric image of the vessels, including hemodynamic information. The information content of these images is important for diagnostics as well as interventions. While information about the severity of the stenosis can be obtained during diagnosis, successful stent placement and endoleaks can be determined during intervention.

In this work, the AR system facilitated endovascular interventions by simply showing the catheter tip within the 3D model of the aorta. In recent years, FBGs have emerged to a seminal technology for shape sensing. The AR guidance system could be improved if not only the tip of the catheter but the whole shape is displayed within the aorta – also to potentially update the aorta shape. This technology was investigated and evaluated by several researchers [103, 122]. The Philips-developed Fiber Optic RealShape technology, however, is the most advanced system [123]. A clinical study with 50 patients proved shorter catheterization times and lower radiation exposure [124].

Conclusion

In conclusion, this work has demonstrated the potential of AR-facilitated vascular diagnostics and interventions. With the high incidence of CVD, the need for safe, accurate and easy-to-use diagnostic and interventional approaches is crucial. The use of AR-based applications, such as the HoloLens, has shown promising results in facilitating vascular diagnostics and interventions while avoiding the use of carcinogenic X-rays and nephrotoxic contrast agents. This thesis has addressed four research questions related to probe tracking, artery segmentation, real-time volume rendering, and endovascular tool tracking, with results demonstrating the feasibility and accuracy of these approaches. However, limitations remain, and future research should strive to overcome visual occlusion issues, rigid registrations and anatomy limitations. Further, the technology should be evaluated in more practical contexts. Overall, this thesis highlights the potential for AR and US to revolutionize vascular diagnostics and interventions towards X-ray free approaches while providing Superman's X-ray vision.

Bibliography

[1] S. Factor, M. A. Lamberti-Abadi and J. Abadi, *Handbook of Pathology and Pathophysiology of Cardiovascular Disease*, 1st ed., ser. Developments in Cardiovascular Medicine 240. Springer US, 2002, ISBN: 9780792375425.

[2] L. M. Buja and J. Butany, *Cardiovascular Pathology*, Fifth Edition. Academic Press, 2022, ISBN: 978-0-12-822224-9. DOI: `https://doi.org/10.1016/B978-0-12-822224-9.00025-6`.

[3] N. Townsend, D. Kazakiewicz, F. Lucy Wright, A. Timmis, R. Huculeci, A. Torbica *et al.*, 'Epidemiology of cardiovascular disease in europe', *Nature Reviews Cardiology*, vol. 19, no. 2, pp. 133–143, 2022, ISSN: 1759-5010. DOI: `10.1038/s41569-021-00607-3`.

[4] G. Dhaliwal and D. Mukherjee, 'Peripheral arterial disease: Epidemiology, natural history, diagnosis and treatment', *International Journal of Angiology*, vol. 16, no. 2, pp. 36–44, 2007, ISSN: 10611711. DOI: `10.1055/s-0031-1278244`.

[5] T. Vos, C. Allen, M. Arora, R. M. Barber, A. Brown, A. Carter *et al.*, 'Global, regional, and national incidence, prevalence, and years lived with disability for 310 diseases and injuries, 1990–2015: a systematic analysis for the global burden of disease study 2015', *The Lancet*, vol. 388, no. 10053, pp. 1545–1602, 2016, ISSN: 1474547X. DOI: `10.1016/S0140-6736(16)31678-6`.

[6] M. A. Allison, E. Ho, J. O. Denenberg, R. D. Langer, A. B. Newman, R. R. Fabsitz *et al.*, 'Ethnic-specific prevalence of peripheral arterial disease in the united states', *American Journal of Preventive Medicine*, vol. 32, no. 4, pp. 328–333, Apr. 2007, ISSN: 0749-3797. DOI: `10.1016/j.amepre.2006.12.010`.

[7] K. Singh, K. H. Bønaa, B. K. Jacobsen, L. Bjørk and S. Solberg, 'Prevalence of and risk factors for abdominal aortic aneurysms in a population-based study : The tromsø study', *American Journal of Epidemiology*, vol. 154, no. 3, pp. 236–244, Aug. 2001, ISSN: 0002-9262. DOI: `10.1093/aje/154.3.236`.

[8] X. Li, G. Zhao, J. Zhang, Z. Duan and S. Xin, 'Prevalence and trends of the abdominal aortic aneurysms epidemic in general population - a meta-analysis', *PLOS ONE*, vol. 8, no. 12, pp. 1–11, 2013, ISSN: 19326203. DOI: `10.1371/journal.pone.0081260`.

[9] J. A. van der Vliet and A. P. M. Boll, 'Abdominal aortic aneurysm', *The Lancet*, vol. 349, no. 9055, pp. 863–866, Mar. 1997, ISSN: 0140-6736. DOI: `10.1016/S0140-6736(96)07282-0`.

[10] V. Aboyans, J.-B. Ricco, M.-L. E. L. Bartelink, M. Björck, M. Brodmann, T. Cohnert *et al.*, '2017 ESC guidelines on the diagnosis and treatment of peripheral arterial diseases, in collaboration with the European Society for Vascular Surgery (ESVS)', *European Journal of Vascular and Endovascular Surgery*, vol. 55, no. 3, pp. 305–368, Mar. 2018, ISSN: 1078-5884. DOI: `10.1016/j.ejvs.2017.07.018`.

[11] A. K. Thukkani and S. Kinlay, 'Endovascular intervention for peripheral artery disease', *Circulation Research*, vol. 116, no. 9, pp. 1599–1613, 2015. DOI: `10.1161/CIRCRESAHA.116.303503`.

[12] A. Wanhainen, F. Verzini, I. Van Herzeele, E. Allaire, M. Bown, T. Cohnert *et al.*, 'Editor's choice; European society for vascular surgery (ESVS) 2019 clinical practice guidelines on the management of abdominal aorto-iliac artery aneurysms', *European Journal of Vascular and Endovascular Surgery*, vol. 57, no. 1, pp. 8–93, Jan. 2019, ISSN: 1078-5884. DOI: `10.1016/j.ejvs.2018.09.020`.

[13] K. Evans, S. Roll and J. Baker, 'Work-related musculoskeletal disorders (WRMSD) among registered diagnostic medical sonographers and vascular technologists: A representative sample', *Journal of Diagnostic Medical Sonography*, vol. 25, no. 6, pp. 287–299, 2009, ISSN: 87564793. DOI: `10.1177/8756479309351748`.

[14] G. Harrison and A. Harris, 'Work-related musculoskeletal disorders in ultrasound: Can you reduce risk?', *Ultrasound*, vol. 23, no. 4, pp. 224–230, 2015. DOI: `10.1177/1742271X15593575`.

[15] S. Rogers, J. Carreira, R. Thompson, A. Morais, C. Miller, W. Wein *et al.*, 'An ex vivo evaluation of tomographic 3D ultrasound, B-Mode ultrasound, CT and MR imaging to measure artery diameter, length and wall volume', *Ultrasound in Medicine and Biology*, vol. 45, no. 10, pp. 2819–2829, 2019, ISSN: 1879291X. DOI: `10.1016/j.ultrasmedbio.2019.07.002`.

[16] F. A. Lederle, J. A. Freischlag, T. C. Kyriakides, J. S. Matsumura, F. T. Padberg, T. R. Kohler *et al.*, 'Long-term comparison of endovascular and open repair of abdominal aortic aneurysm', *New England Journal of Medicine*, vol. 367, no. 21, pp. 1988–1997, 2012, ISSN: 0028-4793. DOI: `10.1056/nejmoa1207481`.

[17] Q. H. Tang, J. Chen, C. F. Hu and X. L. Zhang, 'Comparison between endovascular and open surgery for the treatment of peripheral artery diseases: A meta-analysis', *Annals of Vascular Surgery*, vol. 62, pp. 484–495, Jan. 2020, ISSN: 0890-5096. DOI: `10.1016/J.AVSG.2019.06.039`.

[18] S. Bhatty, R. Cooke, R. Shetty and I. S. Jovin, 'Femoral vascular access-site complications in the cardiac catheterization laboratory: Diagnosis and management', *Interventional Cardiology*, vol. 3, no. 4, pp. 503–514, 2011, ISSN: 17555302. DOI: `10.2217/ICA.11.49`.

[19] S. Sorrentino, P. Nguyen, N. Salerno, A. Polimeni, J. Sabatino, A. Makris *et al.*, ‘Standard versus ultrasound-guided cannulation of the femoral artery in patients undergoing invasive procedures: A meta-analysis of randomized controlled trials’, *Journal of Clinical Medicine*, vol. 9, no. 3, 2020, ISSN: 2077-0383. DOI: 10.3390/jcm9030677.

[20] S. I. Seldinger, ‘Catheter replacement of the needle in percutaneous arteriography: A new technique’, *Acta Radiologica*, vol. 39, no. 5, pp. 368–376, 1953. DOI: 10.3109/00016925309136722.

[21] J. Schröder, *Trainer vaskuläre interventionen: 9 tabellen.* Stuttgart (Germany): Thieme, 2011, ISBN: 9783131532114. [Online]. Available: https://books.google.de/books?id=vU68ygAACAAJ.

[22] B. W. Ullery, R. L. Hallett and D. Fleischmann, ‘Epidemiology and contemporary management of abdominal aortic aneurysms’, *Abdominal Radiology*, vol. 43, no. 5, pp. 1032–1043, 2018, ISSN: 23660058. DOI: 10.1007/s00261-017-1450-7.

[23] A. Hertault, B. Maurel, J. Sobocinski, T. Martin Gonzalez, M. Le Roux, R. Azzaoui *et al.*, ‘Impact of hybrid rooms with image fusion on radiation exposure during endovascular aortic repair’, *European Journal of Vascular and Endovascular Surgery*, vol. 48, no. 4, pp. 382–390, Oct. 2014, ISSN: 1078-5884. DOI: 10.1016/J.EJVS.2014.05.026.

[24] A. Hertault, B. Maurel, M. Midulla, C. Bordier, L. Desponds, M. Saeed Kilani *et al.*, ‘Editor’s choice – minimizing radiation exposure during endovascular procedures: Basic knowledge, literature review, and reporting standards’, *European Journal of Vascular and Endovascular Surgery*, vol. 50, no. 1, pp. 21–36, Jul. 2015, ISSN: 1078-5884. DOI: 10.1016/J.EJVS.2015.01.014.

[25] R. Dörner, B. Jung, W. Broll and P. Grimm, *Virtual und augmented reality (VR / AR): grundlagen und methoden der virtuellen und augmentierten realität*, 1st ed. Vieweg+Teubner Verlag, 2013, ISBN: 978-3-642-28902-6.

[26] P. Milgram and F. Kishino, ‘A taxonomy of mixed reality visual displays’, *IEICE Transactions on Information and Systems*, vol. 77, no. 12, pp. 1321–1329, 1994.

[27] R. Skarbez, M. Smith and M. C. Whitton, ‘Revisiting Milgram and Kishino’s Reality-Virtuality Continuum’, *Frontiers in Virtual Reality*, vol. 2, no. April, 2021. DOI: 10.3389/frvir.2021.647997.

[28] M. Doughty, N. R. Ghugre and G. A. Wright, ‘Augmenting performance: A systematic review of optical see-through head-mounted displays in surgery’, *Journal of Imaging*, vol. 8, no. 7, 2022. DOI: 10.3390/jimaging8070203.

[29] C. Gsaxner, J. Li, A. Pepe, Y. Jin, J. Kleesiek, D. Schmalstieg *et al.*, ‘The holoLens in medicine: A systematic review and taxonomy’, *Medical Image Analysis*, vol. 85, p. 102 757, Apr. 2023, ISSN: 1361-8415. DOI: 10.1016/J.MEDIA.2023.102757.

[30] *Microsoft HoloLens 2: Improved Research Mode to facilitate computer vision research - Microsoft Research.* [Online]. Available: `https://www.microsoft.com/en-us/research/blog/microsoft-hololens-2-improved-research-mode-to-facilitate-computer-vision-research/` (visited on 16/01/2023).

[31] S. Park, S. Bokijonov and Y. Choi, 'Review of microsoft hololens applications over the past five years', *Applied Sciences*, vol. 11, no. 16, 2021, ISSN: 2076-3417. DOI: `10.3390/app11167259`.

[32] D. Ungureanu, F. Bogo, S. Galliani, P. Sama, X. Duan, C. Meekhof *et al.*, 'HoloLens 2 research mode as a tool for computer vision research', pp. 1–7, 2020. [Online]. Available: `http://arxiv.org/abs/2008.11239`.

[33] S. Delorme and J. Debus, *Sonografie*, ser. Duale Reihe. Thieme, 2012, ISBN: 9783131933133. [Online]. Available: `https://eref.thieme.de/ebooks/1775087#/ebook_1775087_SL70134602`.

[34] B. Widder and M. Goertler, *Doppler und duplexsonographie der hirnversorgenden arterien*, 6th ed. Springer Berlin Heidelberg, 2004. DOI: `10.1024/0301-1526.34.1.70a`.

[35] F. A. Jolesz, *Intraoperative imaging and image-guided therapy*, 1st ed. Springer-Verlag New York, 2014, ISBN: 978-1-4614-7656-6.

[36] A. Fenster and J. C. Lacefield, *Ultrasound imaging and therapy*, ser. Imaging in Medical Diagnosis and Therapy. CRC Press, 2015, ISBN: 9781498759977. [Online]. Available: `https://books.google.de/books?id=ipkoCwAAQBAJ`.

[37] S. Ipsen, R. Bruder, I. Kuhlemann, P. Jauer, L. Motisi, F. Cremers *et al.*, 'A visual probe positioning tool for 4D ultrasound-guided radiotherapy', in *2018 40th Annual International Conference of the IEEE Engineering in Medicine and Biology Society (EMBC)*, 2018, pp. 883–886. DOI: `10.1109/EMBC.2018.8512390`.

[38] C. Rüger, M. A. Feufel, S. Moosburner, C. Özbek, J. Pratschke and I. M. Sauer, 'Ultrasound in augmented reality: a mixed-methods evaluation of head-mounted displays in image-guided interventions', *International Journal of Computer Assisted Radiology and Surgery*, vol. 15, no. 11, pp. 1895–1905, 2020, ISSN: 18616429. DOI: `10.1007/s11548-020-02236-6`.

[39] M. Ganau, G. K. Ligarotti and V. Apostolopoulos, 'Real-time intraoperative ultrasound in brain surgery: neuronavigation and use of contrast-enhanced image fusion', *Quantitative Imaging in Medicine and Surgery*, vol. 9, no. 3, 2019, ISSN: 2223-4306. [Online]. Available: `https://qims.amegroups.com/article/view/24593`.

[40] T. Peters, *Image-guided interventions: technology and applications*, 1st ed. Springer, 2008, ISBN: 9780387738567. [Online]. Available: `https://link.springer.com/book/10.1007/978-0-387-73858-1`.

[41] K. S. Arun, T. S. Huang and S. D. Blostein, 'Least-squares fitting of two 3-D point sets', *IEEE Transactions on Pattern Analysis and Machine Intelligence*, vol. 9, no. 5, pp. 698–700, 1987, ISSN: 01628828. DOI: `10.1109/TPAMI.1987.4767965`.

[42] P. J. Besl and N. D. McKay, 'A method for registration of 3-D shapes', *IEEE Transactions on Pattern Analysis and Machine Intelligence*, vol. 14, no. 2, pp. 239–256, 1992. DOI: `10.1109/34.121791`.

[43] **F. von Haxthausen**, R. Moreta-Martinez, A. Pose Díez de la Lastra, J. Pascau and F. Ernst, 'UltrARsound: in situ visualization of live ultrasound images using HoloLens 2', *International Journal of Computer Assisted Radiology and Surgery*, 2022, ISSN: 1861-6429. DOI: `10.1007/s11548-022-02695-z`.

[44] H. Fuchs, A. State, E. D. Pisano, W. F. Garrett, G. Hirota, M. Livingston *et al.*, 'Towards performing ultrasound-guided needle biopsies from within a head-mounted display', in *Visualization in Biomedical Computing*, K. H. Höhne and R. Kikinis, Eds., Berlin, Heidelberg: Springer Berlin Heidelberg, 1996, pp. 591–600, ISBN: 978-3-540-70739-4.

[45] N. Cattari, S. Condino, F. Cutolo, M. Ferrari and V. Ferrari, 'In situ visualization for 3D ultrasound-guided interventions with augmented reality headset', *Bioengineering*, vol. 8, no. 10, 2021, ISSN: 2306-5354. DOI: `10.3390/bioengineering8100131`.

[46] R. Garbi, 'Augmented reality visualisation for orthopaedic surgical guidance with pre- and intra-operative multimodal image data fusion', *Healthcare Technology Letters*, vol. 5, no. 5, pp. 189–193, 2018. DOI: `10.1049/htl.2018.5061`.

[47] T. Kuzhagaliyev, N. T. Clancy, M. Janatka, K. Tchaka, F. Vasconcelos, M. J. Clarkson *et al.*, 'Augmented reality needle ablation guidance tool for irreversible electroporation in the pancreas', in *Medical Imaging 2018: Image-Guided Procedures, Robotic Interventions, and Modeling*, International Society for Optics and Photonics, vol. 10576, SPIE, 2018, pp. 260–265. DOI: `10.1117/12.2293671`.

[48] J. W. Meulstee, J. Nijsink, R. Schreurs, L. M. Verhamme, T. Xi, H. H. K. Delye *et al.*, 'Toward Holographic-Guided Surgery', *Surgical Innovation*, vol. 26, no. 1, pp. 86–94, 2019. DOI: `10.1177/1553350618799552`.

[49] V. García-Vázquez, **F. von Haxthausen**, S. Jäckle, C. Schumann, I. Kuhlemann, J. Bouchagiar *et al.*, 'Navigation and visualisation with HoloLens in endovascular aortic repair', *Innovative Surgical Sciences*, 2018. DOI: `10.1515/iss-2018-2001`.

[50] I. Kuhlemann, M. Kleemann, P. Jauer, A. Schweikard and F. Ernst, 'Towards x-ray free endovascular interventions – using HoloLens for on-line holographic visualisation', *Healthcare Technology Letters*, vol. 4, pp. 184–187, 2017, ISSN: 2053-3713. DOI: `10.1049/htl.2017.0061`.

[51] F. Liebmann, S. Roner, M. von Atzigen, D. Scaramuzza, R. Sutter, J. Snedeker *et al.*, 'Pedicle screw navigation using surface digitization on the microsoft HoloLens', *International Journal of Computer Assisted Radiology and Surgery*, vol. 14, no. 7, pp. 1157–1165, 2019, ISSN: 18616429. DOI: 10.1007/s11548-019-01973-7.

[52] R. Moreta-Martinez, D. García-Mato, M. García-Sevilla, R. Pérez-Mañanes, J. Calvo-Haro and J. Pascau, 'Augmented reality in computer-assisted interventions based on patient-specific 3D printed reference', *Healthcare Technology Letters*, vol. 5, no. 5, pp. 162–166, 2018, ISSN: 20533713. DOI: 10.1049/htl.2018.5072.

[53] P. Kriechling, S. Roner, F. Liebmann, F. Casari, P. Fürnstahl and K. Wieser, 'Augmented reality for base plate component placement in reverse total shoulder arthroplasty: a feasibility study', *Archives of Orthopaedic and Trauma Surgery*, vol. 141, no. 9, pp. 1447–1453, 2021. DOI: 10.1007/s00402-020-03542-z.

[54] L. Qian, X. Zhang, A. Deguet and P. Kazanzides, 'ARAMIS: Augmented reality assistance for minimally invasive surgery using a head-mounted display', in *Medical Image Computing and Computer Assisted Intervention – MICCAI 2019*, D. Shen, T. Liu, T. M. Peters, L. H. Staib, C. Essert, S. Zhou *et al.*, Eds., Cham: Springer International Publishing, 2019, pp. 74–82. DOI: 10.1007/978-3-030-32254-0_9.

[55] M. Carbone, S. Condino, F. Cutolo, R. M. Viglialoro, O. Kaschke, U. W. Thomale *et al.*, 'Proof of concept: wearable augmented reality video see-through display for neuro-endoscopy', in *Augmented Reality, Virtual Reality, and Computer Graphics*, L. T. De Paolis and P. Bourdot, Eds., Cham: Springer International Publishing, 2018, pp. 95–104. DOI: 10.1007/978-3-319-95282-6_7.

[56] C. Kunz, P. Maurer, F. Kees, P. Henrich, C. Marzi, M. Hlaváč *et al.*, 'Infrared marker tracking with the HoloLens for neurosurgical interventions', *Current Directions in Biomedical Engineering*, vol. 6, no. 1, p. 20 200 027, 2020. DOI: https://doi.org/10.1515/cdbme-2020-0027.

[57] C. Gsaxner, J. Li, A. Pepe, D. Schmalstieg and J. Egger, 'Inside-out instrument tracking for surgical navigation in augmented reality', in *Proceedings of the 27th ACM Symposium on Virtual Reality Software and Technology*, ser. VRST '21, New York, NY, USA: Association for Computing Machinery, 2021, ISBN: 9781450390927. DOI: 10.1145/3489849.3489863.

[58] F. Mahmood, E. Mahmood, R. G. Dorfman, J. Mitchell, F. U. Mahmood, S. B. Jones *et al.*, 'Augmented reality and ultrasound education: initial experience', *Journal of Cardiothoracic and Vascular Anesthesia*, vol. 32, no. 3, pp. 1363–1367, 2018, ISSN: 15328422. DOI: 10.1053/j.jvca.2017.12.006.

[59] N. A. Farshad-Amacker, T. Bay, A. B. Rosskopf, J. M. Spirig, F. Wanivenhaus, C. W. A. Pfirrmann *et al.*, 'Ultrasound-guided interventions with augmented reality in situ visualisation: a proof-of-mechanism phantom study', *European Radiology Experimental*, vol. 4, no. 1, 2020. DOI: 10.1186/s41747-019-0129-y.

[60] T. Nguyen, W. Plishker, A. Matisoff, K. Sharma and R. Shekhar, 'HoloUS: augmented reality visualization of live ultrasound images using HoloLens for ultrasound-guided procedures', *International Journal of Computer Assisted Radiology and Surgery*, 2021. DOI: `10.1007/s11548-021-02526-7`.

[61] W. Gu, *HoloLens2-ResearchMode-Unity: unity plugin for using research mode functionality in HoloLens 2. Modified based on HoloLens2ForCV.* [Online]. Available: `https://github.com/petergu684/HoloLens2-ResearchMode-Unity` (visited on 16/01/2023).

[62] R. E. Kalman, 'A new approach to linear filtering and prediction problems', *Journal of Basic Engineering*, vol. 82, no. 1, pp. 35–45, 1960, ISSN: 0021-9223. DOI: `10.1115/1.3662552`.

[63] M. Tölgyessy, M. Dekan, L. Chovanec and P. Hubinský, 'Evaluation of the Azure Kinect and its comparison to Kinect v1 and Kinect v2', *Sensors*, vol. 21, no. 2, pp. 1–25, 2021. DOI: `10.3390/s21020413`.

[64] A. Lasso, T. Heffter, A. Rankin, C. Pinter, T. Ungi and G. Fichtinger, 'PLUS: open-source toolkit for ultrasound-guided intervention ystems', *IEEE Transactions on Biomedical Engineering*, vol. 61, no. 10, pp. 2527–2537, 2014. DOI: `10.1109/TBME.2014.2322864`.

[65] J. Tokuda, G. S. Fischer, X. Papademetris, Z. Yaniv, L. Ibanez, P. Cheng *et al.*, 'OpenIGTLink: an open network protocol for image-guided therapy environment', *International Journal of Medical Robotics and Computer Assisted Surgery*, vol. 5, no. 4, pp. 423–434, 2009. DOI: `https://doi.org/10.1002/rcs.274`.

[66] SlicerIGT-community, *User tutorial U31 - Tracked ultrasound calibration*, 2016. [Online]. Available: `https://www.slicerigt.org/wp/user-tutorial/` (visited on 16/01/2023).

[67] M. Welch, J. Andrea, T. Ungi and G. Fichtinger, 'Freehand ultrasound calibration: phantom versus tracked pointer', in *Medical Imaging 2013: Image-Guided Procedures, Robotic Interventions, and Modeling*, D. R. H. III and Z. R. Yaniv, Eds., International Society for Optics and Photonics, vol. 8671, SPIE, 2013, pp. 348–353. DOI: `10.1117/12.2007922`.

[68] *Plus toolkit - printable 3D models catalog.* [Online]. Available: `http://perk-software.cs.queensu.ca/plus/doc/nightly/modelcatalog/` (visited on 16/01/2023).

[69] D. Q. Huynh, 'Metrics for 3D rotations: comparison and analysis', *Journal of Mathematical Imaging and Vision*, vol. 35, no. 2, pp. 155–164, 2009, ISSN: 1573-7683. DOI: `10.1007/s10851-009-0161-2`.

[70] C. S. Bamji, S. Mehta, B. Thompson, T. Elkhatib, S. Wurster, O. Akkaya *et al.*, ‘IMpixel 65nm BSI 320MHz demodulated TOF image sensor with 3\$$\mu$\$m global shutter pixels and analog binning’, in *2018 IEEE International Solid - State Circuits Conference - (ISSCC)*, 2018, pp. 94–96. DOI: `10.1109/ISSCC.2018.8310200`.

[71] P. Hübner, K. Clintworth, Q. Liu, M. Weinmann and S. Wursthorn, ‘Evaluation of HoloLens tracking and depth sensing for indoor mapping applications’, *Sensors*, vol. 20, no. 4, p. 1021, 2020. DOI: `10.3390/s20041021`.

[72] A. E. Lugo, N. Bockelmann and **F. von Haxthausen**, ‘Sequential U-Net architecture for automatic femoral artery segmentation in ultrasound images’, *Current Directions in Biomedical Engineering*, vol. 7, no. 1, pp. 158–161, 2021. DOI: `doi:10.1515/cdbme-2021-1034`.

[73] A. Fedorov, R. Beichel, J. Kalpathy-Cramer, J. Finet, J. C. Fillion-Robin, S. Pujol *et al.*, ‘3D Slicer as an image computing platform for the quantitative imaging network’, *Magnetic Resonance Imaging*, vol. 30, no. 9, pp. 1323–1341, Nov. 2012. DOI: `10.1016/J.MRI.2012.05.001`.

[74] O. Ronneberger, P. Fischer and T. Brox, ‘U-Net: Convolutional networks for biomedical image segmentation’, in *Medical Image Computing and Computer-Assisted Intervention – MICCAI 2015*, N. Navab, J. Hornegger, W. M. Wells and A. F. Frangi, Eds., Cham: Springer International Publishing, 2015, pp. 234–241, ISBN: 978-3-319-24574-4.

[75] D. van Erp, T. Heskes and T. van den Heuvel, ‘Automatic abdominal aortic aneurysm detection from ultrasound imaging using deep learning’, 2021. [Online]. Available: `https://www.pcultrasound.com/resources/research/publications/article_70.pdf` (visited on 16/01/2023).

[76] E. Smistad and L. Løvstakken, ‘Vessel detection in ultrasound images using deep convolutional neural networks’, in *Deep Learning and Data Labeling for Medical Applications*, G. Carneiro, D. Mateus, L. Peter, A. Bradley, J. M. R. S. Tavares, V. Belagiannis *et al.*, Eds., Cham: Springer International Publishing, 2016, pp. 30–38. DOI: `10.1007/978-3-319-46976-8_4`.

[77] E. Smistad, K. F. Johansen, D. H. Iversen and I. Reinertsen, ‘Highlighting nerves and blood vessels for ultrasound-guided axillary nerve block procedures using neural networks’, *Journal of Medical Imaging*, vol. 5, no. 4, p. 044 004, 2018. DOI: `10.1117/1.JMI.5.4.044004`.

[78] L. A. Groves, B. VanBerlo, N. Veinberg, A. Alboog, T. M. Peters and E. C. S. Chen, ‘Automatic segmentation of the carotid artery and internal jugular vein from 2D ultrasound images for 3D vascular reconstruction’, *International Journal of Computer Assisted Radiology and Surgery*, vol. 15, no. 11, pp. 1835–1846, 2020. DOI: `10.1007/s11548-020-02248-2`.

[79] **F. von Haxthausen**, C. Rüger, M. M. Sieren, R. Kloeckner and F. Ernst, 'Augmenting image-guided procedures through in situ visualization of 3D ultrasound via a head-mounted display', *Sensors*, vol. 23, no. 4, 2023. DOI: 10.3390/s23042168.

[80] L. Groves, N. Li, T. M. Peters and E. C. S. Chen, 'Towards a first-person perspective mixed reality guidance system for needle interventions', *Journal of Imaging*, vol. 8, no. 1, 2022. DOI: 10.3390/jimaging8010007.

[81] N. Cattari, S. Condino, F. Cutolo, M. Ghilli, M. Ferrari and V. Ferrari, 'Wearable AR and 3D ultrasound: towards a novel way to guide surgical dissections', *IEEE Access*, vol. 9, pp. 156 746–156 757, 2021. DOI: 10.1109/ACCESS.2021.3129324.

[82] *Holographic Remoting Overview - Mixed Reality | Microsoft Docs*. [Online]. Available: https://docs.microsoft.com/en-us/windows/mixed-reality/develop/native/holographic-remoting-overview (visited on 16/01/2023).

[83] *QR code tracking overview - Mixed Reality | Microsoft Learn*. [Online]. Available: https://learn.microsoft.com/en-us/windows/mixed-reality/develop/advanced-concepts/qr-code-tracking-overview (visited on 16/01/2023).

[84] Q. Zhang, R. Eagleson and T. M. Peters, 'Volume visualization: a technical overview with a focus on medical applications', *J. Digit. Imaging*, vol. 24, no. 4, pp. 640–664, 2011, ISSN: 1618-727X. DOI: 10.1007/s10278-010-9321-6.

[85] D. Honigmann, J. Ruisz and C. Haider, 'Adaptive design of a global opacity transfer function for direct volume rendering of ultrasound data', in *14th IEEE Visualization 2003 (VIS'03)*, ser. VIS '03, USA: IEEE Computer Society, 2003, p. 64, ISBN: 0769520308.

[86] **F. von Haxthausen**, S. Ipsen, H. Schwegmann, R. Bruder, F. Ernst and V. Garc\'\ia-Vázquez, 'A 3D Slicer module for calibration of spatially tracked 3D ultrasound probes', in *International Journal of Computer Assisted Radiology and Surgery*, vol. 15, 2020, S14–S16. DOI: https://doi.org/10.1007/s11548-020-02171-6.

[87] R. Amini, J. Z. Kartchner, L. A. Stolz, D. Biffar, A. J. Hamilton and S. Adhikari, 'A novel and inexpensive ballistic gel phantom for ultrasound training', *World Journal of Emergency Medicine*, vol. 6, no. 3, p. 225, 2015. DOI: 10.5847/wjem.j.1920-8642.2015.03.012.

[88] N. Alves, A. Kim, J. Tan, G. Hwang, T. Javed, B. Neagu *et al.*, 'Cardiac tissue-mimicking ballistic gel phantom for ultrasound imaging in clinical and research applications', *Ultrasound in Medicine and Biology*, vol. 46, no. 8, pp. 2057–2069, 2020, ISSN: 1879291X. DOI: 10.1016/j.ultrasmedbio.2020.03.011.

[89] D. S. Morrow, J. A. Cupp and J. S. Broder, 'Versatile, reusable, and inexpensive ultrasound phantom procedural trainers', *Journal of Ultrasound in Medicine*, vol. 35, no. 4, pp. 831–841, 2016. DOI: 10.7863/ultra.15.04085.

[90] E. Maneas, W. Xia, D. I. Nikitichev, B. Daher, M. Manimaran, R. Y. J. Wong *et al.*, ‘Anatomically realistic ultrasound phantoms using gel wax with 3D printed moulds’, *Physics in Medicine and Biology*, vol. 63, no. 1, 2018. DOI: `10.1088/1361-6560/aa9e2c`.

[91] U. Kuckartz, ‘Qualitative text analysis: A systematic approach’, in *Compendium for Early Career Researchers in Mathematics Education*, G. Kaiser and N. Presmeg, Eds., Cham: Springer International Publishing, 2019, pp. 181–197, ISBN: 978-3-030-15636-7. DOI: `10.1007/978-3-030-15636-7_8`.

[92] R. Rampin and V. Rampin, ‘Taguette: open-source qualitative data analysis’, *Journal of Open Source Software*, vol. 6, no. 68, p. 3522, 2021. DOI: `10.21105/joss.03522`.

[93] S. G. Hart and L. E. Staveland, ‘Development of NASA-TLX (task load index): results of empirical and theoretical research’, *Advances in Psychology*, vol. 52, no. C, pp. 139–183, Jan. 1988, ISSN: 0166-4115. DOI: `10.1016/S0166-4115(08)62386-9`.

[94] *Holographic Remoting Player - Mixed Reality | Microsoft Learn*. [Online]. Available: `https://learn.microsoft.com/en-us/windows/mixed-reality/develop/native/holographic-remoting-player#diagnostics` (visited on 16/01/2023).

[95] M. Arif, A. Moelker and T. van Walsum, ‘Automatic needle detection and real-time bi-planar needle visualization during 3D ultrasound scanning of the liver’, *Medical Image Analysis*, vol. 53, pp. 104–110, Apr. 2019, ISSN: 1361-8415. DOI: `10.1016/J.MEDIA.2019.02.002`.

[96] K. Raaen and T.-M. Grønli, ‘Latency thresholds for usability in games: a survey’, in *Norsk Informatikkonferanse*, 2014.

[97] **F. von Haxthausen**, S. Jäckle, J. Strehlow, F. Ernst and V. García-Vázquez, ‘Catheter pose-dependent virtual angioscopy images visualized on augmented reality glasses’, Current Directions in Biomedical Engineering, vol. 5, no. 1, pp. 289–291, 2019. DOI: `doi:10.1515/cdbme-2019-0073`.

[98] **F. von Haxthausen**, S. Jäckle, J. Bouchagiar, F. Matysiak, M. Kaschwich, J. P. Goltz *et al.*, ‘An augmented reality guidance system for endovascular aortic repair: first steps in reducing radiation exposure’, in *Proceedings of the 33rd International Congress and Exhibition on Computer Assisted Radiology and Surgery (CARS’19)*, 2019.

[99] C. Shi, C. Tercero, S. Ikeda, K. Ooe, T. Fukuda, K. Komori *et al.*, ‘In vitro three-dimensional aortic vasculature modeling based on sensor fusion between intravascular ultrasound and magnetic tracker’, *The International Journal of Medical Robotics and Computer Assisted Surgery*, vol. 8, no. 3, pp. 291–299, 2012. DOI: `https://doi.org/10.1002/rcs.1416`.

[100] C. Shi, S. Giannarou, S. L. Lee and G. Z. Yang, ‘Simultaneous catheter and environment modeling for Trans-catheter aortic valve implantation’, *2014 IEEE/RSJ International Conference on Intelligent Robots and Systems*, no. Iros, pp. 2024–2029, 2014, ISSN: 21530866. DOI: `10.1109/IROS.2014.6942832`.

[101] L. Zhao, S. Giannarou, S. Lee and G. Yang, ‘SCEM+: Real-time robust simultaneous catheter and environment modeling for endovascular navigation’, *IEEE Robotics and Automation Letters*, vol. 1, no. 2, pp. 961–968, 2016, ISSN: 2377-3766. DOI: `10.1109/LRA.2016.2524984`.

[102] C. Shi, C. Tercero, X. Wu, S. Ikeda, K. Komori, K. Yamamoto *et al.*, ‘Real-time in vitro intravascular reconstruction and navigation for endovascular aortic stent grafting’, *The International Journal of Medical Robotics and Computer Assisted Surgery*, vol. 12, no. 4, pp. 648–657, 2016. DOI: `10.1002/rcs.1736`.

[103] M. M. Sieren, S. Jäckle, T. Eixmann, H. Schulz-Hildebrandt, F. Matysiak, M. Preuss *et al.*, ‘Radiation-free thoracic endovascular aneurysm repair with fiberoptic and electromagnetic guidance: A phantom study’, *Journal of Vascular and Interventional Radiology*, vol. 33, no. 4, pp. 384–391, Apr. 2022, ISSN: 1051-0443. DOI: `10.1016/J.JVIR.2021.12.025`.

[104] F. Manstad-Hulaas, G. A. Tangen, L. G. Gruionu, P. Aadahl and T. A. N. Hernes, ‘Three-dimensional endovascular navigation with electromagnetic tracking: Ex vivo and in vivo accuracy’, *Journal of Endovascular Therapy*, vol. 18, no. 2, pp. 230–240, 2011. DOI: `10.1583/10-3301.1`.

[105] A. De Lambert, S. Esneault, A. Lucas, P. Haigron, P. Cinquin and J. L. Magne, ‘Electromagnetic tracking for registration and navigation in endovascular aneurysm repair: A phantom study’, *European Journal of Vascular and Endovascular Surgery*, vol. 43, no. 6, pp. 684–689, 2012, ISSN: 10785884. DOI: `10.1016/j.ejvs.2012.03.007`.

[106] S. Condino, V. Ferrari, C. Freschi, A. Alberti, R. Berchiolli, F. Mosca *et al.*, ‘Electromagnetic navigation platform for endovascular surgery: how to develop sensorized catheters and guidewires’, *The International Journal of Medical Robotics and Computer Assisted Surgery*, vol. 8, no. 3, pp. 300–310, 2012. DOI: `10.1002/rcs.1417`.

[107] M. A. A. Basha, A. F. Salem, T. M. Azmy and S. M. Shehata, ‘The added value of CT virtual angioscopy to MDCT angiography in the evaluation of aortic diseases’, *Abdominal Radiology*, vol. 45, no. 8, pp. 2576–2584, 2020, ISSN: 2366-0058. DOI: `10.1007/s00261-020-02607-2`.

[108] A. C. Tomás, Á. L. Santos and J. Fragata, ‘Virtual angioscopy and 3D navigation of the aorta’, *Journal of Cardiac Surgery*, vol. 32, no. 1, pp. 33–37, 2017. DOI: `https://doi.org/10.1111/jocs.12874`.

[109] *3D Guidance ® Tracking Technology for Your Most Realistic Training or Simulation System.* [Online]. Available: `https://www.ndigital.com/wp-content/uploads/2020/09/10005584-3D-Guidance-Simulation.pdf` (visited on 16/01/2023).

[110] *Open Inventor™ | Open Inventor Toolkit.* [Online]. Available: `https://www.openinventor.com/` (visited on 16/01/2023).

[111] E. M. Faure, L. Canaud, P. Cathala, I. Serres, C. Marty-Ané and P. Alric, 'Assessment of abdominal branch vessel patency after bare-metal stenting of the thoracoabdominal aorta in a human ex vivo model of acute type B aortic dissection', *Journal of Vascular Surgery*, vol. 61, no. 5, pp. 1299–1305, 2015, ISSN: 10976809. DOI: `10.1016/j.jvs.2013.11.095`.

[112] L. E. Savastano, Q. Zhou, A. Smith, K. Vega, C. Murga-Zamalloa, D. Gordon *et al.*, 'Multimodal laser-based angioscopy for structural, chemical and biological imaging of atherosclerosis', *Nature Biomedical Engineering*, vol. 1, no. 2, pp. 1–15, 2017, ISSN: 2157846X. DOI: `10.1038/s41551-016-0023`.

[113] *gRPC.* [Online]. Available: `https://grpc.io/` (visited on 16/01/2023).

[114] J. B. Hummel, M. R. Bax, M. L. Figl, Y. Kang, C. Maurer Jr., W. W. Birkfellner *et al.*, 'Design and application of an assessment protocol for electromagnetic tracking systems', *Medical Physics*, vol. 32, no. 7Part1, pp. 2371–2379, 2005. DOI: `https://doi.org/10.1118/1.1944327`.

[115] M. Kaschwich, M. Sieren, F. Matysiak, J. Bouchagiar, A. Dell, A. Bayer *et al.*, 'Feasibility of an endovascular training and research environment with exchangeable patient specific 3D printed vascular anatomy: Simulator with exchangeable patient-specific 3D-printed vascular anatomy for endovascular training and research', *Annals of Anatomy - Anatomischer Anzeiger*, vol. 231, p. 151 519, 2020, ISSN: 0940-9602. DOI: `https://doi.org/10.1016/j.aanat.2020.151519`.

[116] J. M. Fitzpatrick, 'Fiducial registration error and target registration error are uncorrelated', *Proc. SPIE 7261*, vol. 7261, p. 726 102, 2009, ISSN: 16057422. DOI: `10.1117/12.813601`.

[117] V. García-Vázquez, F. Matysiak, S. Jäckle, T. Eixmann, M. M. Sieren, **F. von Haxthausen** *et al.*, 'Catheter pose-dependent virtual angioscopy images for endovascular aortic repair: validation with a video graphics array (VGA) camera', *Current Directions in Biomedical Engineering*, vol. 6, no. 1, p. 20 200 010, 2020. DOI: `doi:10.1515/cdbme-2020-0010`.

[118] M. S. Balani and J. Tümler, 'Usability and user experience of interactions on VR-PC, HoloLens 2, VR cardboard and AR smartphone in a biomedical application', J. Y. C. Chen and G. Fragomeni, Eds., Cham: Springer International Publishing, 2021, pp. 275–287. DOI: `10.1007/978-3-030-77599-5_20`.

[119] S. Moosburner, C. Remde, P. Tang, M. Queisner, N. Haep, J. Pratschke *et al.*, 'Real world usability analysis of two augmented reality headsets in visceral surgery', *Artificial Organs*, vol. 43, no. 7, pp. 694–698, 2019. DOI: `https://doi.org/10.1111/aor.13396`.

[120] Y. Xiang, T. Schmidt, V. Narayanan and D. Fox, 'PoseCNN: A Convolutional Neural Network for 6D Object Pose Estimation in Cluttered Scenes', in *Robotics: Science and Systems (RSS)*, 2018. DOI: `10.48550/arXiv.1711.00199`.

[121] *Augmented and Virtual Reality in healthcare market size, report 2030.* [Online]. Available: `https://www.precedenceresearch.com/augmented-and-virtual-reality-in-healthcare-market` (visited on 16/01/2023).

[122] S. Jäckle, A. Lange, V. García-Vázquez, T. Eixmann, F. Matysiak, M. M. Sieren *et al.*, 'Instrument localisation for endovascular aneurysm repair: Comparison of two methods based on tracking systems or using imaging', *The International Journal of Medical Robotics and Computer Assisted Surgery*, vol. 17, no. 6, e2327, 2021. DOI: `https://doi.org/10.1002/rcs.2327`.

[123] *Fiber Optic RealShape (FORS) Technology - Research | Philips.* [Online]. Available: `https://www.philips.com/a-w/research/research-programs/fors.html` (visited on 16/01/2023).

[124] G. Panuccio, A. Schanzer, F. Rohlffs, F. Heidemann, B. Wessels, G. W. Schurink *et al.*, 'Endovascular navigation with Fiber Optic RealShape technology', *Journal of Vascular Surgery*, vol. 77, no. 1, pp. 3–8, Jan. 2023, ISSN: 0741-5214. DOI: `10.1016/j.jvs.2022.08.002`.

List of own Publications

Conference Publications

[1] **F. von Haxthausen**, S. Jäckle, J. Strehlow, F. Ernst and V. García-Vázquez, ‘Catheter pose-dependent virtual angioscopy images visualized on augmented reality glasses’, Current Directions in Biomedical Engineering, vol. 5, no. 1, pp. 289–291, 2019. DOI: `doi:10.1515/cdbme-2019-0073`.

[2] **F. von Haxthausen**, S. Jäckle, J. Bouchagiar, F. Matysiak, M. Kaschwich, J. P. Goltz *et al.*, ‘An augmented reality guidance system for endovascular aortic repair: first steps in reducing radiation exposure’, in *Proceedings of the 33rd International Congress and Exhibition on Computer Assisted Radiology and Surgery (CARS’19)*, 2019.

[3] **F. von Haxthausen**, S. Ipsen, H. Schwegmann, R. Bruder, F. Ernst and V. Garc\’\ia-Vázquez, ‘A 3D Slicer module for calibration of spatially tracked 3D ultrasound probes’, in *International Journal of Computer Assisted Radiology and Surgery*, vol. 15, 2020, S14–S16. DOI: `https://doi.org/10.1007/s11548-020-02171-6`.

[4] **F. von Haxthausen**, Y. Chen and F. Ernst, ‘Superimposing holograms on real world objects using hololens 2 and its depth camera’, *Current Directions in Biomedical Engineering*, vol. 7, no. 1, pp. 111–115, 2021. DOI: `doi:10.1515/cdbme-2021-1024`.

[5] A. E. Lugo, N. Bockelmann and **F. von Haxthausen**, ‘Sequential U-Net architecture for automatic femoral artery segmentation in ultrasound images’, *Current Directions in Biomedical Engineering*, vol. 7, no. 1, pp. 158–161, 2021. DOI: `doi:10.1515/cdbme-2021-1034`.

Journal Publications

[6] V. García-Vázquez, **F. von Haxthausen**, S. Jäckle, C. Schumann, I. Kuhlemann, J. Bouchagiar *et al.*, ‘Navigation and visualisation with HoloLens in endovascular aortic repair’, *Innovative Surgical Sciences*, 2018. DOI: `10.1515/iss-2018-2001`.

[7] **F. von Haxthausen**, S. Böttger, D. Wulff, J. Hagenah, V. García-Vázquez and S. Ipsen, ‘Medical robotics for ultrasound imaging: current systems and future trends’, *Current Robotics Reports*, vol. 2, no. 1, pp. 55–71, 2021. DOI: `10.1007/s43154-020-00037-y`.

[8] **F. von Haxthausen**, R. Moreta-Martinez, A. Pose Díez de la Lastra, J. Pascau and F. Ernst, ‘UltrARsound: in situ visualization of live ultrasound images using HoloLens 2’, *International Journal of Computer Assisted Radiology and Surgery*, 2022, ISSN: 1861-6429. DOI: `10.1007/s11548-022-02695-z`.

[9] **F. von Haxthausen**, C. Rüger, M. M. Sieren, R. Kloeckner and F. Ernst, ‘Augmenting image-guided procedures through in situ visualization of 3D ultrasound via a head-mounted display’, *Sensors*, vol. 23, no. 4, 2023. DOI: `10.3390/s23042168`.

[10] A. Pose-Díez-de-la-Lastra, R. Moreta-Martinez, M. García-Sevilla, D. García-Mato, J. A. Calvo-Haro, L. Mediavilla-Santos *et al.*, ‘Hololens 1 vs. hololens 2: Improvements in the new model for orthopedic oncological interventions’, *Sensors*, vol. 22, no. 13, 2022, ISSN: 1424-8220. DOI: `10.3390/s22134915`. [Online]. Available: `https://www.mdpi.com/1424-8220/22/13/4915`.

List of Figures

Introduction 1

List of Tables

Acronyms

AAA Abdominal Aortic Aneurysm

AB Active Brightness

AHAT Articulated HAnd Tracking

AR Augmented Reality

CNN Convolutional Neural Networks

CT Computed Tomography

CTA Computed Tomography Angiography

CVD Cardiovascular Diseases

DSA Digital Subtraction Angiography

DUS Duplex Ultrasonography

EM Electromagnetic

EVAR Endovascular Aortic Repair

FBGs Fibre Bragg Gratings

FOV Field-of-View

FRE Fiducial Registration Error

HMD Head-Mounted Display

HRM Holographic Remoting Mode

ICP Iterative Closest Point

IGT Image-Guided Therapy

IVUS Intravascular Ultrasound

LEDs Light-Emitting Diodes

LR Learning Rate

MRI Magnetic Resonance Imaging

OCT Optical Coherence Tomography

OST Optical See-Through

OTF Opacity Transfer Function

OTS Optical Tracking System

PAD Peripheral Arterial Disease

R-CNN Region Based Convolutional Neural Networks

ReLU Rectified Linear Unit

SD Standard Deviation

SLAM Simultaneous Localization and Mapping

TLX Task Load Index

tUS Tomographic Ultrasound

US Ultrasound

UWP Universal Windows Platform

VA Virtual Angioscopy

VPT Video Pass-Through

VR Virtual Reality

Felix von Haxthausen

Google Scholar

Work Experience

ongoing
Feb 2018

***Researcher* - Institute for Robotics and Cognitive Systems, University of Lübeck, Germany**

Working on navigation systems based on Augmented Reality, ultrasound imaging and robotics to navigate medical applications.

Tracking for Augmented Reality:

- Investigated an outside-in approach based on electromagnetic tracking for endovascular tools [1].
- Developed an inside-out approach to track retroreflective spheres using the depth camera integrated into HoloLens 2. Achieved a tracking error of $<2\ mm$ [2].
- Evaluated ready-to-use systems such as Vuforia regarding their accuracy [3].
- Implemented a marker-less, point cloud based registration approach which does not rely on additional hardware [4].

Streaming methods for Augmented Reality:

- Created a HoloLens application to stream and visualize virtual angioscopy images. The appropriate image format reduced the latency by 87 % [5].
- Developed a HoloLens applications to stream and visualize 2D and 3D ultrasound images [6, 2]. A loss-less data encoding allowed a decrease of 63 % in transmitted data size.

Visual servoing of robots:

- Development of a Deep Learning-based robot control system that can automatically acquire an ultrasound scan of peripheral arteries [7].
- Investigated current systems and future trends for robotic ultrasound systems [8].

Mar 2022
Sep 2021

***Visiting Researcher* - Image Guided Therapy Research Group, University Carlos III of Madrid, Spain**

- Developed a HoloLens 2 application to spatially track retroreflective spheres using the on-board camera systems and stream ultrasound images with minimal latency [2].
- Investigated the accuracy of the tracking approach during an orthopedic oncological intervention.
- Participated and won the best project award at the Medical Augmented Reality Summer School.

Oct 2017
Feb 2017

***Master Thesis Student* - neuroloop GmbH, Freiburg, Germany**

- Developed a signal processing pipeline for blood pressure correlated nerve signals.
- Implemented machine learning methods to estimate the blood pressure.
- Participated in animal experiments for acquiring the nerve signals.

Dec 2016
Sep 2016

***Research Intern* - Manipal University, Manipal, India**

- Developed a low-cost hemoglobin-meter for use in rural India.
- Participated in a workshop on Kalman filters.

Aug 2015
Feb 2015

***Intern & Bachelor Thesis Student* - Drägerwerk AG & Co. KGaA, Lübeck, Germany**

- Investigated the cross-sensitivity and temperature behavior of a gas sensor based on a miniaturized Fabry-Pérot-Interferometer.
- Evaluated different chemometrical methods for gas concentration estimation.

Education

Jul 2023
Feb 2018

***PhD* - Biomedical Engineering**
University of Lübeck, Germany
Topic: "Augmented Reality Applications to Facilitate Vascular Diagnostics and Interventions"

Nov 2017
Sep 2015

***Master of Science* - Biomedical Engineering** CGPA (German): 1.5
University of Lübeck, Germany

Jan 2015
Aug 2014

***Erasmus Exchange* - Molecular Biology**
Boğaziçi University, Istanbul, Turkey

Aug 2015
Sep 2011

***Bachelor of Science* - Biomedical Engineering** CGPA (German): 1.3
Hamburg University of Applied Sciences, Germany

AWARDS, SCHOLARSHIPS & CERTIFICATES

2023 | ***Certificate*** **- Scrum Foundation, Master & Product Owner**

2021 | ***Award*** **- Best Project Award - Medical Augmented Reality Summer School**

2021 | ***Scholarship*** **- DAAD funded international research stay for computer scientists**

2021 | ***Award*** **- Best Poster at CURAC conference**

2020 | ***Award*** **- Best Paper at CURAC conference**

2015 | ***Award*** **- Best Graduate of 2015 in Biomedical Engineering**

SKILLS

Unity: ● ● ● ● ○ | C#: ● ● ● ○ ○ | MATLAB: ● ● ● ● ○ | Python: ● ● ○ ○ ○ | C++ ● ● ○ ○ ○

LANGUAGES

German - native | English - C2 | Spanish - A2

SELECTED PUBLICATIONS

[1] V. García-Vázquez, F. von Haxthausen, S. Jäckle, C. Schumann, I. Kuhlemann, J. Bouchagiar, A.-C. Höfer, F. Matysiak, G. Hüttmann, J. P. Goltz *et al.*, "Navigation and visualisation with Hololens in endovascular aortic repair," *Innov Surg Sci*, vol. 3, no. 3, pp. 167–177, 2018. Available at: https://doi.org/10.1515/iss-2018-2001

[2] F. von Haxthausen, R. Moreta-Martinez, A. Pose-Díez-de-la Lastra, J. Pascau, and F. Ernst, "UltrARsound: in situ visualization of live ultrasound images using Hololens 2," *Int J Comput Assist Radiol Surg*, pp. 1–11, 2022. Available at: https://doi.org/10.1007/s11548-022-02695-z

[3] A. Pose-Díez-de-la Lastra, R. Moreta-Martinez, M. García-Sevilla, D. García-Mato, J. A. Calvo-Haro, L. Mediavilla-Santos, R. Pérez-Mañanes, F. von Haxthausen, and J. Pascau, "Hololens 1 vs. Hololens 2: Improvements in the new model for orthopedic oncological interventions," *Sensors*, vol. 22, no. 13, 2022. Available at: https://www.mdpi.com/1424-8220/22/13/4915

[4] F. von Haxthausen, Y. Chen, and F. Ernst, "Superimposing holograms on real world objects using Hololens 2 and its depth camera," *Curr Dir Biomed Eng*, vol. 7, pp. 111–115, 2021. Available at: https://doi.org/10.1515/cdbme-2021-1024

[5] F. von Haxthausen, S. Jäckle, J. Strehlow, F. Ernst, and V. García-Vázquez, "Catheter pose-dependent virtual angioscopy images visualized on augmented reality glasses," *Curr Dir Biomed Eng*, vol. 5, no. 1, pp. 289–291, 2019. Available at: https://doi.org/10.1515/cdbme-2019-0073

[6] F. von Haxthausen, C. Rüger, M. M. Sieren, R. Kloeckner, and F. Ernst, "Augmenting image-guided procedures through in situ visualization of 3D ultrasound via a head-mounted display," *Sensors*, vol. 23, no. 4, 2023. Available at: https://www.mdpi.com/1424-8220/23/4/2168

[7] F. von Haxthausen, J. Hagenah, M. Kaschwich, M. Kleemann, V. García-Vázquez, and F. Ernst, "Robotized ultrasound imaging of the peripheral arteries–a phantom study," *Curr Dir Biomed Eng*, vol. 6, no. 1, 2020. Available at: https://doi.org/10.1515/cdbme-2020-0033

[8] F. von Haxthausen, S. Böttger, D. Wulff, J. Hagenah, V. García-Vázquez, and S. Ipsen, "Medical robotics for ultrasound imaging: current systems and future trends," *Curr Robot Rep*, vol. 2, no. 1, pp. 55–71, 2021. Available at: https://doi.org/10.1007/s43154-020-00037-y

INTERESTS

Swimming | Cycling | Concerts | 3D printing | Volleyball